Non-local electrical conductivity in $PdCoO_2$

by

Graham Baker

B.Sc., Queen's University, 2016

A THESIS SUBMITTED IN PARTIAL FULFILLMENT
OF THE REQUIREMENTS FOR THE DEGREE OF

Doctor of Philosophy

in

THE FACULTY OF GRADUATE AND POSTDOCTORAL STUDIES
(Physics)

The University of British Columbia
(Vancouver)

October 2022

The following individuals certify that they have read, and recommend to the Faculty of Graduate and Postdoctoral Studies for acceptance, the thesis entitled:

Non-local electrical conductivity in $PdCoO_2$

submitted by **Graham Baker** in partial fulfillment of the requirements for the degree of **Doctor of Philosophy** in **Physics**.

Examining Committee:

Douglas Bonn, Professor, Department of Physics and Astronomy, UBC
Supervisor

Scott Oser, Professor, Department of Physics and Astronomy, UBC
Supervisory Committee Member

Alireza Nojeh, Professor, Department of Electrical and Computer Engineering, UBC
University Examiner

Jörg Rottler, Professor, Department of Physics and Astronomy, UBC
University Examiner

N. Peter Armitage, Professor, Department of Physics and Astronomy, The Johns Hopkins University
External Examiner

Additional Supervisory Committee Members:

Sarah Burke, Professor, Department of Physics and Astronomy & Department of Chemistry, UBC
Supervisory Committee Member

Marcel Franz, Professor, Department of Physics and Astronomy, UBC
Supervisory Committee Member

Abstract

Electrical conduction becomes non-local when an inhomogeneous electronic distribution is induced with a spatial variation shorter than the mean free path (MFP) between momentum-relaxing electronic scattering processes. Two important methods of inducing such a distribution are via the size and skin effects. In the size effect, one or more dimensions of a medium are reduced below the MFP. The scattering of electrons from the medium's boundaries then induces an inhomogeneous electronic distribution under an applied direct current. In the skin effect, the exponential decay of alternating electromagnetic fields as they propagate into the medium gives rise to a so-called skin layer. The electronic distribution within the skin layer becomes inhomogeneous as the skin depth falls below the MFP.

Here we study the size and skin effects in $PdCoO_2$, both experimentally and theoretically. While previous theoretical treatments of non-local electrical conductivity have assumed a free-electron dispersion, we observe that the anisotropic Fermi surface (FS) in $PdCoO_2$ results in behaviour that is incompatible with this assumption.

Measurements of the size effect in $PdCoO_2$ revealed two novel phenomena, both of which are symmetry-forbidden for local conduction: anisotropy in the in-plane longitudinal resistivity, and a non-zero transverse resistivity at zero magnetic field. We developed a theory of the size effect for arbitrary FS geometry and used it to reproduce the key features of these measurements.

Motivated by recent interest in the possibility that electrons in solids may behave viscously as a result of frequent internal momentum-conserving scattering, we developed a generalized theory of the skin effect, taking into account separate rates of momentum-conserving and momentum-relaxing scattering for arbitrary FS geometry. For an isotropic FS, our theory encompasses several known limiting behaviours. For anisotropic FSs, we explored geometries which lead to changes in the scaling of the surface impedance.

By applying bolometric broadband microwave spectroscopy, we studied the skin effect in $PdCoO_2$ for three different directions of electromagnetic propagation. Using symmetry-based arguments, we determined that our measurements were neither in the local nor purely viscous regime. We argued instead that the data demonstrate a novel, predominantly ballistic effect as a result of the faceted FS.

Lay Summary

Two familiar formulas of physics, Newton's second law and Ohm's law, are seemingly at odds with one another. In Newton's second law, a constant force produces a constant acceleration. But in Ohm's law, the force of a constant electric field on the electrons in a metal leads to a constant current, proportional to the electrons' velocity. The reason this holds in most metals is that the electrons undergo frequent collisions that randomize their velocity. But in the absence of these collisions, electrical conductivity becomes non-local: an electron's velocity at a given point in space depends not only on the electric field at the same point, but over its entire trajectory. Unlike familiar fluids in which particles are equally likely to travel in any direction, the electrons in $PdCoO_2$ are almost exclusively confined to travel in only six directions. Here we study how this leads to several novel non-local effects.

Preface

The work presented in this thesis was conducted during my time as a graduate student at the University of British Columbia, under the supervision of Doug Bonn.

A version of chapter 2 has been published [5]:

> Maja D. Bachmann*, Aaron L. Sharpe*, Graham Baker, Arthur W. Barnard, Carsten Putzke, Thomas Scaffidi, Nabhanila Nandi, Philippa H. McGuinness, Elina Zhakina, Michal Moravec, Seunghyun Khim, Markus König, David Goldhaber-Gordon, D.A. Bonn, Andrew P. Mackenzie, and Philip J.W. Moll,
> **Directional ballistic transport in the two-dimensional metal $PdCoO_2$**
> *Nature Physics* (2022)

where * denotes equal contribution. The experimental results, including device fabrication and electrical measurements, were mainly the work of M.D.B. while completing a doctorate under the supervision of A.P.M. and P.J.W.M. at the Max Planck Institute for Chemical Physics of Solids. The samples of $PdCoO_2$ came from A.P.M.'s group. The theoretical work, including the theory of the size effect for arbitrary Fermi surface geometry and the specific application to $PdCoO_2$, is my own.

A version of chapter 3 has been submitted for publication [69]:

> Davide Valentinis, Graham Baker, D.A. Bonn, and Jörg Schmalian,
> **Kinetic theory of the non-local electrodynamic response in anisotropic metals: skin effect in 2D systems**
> *arXiv:2204.13344* (2022)

This work is theoretical and computational in nature and is closely related to the experimental work presented in chapter 4. The idea for this work arose from conversations between me, D.A.B., and J.S. about the interpretation of the experiments described in chapter 4. The subsequent research was performed collaboratively by me, J.S. and D.V.. The original results for chapter 3 are presented in sections 3.3.1, 3.3.3 and 3.3.4. *Section 3.3.1*: This derivation is my own. It is a generalization and modification of an earlier derivation by J.S.. The original derivation of a collision integral which gives rise to a quasi-conserved quantity, by J.S., was based on quasi-conserved crystal momentum and assumed two-dimensional systems with isotropic local conductivity tensor. I performed the calculation presented in section 3.3.1, which generalizes the original calculation to two- and three-dimensional systems with anisotropic local conductivity tensor, and applies it to quasi-conserved linear momentum rather than crystal momentum. *Section 3.3.3*: The series expansions of the conductivity in this section are my own but closely follow

work done by D.V.. *Section 3.3.4*: The discussion and analytical results for the asymptotic behaviour of the surface impedance in this section are my own work. Figures 3.3 to 3.5 and the numerical results therein are the work of D.V. but are the result of numerous discussions between us.

A version of chapter 4 has been submitted for publication [6]:

> Graham Baker, Timothy W. Branch, James Day, Davide Valentinis, Mohamed Oudah, Philippa H. McGuinness, Seunghyun Khim, Piotr Surowka, Roderich Moessner, Jörg Schmalian, Andrew P. Mackenzie, and D.A. Bonn,
> **Non-local microwave electrodynamics in ultra-pure $PdCoO_2$**
> *arXiv:2204.14239* (2022)

I was the lead investigator for this work. D.A.B. and I designed the research program. I was responsible for data collection and analysis. I performed the calculations, with input from J.S. and D. V.. D.A.B. and I wrote the manuscript. T.W.B. performed the finite-element method electromagnetic simulations. The samples of $PdCoO_2$ came from A.P.M.'s group. All authors contributed to the interpretation of the data.

Table of Contents

List of Tables

List of Figures

List of Symbols

$\mathscr{C}$	collision integral
$\hat{C}$	linearized collision operator
$\mathscr{E}$	energy
E	electric field
H	magnetic field
J	electrical current density
k	crystal momentum
l	mean free path (chapter 3)
q	wavevector
$\mathscr{S}_F$	Fermi surface
S_F	Fermi surface area
W	sample width
δ	skin depth
λ	mean free path (everywhere except chapter 3)
γ	scattering rate
ρ	electrical resistivity
σ	electrical conductivity
τ	scattering time
ω	angular frequency

List of Abbreviations

AC alternating current

ARPES angle-resolved photoemission spectroscopy

ASE Anomalous Skin Effect

BMS bolometric microwave spectroscopy

CSE Classical Skin Effect

CMS Corbino microwave spectroscopy

DC direct current

FS Fermi surface

FIB focused ion beam

MC momentum-conserving

MCP microwave cavity perturbation

MFP mean free path

MR momentum-relaxing

NLE non-local electrodynamics

QO quantum oscillations

RTA relaxation time approximation

SIBC surface impedance boundary condition

TE transverse electric

TEF transverse electron focusing

TEM transverse electromagnetic

TM transverse magnetic

VSE Viscous Skin Effect

Acknowledgments

Thank you to my supervisor, Doug Bonn. I am grateful for the opportunities he has provided me, including to work with the unique technique of bolometric microwave spectroscopy, and to work on interesting research projects with excellent collaborators. I have benefitted from his broad knowledge of condensed matter physics, commitment to Socratic teaching, and level-headed guidance. I have appreciated his enthusiasm, humour, and knack for telling a good story.

Thank you to James Day for his support throughout my time at UBC. I appreciate his commitment to mentorship, his friendship, and his sense of humour. I admire his thoughtful and deliberate approach across all areas of life, which I aspire to emulate.

Thank you to my collaborators. From the Max Planck Institute of Chemical Physics of Solids: Andy Mackenzie, Seunghyun Khim, Maja Bachmann, Philippa McGuinness; from the Karlsruhe Institute of Technology: Jörg Schmalian, Davide Valentinis; from the Max Planck Institute for the Physics of Complex Systems: Roderich Moessner, Piotr Surowka. Each of them has made important contributions to this work, and our discussions have been a pleasure.

Thank you to my lab-mates. To Aaron Kraft for the camaraderie. To Brandon Stuart for his friendship throughout classes, conferences, and preparing for the comprehensive exam. To Mohamed Oudah for his sense of humour and willingness to answer so many questions on chemistry and crystal growth. To Tim Branch for his shared interest and enthusiasm about our research. To all of the LAIR group for providing such a great community.

Thank you to the friends outside of the lab who have made my time in Vancouver so enjoyable and helped ease the stress of graduate school.

Thank you to my family. To my dad for exposing me to physics originally and for being my coach and rock. To my mom for her encouragement and reminders to seek balance. To my sister for leading by example with grit, determination, and perseverance.

Thank you to my partner's family for having me stay with them during the beginning of the pandemic, for providing such a wonderful community away from home in British Columbia, and for their encouragement.

Thank you to my partner, Siobhan. She has accompanied me through the ups and downs of my PhD with patience and faith. I am so grateful for her continual support and encouragement.

Chapter 1

Introduction

1.1 Overview

When describing electrical transport in solids, the assumption of a local relationship between electrical current $\boldsymbol{J}$ and electrical field $\boldsymbol{E}$—that the current at position $\boldsymbol{r}$ depends only on the electric field at that same point $\boldsymbol{r}$—is ubiquitous, leading to the familiar version of Ohm's law

$$J_i(\boldsymbol{r}) = \sigma_{ij} E_j(\boldsymbol{r}) \tag{1.1}$$

where $\boldsymbol{\sigma}$ is the electrical conductivity tensor. In fact, this is a special case of a more general relation. In general, the dynamics of electrons can depend on the entire history of the electric field they have experienced, and therefore electrical current at a given position can depend on the electrical field elsewhere:

$$J_i(\boldsymbol{r}) = \int d\boldsymbol{r}' \, \sigma_{ij}(\boldsymbol{r}, \boldsymbol{r}') E_j(\boldsymbol{r}'). \tag{1.2}$$

The reason that eq. (1.1) can be used so widely in place of eq. (1.2) is that typically electrons are scattered, in a manner which resets their dynamics, on a length scale much shorter than the spatial variation in the electric current or electric field.

Historically, non-local electrical conduction has been studied in two distinct settings. In direct current (DC) electrical measurements in micro-structured samples, scattering of electrons at the boundaries of the sample leads to spatially non-uniform current—a phenomenon known as the size effect. In alternating current (AC) electromagnetic measurements in bulk samples, spatially non-uniform current arises because electromagnetic fields decay as they propagate into the sample—a phenomenon known as the skin effect. In both cases, non-local effects arise when the current is sufficiently non-uniform.

Recently, two things have served to generate significant interest in non-local electrical conduction, as described in the following two sections.

Scattering beyond the relaxation time approximation

When an electric field is applied to a metal, it modifies the distribution of electrons away from the distribution at equilibrium. The scattering of electrons acts to return the distribution to its equilibrium form.

Historically, the understanding of both the size effect and the skin effect has been rooted in the relaxation time approximation (RTA), which assumes that there is a single rate at which collisions cause the entire non-equilibrium distribution to decay. (We will describe the RTA mathematically in chapter 2.) This gives rise to the notion of a single electron mean free path (MFP) between collisions. In this case, the spatial nature of electron dynamics can fall into one of two regimes, depending on how the measurement length scale w compares to the MFP λ. (In the size effect, w is a physical sample dimension; in the skin effect, w is the skin depth—the decay length of the electromagnetic fields). When $\lambda \ll w$, electrical conduction is local. When $\lambda \gg w$, electrical conduction is non-local and *ballistic*: electrons travel unimpeded on the scale of w.

From an ab initio viewpoint, the dynamics by which the various possible electron scattering mechanisms act to relax the non-equilibrium electronic distribution are far more complex than assumed in the RTA. While the local conductivity is only sensitive to the rate at which non-equilibrium momentum decays, the non-local conductivity is sensitive to the entire spectrum of decay rates associated with the various scattering mechanisms at play. Of particular recent interest has been the prospect of a regime in which momentum-conserving (MC) scattering is more frequent than momentum-relaxing (MR) scattering, in which electrons would behave collectively as a viscous fluid[1]. The regimes that arise when scattering is characterized by distinct MC and MR MFPs are illustrated in fig. 1.1.

New ultra-pure materials with anisotropic Fermi surfaces

Materials with sufficiently high purity to allow for the potential observation of non-local electrical conduction are scarce. The materials for which non-local conduction has previously been studied have posessed Fermi surfaces (FSs) that consist of either (1) a single, nearly-isotropic sheet, or (2) multiple sheets with complex geometries.

Early studies of non-local conduction were performed on certain elemental metals for which a high level of refinement is possible. Among the elements, only the monovalent metals posess simple FSs. These consist of the alkali metals Na, K, Rb, and Cs, and the noble metals Cu, Ag, and Au. The alkali metals posess almost exactly spherical FSs, while the FSs of the noble metals are nearly spherical except for "necks" at which they make contact with the boundaries of the Brillouin zone. For all other elemental metals, the FS is relatively complex [3].

Over the last several decades, non-local electrical conduction has been studied most intensely in GaAs and graphene, both of which posess FSs which consist of a single, two-dimensional sheet which is approximately isotropic.

Ultra-high purity has recently become available in the delafossite metals $PdCoO_2$, $PtCoO_2$, $PdRhO_2$,

[1]The distinction between MC and MR scattering is with respect to the total momentum of all electrons rather than the momentum of an individual electron.

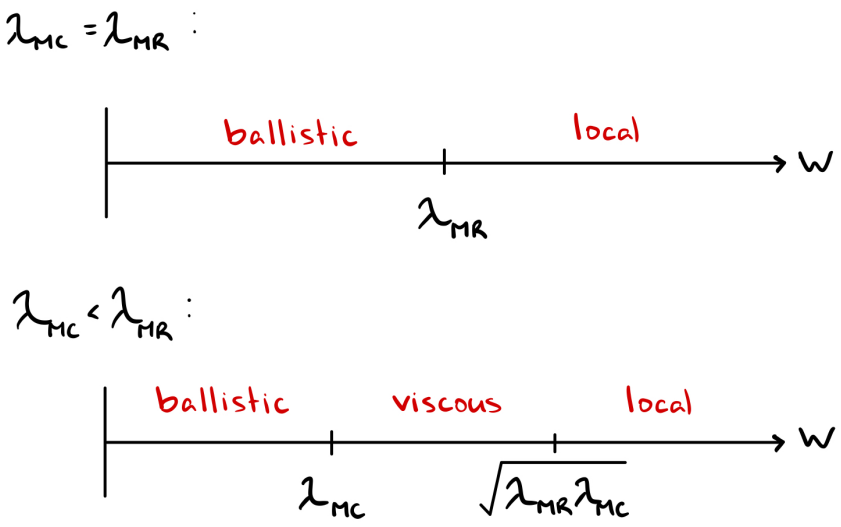

Figure 1.1: Illustration of non-local conduction regimes as a function of measurement length scale w. Top: When the MR and MC MFPs are equal, conduction is local at long length scales and ballistic at short length scales. Bottom: When the MC MFP is much shorter than the MR MFP, a viscous regime exists at intermediate length scales.

and $PdCrO_2$. These metals share the feature of having a quasi-two-dimensional FS with a nearly-hexagonal cross section. Therefore, their FSs are both simple yet anisotropic. This combination has the potential to lead to novel non-local effects distinct from those observed in any previous materials.

The work described in this thesis is both theoretical and experimental in nature, with $PdCoO_2$—the delafossite metal with the longest low-temperature MFP—as the focus of the experimental efforts. The central aim is to be able to theoretically treat the size and skin effects in a metal of arbitrary Fermi surface and with arbitrary ratio of MC and MR scattering, and to experimentally measure how these various factors are manifested in the properties of $PdCoO_2$. The remainder of this chapter is focussed on setting the context for the work described in subsequent chapters. The two branches of inquiry—the size effect and the skin effect—have developed largely independently of one another. Therefore, both require that different gaps be filled in. It is therefore instructive to consider the histories of these two branches separately, up to their status immediately prior to the present work. In section 1.2, we review the history of non-local electrical transport studies. In section 1.3, we review both the basic experimental facts about $PdCoO_2$ and several non-local transport studies to date. In section 1.4, we review the historical development of the theory of non-local electrodynamics. Finally, in section 1.5, we summarize the status of each of these areas and outline the problem that each of the subsequent chapters will address.

1.2 History of non-local transport

1.2.1 Local transport

Ohm's law, in the context of electromagnetism, is conventionally written as

$$J_i = \sigma_{ij} E_j \tag{1.3}$$

where $\boldsymbol{J}$ is current density [A/m^2], $\boldsymbol{E}$ is electric field [$\mathrm{V\,m}^{-1}$] and $\boldsymbol{\sigma}$ is the conductivity matrix [$\Omega\,\mathrm{m}$]. This equation can be inverted to obtain

$$E_i = \rho_{ij} J_j \tag{1.4}$$

where

$$\rho_{ij} \equiv \sigma_{ij}^{-1} \tag{1.5}$$

is the resistivity tensor.

In the context of electrical circuits, Ohm's law is conventionally stated as

$$V = RI \tag{1.6}$$

where V is voltage [V], I is current [A], and R is resistance [Ω]. Consider a conductor of arbitrary but uniform cross section with cross-sectional area A and length l. If the potential V is uniform across each end, then $\boldsymbol{E}$ is uniform throughout the conductor. Using

$$V = -\int d\boldsymbol{l} \cdot \boldsymbol{E} \tag{1.7}$$

we have

$$E = \frac{V}{l}. \tag{1.8}$$

If we take eq. (1.3) to be true, then $\boldsymbol{J}$ is also uniform throughout the conductor. Using

$$I = \int d\boldsymbol{a} \cdot \boldsymbol{J} \tag{1.9}$$

we have

$$J = \frac{I}{A}. \tag{1.10}$$

Substituting eqs. (1.8) and (1.10) into eq. (1.4) we get eq. (1.6) with

$$R = \frac{l\rho}{A}. \tag{1.11}$$

Conventionally, ρ is viewed as an intrinsic property of a material, with R containing extrinsic geometrical factors.

1.2.2 Ballistic transport

Ballistic size effect

In the 1930s, Lovell [37] and Appleyard and Lovell [2] observed width-dependent resistivity in high-purity films of the alkali metals K, Rb, and Cs deposited in high vacuum. They observed a resistivity which approached that of bulk samples for sufficiently thick films, suggesting that the origin of the increasing resistivity with decreasing film thickness was a result of the electron MFP being limited by film thickness. While there had been previous reports of width-dependent resistivity, the films in those reports had not been deposited in high vacuum. Their resistivities were always much greater than the bulk value, regardless of thickness, suggesting that they were instead dominated by defects introduced in the deposition process.

Soon after the work of Lovell and Appleyard, Fuchs [24] developed what is now the standard theory of the "size effect". This theory is now commonly known as Fuchs-Sondheimer theory as a result of Sondheimer's well-known review [56]. Fuchs-Sondheimer theory is a kinetic theory based on the Boltzmann equation, a mathematical treatment of which we will defer to chapter 2. Fuchs-Sondheimer theory uses the RTA and is based on the assumption of a three-dimensional metal with electronic dispersion relation

$$\mathscr{E}_{\boldsymbol{k}} = \frac{\hbar^2 k^2}{2m}. \tag{1.12}$$

It describes how the ratio of resistivity ρ to bulk resistivity ρ_0 varies with the ratio of the finite dimension W to the MFP λ, defined as κ:

$$\kappa \equiv \frac{W}{\lambda} \tag{1.13}$$

The main result is that

$$\frac{\rho}{\rho_0} = \frac{\Phi(\kappa)}{\kappa} \tag{1.14}$$

with

$$\frac{1}{\Phi(\kappa)} = \frac{1}{\kappa} - \frac{3}{2\kappa^2}\int_1^\infty dt \left(\frac{1}{t^3} - \frac{1}{t^5}\right)\left(1 - e^{-\kappa t}\right). \tag{1.15}$$

Later, Beenakker and van Houten [8, 9] developed a theory of the size effect for a two-dimensional metal, with all other assumptions the same as for Fuchs-Sondheimer theory. They found that

$$\frac{\rho}{\rho_0} = \left[1 - \frac{4}{\pi\kappa}\int_0^1 d\xi\,\xi\sqrt{1-\xi^2}(1 - e^{-\kappa/\xi})\right]^{-1} \tag{1.16}$$

In both 2D and 3D, the asymptotic behaviour is given by

$$\frac{\rho}{\rho_0} = \begin{cases} 1 + \dfrac{\alpha}{\kappa} & \kappa \gg 1 \\ \dfrac{\beta}{\kappa \log(1/\kappa)} & \kappa \ll 1 \end{cases} \tag{1.17}$$

with the coefficients α and β listed in table 1.1.

	3D	2D
α	$\frac{3}{8}$	$\frac{3}{4\pi}$
β	$\frac{4}{3}$	$\frac{\pi}{2}$

Table 1.1: Coefficients for the asymptotic behaviour of the ballistic size effect. Cf. eq. (1.17).

The key result is that there are two distinct regimes. When the sample width W is much larger than the MFP λ, the resistivity ρ tends to a width-independent, intrinsic value ρ_0. This is known as the *local* regime. When the MFP λ is much larger than the sample width ρ, the resistivity ρ is dominated by the scattering of electrons at sample boundaries and has a strong width dependence given by $[\kappa \log(1/\kappa)]^{-1}$. This is known as the *ballistic* regime, because electrons propagate in straight paths across the finite dimension of the sample.

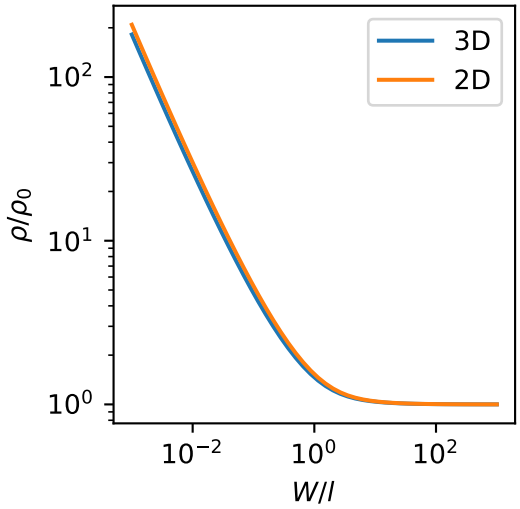

Figure 1.2: Theory of the ballistic size effect for two- and three-dimensional free electron metals. The ratio of resistivity to bulk resistivity as a function of the ratio of channel width to bulk MFP, as per eqs. (1.14) to (1.16).

Other manifestations of ballistic transport

Ballistic transport generally refers to any case in which the MFP exceeds a physical sample dimension. The size effect for a single finite dimension, as discussed above, represents the simplest such geometry. The size effect has also been studied for two finite dimensions, in channels with rectangular and circular cross-sections. Throughout the early history of ballistic transport, the systems under study were high-purity elemental metals. In the 1980s, high-purity semiconductor heterostructures and novel microstructuring techniques emerged. GaAs-based heterostructures became a central system in the study of ballistic transport, and novel microstructuring techniques allowed for more complex geometries to

become available. Two important experimental geometries were transverse electron focusing (TEF) and square junctions. These will be described in section 1.3.3.

It is also worth briefly clarifying what is beyond the scope of the current discussion of ballistic transport. In microstructured conductors, another length scale can become important: the Fermi wavelength λ_F, defined as $\lambda_F = 2\pi/k_F$ where k_F is the Fermi momentum. When sample dimensions are comparable to λ_F, quantum interference effects can become important. In this case, a fully quantum-mechanical treatment based in the Landauer-Büttiker formalism becomes necessary, rather than the semiclassical Boltzmann approach [8]. We will not be concerned with such effects here. In high-conductivity materials, the MFP is much greater than λ_F. Furthermore, λ_F in metals is much smaller than in semiconductors such as GaAs. In $PdCoO_2$, the low-temperature MFP is 20 µm while $\lambda_F = 0.66$ nm [28].

1.2.3 Viscous transport

Viscous size effect

In the 1960s, Gurzhi [26] proposed that viscous effects may be observable in the flow of electrons in solids. Indeed, a viscous regime exists in both classical and quantum fluids. The difference in a solid-state system is that the electrons flow amidst the background of an ionic lattice, providing a pathway for the electronic momentum to be relaxed. Gurzhi's proposal was that while local electrical conduction is set by MR scattering, MC collisions give rise to viscosity and, if MC scattering were frequent enough, this could be observable in non-local electrical conduction. While earlier work in this field assumed that MR scattering would arise from impurities while MC scattering would arise from normal electron-electron scattering, recently there has been growing awareness that the microscopic attribution of MC and MR scattering can be more complex. For example, even a single scattering mechanism can relax the momentum of a non-equilibrium distribution of electrons faster than other modes of that distribution [35, 36].

The simplest model for how viscosity would manifest in electrical transport in a channel of finite width W is based in a hydrodynamical description. Note that such a description is already based in the assumption that MC scattering is more frequent than both scattering at the sample's boundaries and MR scattering. Within a hydrodynamical description, a charged fluid flowing in a channel bounded along the y direction has a flow velocity $u(y)$ described by

$$\nu \frac{d^2u}{dy^2} + e\frac{E_x}{m} = \gamma_{mr} u. \tag{1.18}$$

where ν is the fluid's viscosity and γ_{mr} is the rate of MR scattering [26]. Defining

$$\kappa \equiv \frac{W}{l_G} \tag{1.19}$$

where here the relevant length scale is the Gurzhi length

$$l_G \equiv \sqrt{\frac{\nu}{\gamma_{mr}}}, \tag{1.20}$$

one arrives at

$$\frac{\rho}{\rho_0} = \left(1 - \frac{2}{\kappa}\tanh\frac{\kappa}{2}\right)^{-1}. \tag{1.21}$$

Equation (1.21) assumes so-called no-slip boundary conditions, meaning that at the boundaries, the fluid has no velocity relative to the boundaries. Equation (1.21) has the asymptotic behaviour

$$\frac{\rho}{\rho_0} = \begin{cases} 1 & \kappa \gg 1 \\ \\ \dfrac{12}{\kappa^2} & \kappa \ll 1. \end{cases} \tag{1.22}$$

Here again, we see that two distinct regimes emerge. When sample width W is much greater than the Gurzhi length l_G, we recover the local regime. In the opposite limit, the resistivity is dominated by the viscosity and varies as $\nu/\gamma_{mr}W^2$. This is known as the *viscous* regime.

Size effect in GaAs

In the 1990s, Molenkamp and de Jong [42] and De Jong and Molenkamp [20] were the first to observe viscous electron flow in a solid by studying narrow wires of GaAs. Their work was also significant because of the model they developed, which is now widely adopted. This model accounted for both MR and MC MFPs, and was thus able to provide a unified description for the local, viscous, and ballistic regimes. As will become important to the work described in this thesis, however, their theory made the assumption of a two-dimensional metal with free-particle-like dispersion, leading to an isotropic FS.

Other manifestations of viscous transport

Viscous transport has been searched for most widely in GaAs and graphene [38]. While the presence of $\rho \sim W^{-2}$ behaviour in a sample with a single finite dimension is particularly conceptually simple, other more complex experiments have been studied as well.

One class of experiments that has recently emerged is to study the same geometry as the size effect—a sample with one finite dimension—but to use a local imaging technique to measure the profile of the electric current and field across the finite sample dimension via scanning probe techniques. The electric field can be measured locally via a scanning single-electron transistor [58]; the electric current can be measured via scanning nitrogen-vacancy magnetometry [33, 70].

Another class of experiments has looked at more complex geometries, like flow past a slit, in which vortex behaviour can form [7, 45].

1.3 $PdCoO_2$

The delafossite metal $PdCoO_2$, whose crystal structure is shown in fig. 1.3, is uniquely positioned as a result of two factors:

1. The delafossite metals are unique among ultra-high-conductivity metals in exhibiting simple yet anisotropic and facetted Fermi surfaces, and

2. $PdCoO_2$ exhibits the longest low-temperature MFP among the delafossites.

In sections 1.3.1 and 1.3.2 I will present the key experimental results which establish these two properties of $PdCoO_2$ and briefly discuss their potential causes. In section 1.3.3, I will present several mesoscopic transport studies whose results are a consequence of one or both of these two properties.

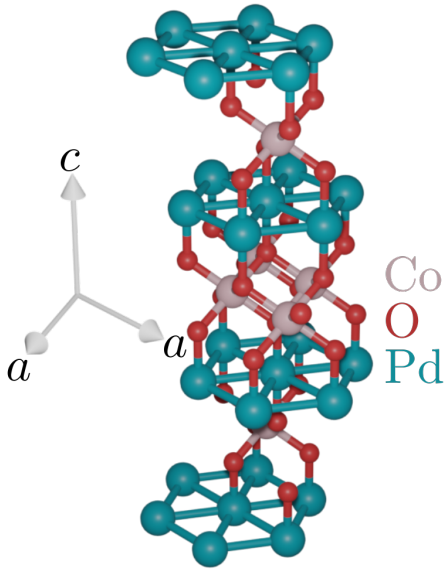

Figure 1.3: Crystal structure of $PdCoO_2$.

1.3.1 Fermi surface

The quantum oscillations (QO) measurements by Hicks et al. [28] provide key information about the three-dimensional Fermi surface of $PdCoO_2$. The FS deduced from the QO measurements of Hicks et al. [28], in combination with information from earlier angle-resolved photoemission spectroscopy (ARPES) [46], is shown in fig. 1.4. It is seen that only a single band crosses the Fermi level. This band is nearly cylindrical and has a nearly-hexagonal cross section. Later ARPES measurements by Sunko [60] provide a high-resolution picture of the nearly-hexagonal cross section.

A nearly hexagonal Fermi surface which fills half the Brillouin zone is common to $PdCoO_2$, $PdRhO_2$, $PtCoO_2$, and $PdCrO_2$ [39]. It is instructive to consider how it arises in a tight-binding model. For a tri-

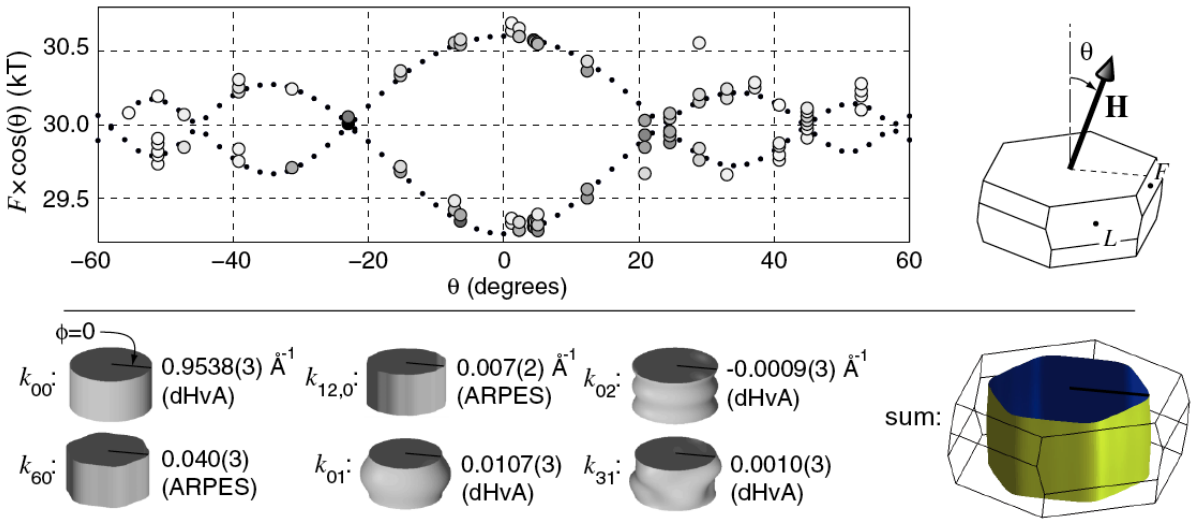

Figure 1.4: Quantum oscillations measurements of $PdCoO_2$. Top: Fit to oscillation frequencies as a function of angle. Bottom: Harmonic components included in the fit and their amplitudes. From [28].

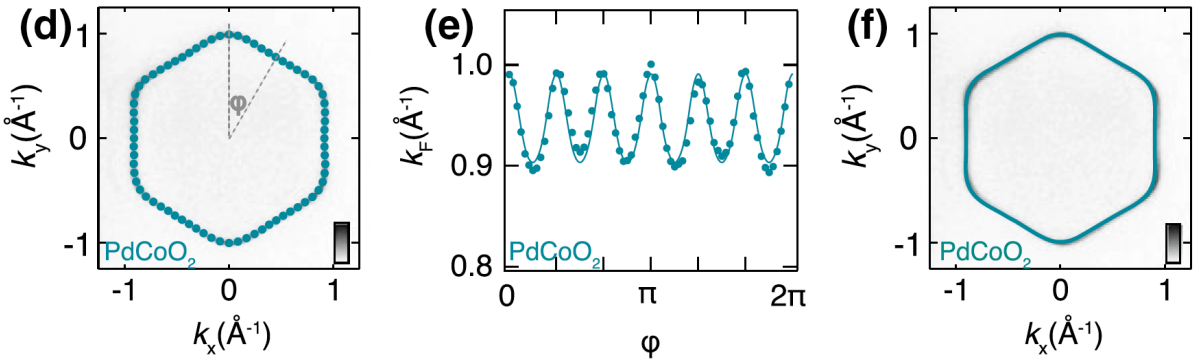

Figure 1.5: Angle-resolved photoemission spectroscopy measurements of $PdCoO_2$. (d) Photoemission intensity in grayscale. Dots are Fermi momenta obtained by fitting radial momentum distribution curves. (e) Fermi momenta as a function of angle with harmonic fit (line). (f) Harmonic fit superimposed on photoemission intensity. From [60].

angular lattice with only nearest-neighbour hopping, a hexagonal FS appears, but at 3/4 filling rather than at 1/2 filling. If hopping is included beyond nearest neighbours, a hexagonal FS arises at 1/2 filling.

1.3.2 Bulk transport

Hicks et al. [28] also performed high-resolution resistivity measurements of $PdCoO_2$, as shown in section 1.3.2.

The in-plane resistivity ρ_{ab} is consistent with the sum of a temperature-independent and an Arrhenius term. The temperature independent residual resistivity is typically associated with electron-impurity scattering. When combined with the plasma frequency ω_p and Fermi velocity v_F taken from QO measurements, the residual resistivity corresponds to a MFP of $\approx 20\,\mu$m. The observation of an

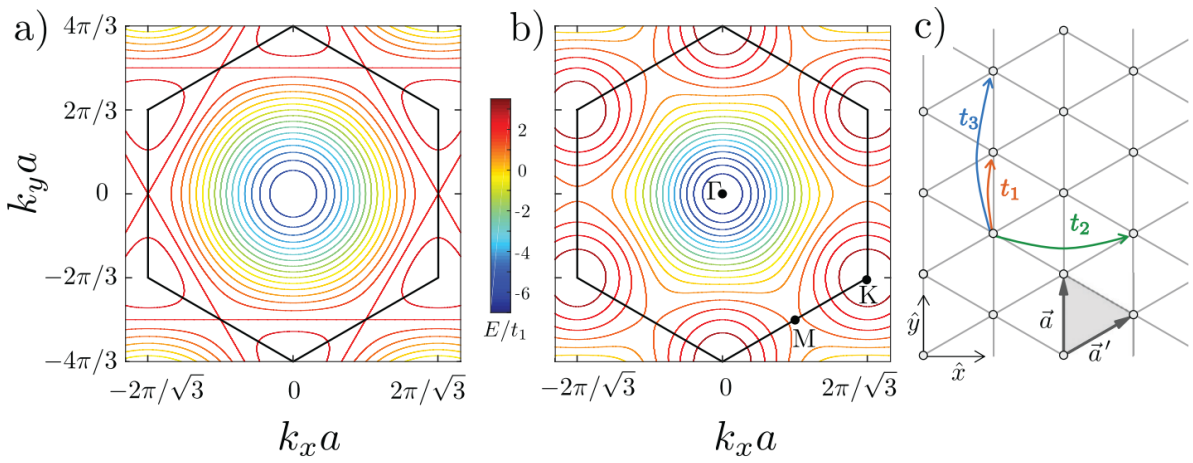

Figure 1.6: Tight-binding model on a triangular lattice. (a) Contours for a model with only nearest-neighbour hopping (indicated by t_1 in (c)). A hexagonal contour appears at 3/4 filling of the Brillouin zone. (b) Contours for a model with t_1 and t_3 hopping terms (as shown in (c) with $t_3 = 0.15t_1$. A nearly-hexagonal contour appears at 1/2 filling, similar to the FS of $PdCoO_2$ determined by ARPES. A similar result can also be obtained for a model including hopping term t_2 rather than t_3. From [39].

Arrhenius term is associated with phonon drag, which is electron-phonon scattering in which the decay of the non-equilibrium phonon distribution is slow.

The out-of-plane residual resistivity is roughly 1000× greater than the in-plane residual resistivity. This large resistivity anisotropy has frequently been used to treat electrical transport in $PdCoO_2$ in a two dimensional approximation. Given that the shape of the Fermi surface (as determined from QO) only leads to an anisotropy of ≈ 250, this implies that scattering itself is anisotropic.

The exceptionally long low-temperature in-plane MFP raises the question of its cause. Comparable MFPs have only been achieved after decades of effort. While the focus of this thesis is more so on the consequences of this, we will comment briefly here on possible causes. There have been two studies to look into possible causes [61, 65]. The residual scattering rate may be low because of crystalline perfection or because scattering is suppressed for some reason. For example, for dilute impurities, the collision probability is given by

$$W_{\boldsymbol{k},\boldsymbol{k}'} = \frac{2\pi}{\hbar}\delta(\mathscr{E}_{\boldsymbol{k}} - \mathscr{E}_{\boldsymbol{k}'})\, n_{\text{imp}}\, U^2_{\boldsymbol{k},\boldsymbol{k}'} \tag{1.23}$$

where n_{imp} is the number of impurities per unit volume and the matrix element $U_{\boldsymbol{k},\boldsymbol{k}'}$ is given by

$$U_{\boldsymbol{k},\boldsymbol{k}'} = \left|\langle \boldsymbol{k}|U|\boldsymbol{k}'\rangle\right| = \int d\boldsymbol{r}\, \psi^*_{\boldsymbol{k}'}(\boldsymbol{r}) U(\boldsymbol{r}) \psi_{\boldsymbol{k}}(\boldsymbol{r}) \tag{1.24}$$

where $\psi_{\boldsymbol{k}}$ are the single-electron states and $U(\boldsymbol{r})$ is the impurity potential. The question then is whether $W_{\boldsymbol{k},\boldsymbol{k}'}$ is low because n_{imp} is low (crystalline perfection) or because $U_{\boldsymbol{k},\boldsymbol{k}'}$ is low (suppression of scattering).

Usui et al. [65] argued that $U_{\boldsymbol{k},\boldsymbol{k}'}$ is suppressed. While their focus was on $PtCoO_2$, the same ideas

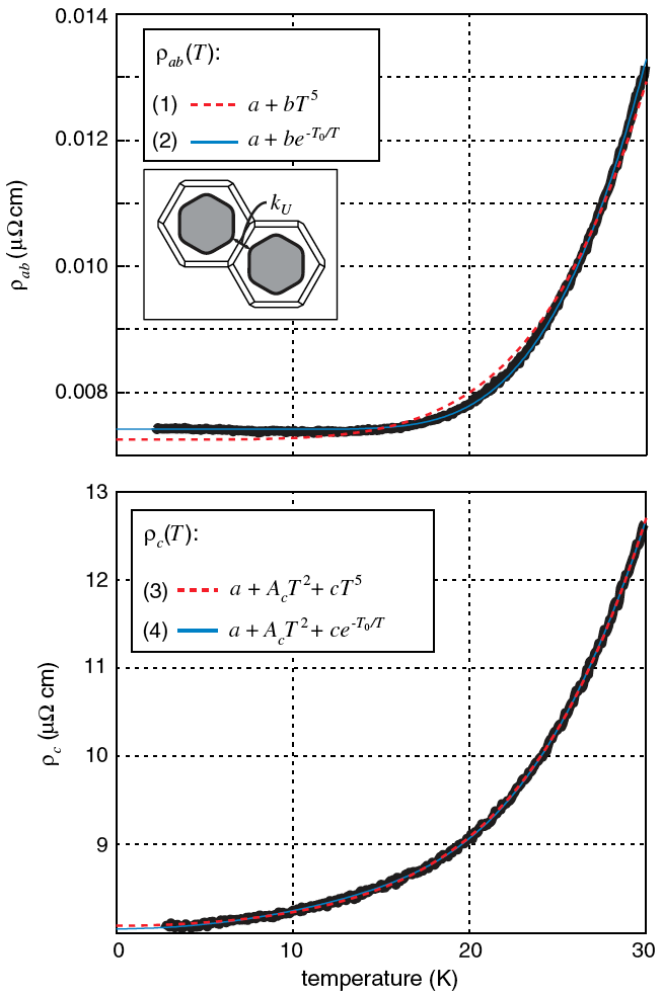

Figure 1.7: Bulk resistivity of $PdCoO_2$. Top: In-plane resistivity. Using the plasma frequency and Fermi velocity values deduced from QO measurements, the residual resistivity value corresponds to a MFP of 20 µm. The temperature dependent part of the resistivity is better fit to an Arrhenius rather than a T^5 dependence, indicating electron-phonon drag. Bottom: c-axis resistivity. The residual resistivity is $> 1000\times$ greater than the in-plane residual resistivity. From [28].

apply to $PdCoO_2$. They considered two tight-binding models for the Pt triangular-lattice planes: (1) a single-orbital model that reproduces the experimentally-observed FS geometry, and (2) a microscopically realistic multi-orbital model. They found that the multi-orbital model leads to a suppression of scattering, as shown in fig. 1.8.

Sunko et al. [61] sought to investigate the role of n_{imp}. The authors introduced defects via electron irradiation and looked at the relationship between the increase in resistivity and introduced defect concentration, as shown in fig. 1.9. From this relationship, they found that the introduced defects were acting as strong scatterers. They used this fact to argue that suppression of scattering must not be significant, and that the low resistivity in as-grown crystals must arise from a low impurity concentration. Of course, an implicit assumption of this logic is that the behaviour of the defects in as-grown samples

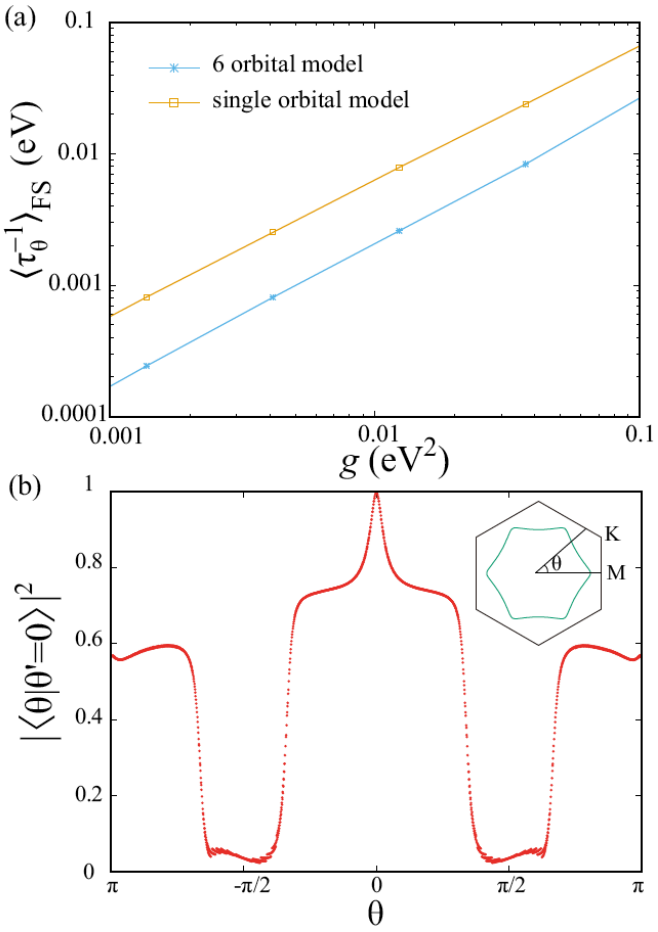

Figure 1.8: Theoretical calculation of matrix element based suppression of impurity scattering in $PtCoO_2$. (a) FS-averaged impurity scattering rate as a function of the parameter $g \propto U_0^2$, where U_0 is the strength of the impurity potential. The scattering rate in a microscopically realistic multi-orbital model is lower than that for a single-orbital model. (b) The overlap of wave functions on the Fermi surface relative to that at $\theta = 0$ as a function of angle. The overlap is strongly suppressed along certain directions for which the two wave functions have different orbital character. This suppresses the impurity scattering matrix element and therefore also reduces the averaged impurity scattering rate. From [65].

is sufficiently similar to that of defects introduced via electron irradiation.

1.3.3 Mesoscopic transport

Evidence for viscous effects

Moll et al. [43] reported evidence for viscous effects in $PdCoO_2$ in 2016. Their experiment consisted of using a focused ion beam (FIB) to create and then repeatedly narrow a channel, as shown in fig. 1.10 a. In so doing, the authors measured resistivity as a function of width. By comparing to the theory developed by Molenkamp and de Jong [42], they showed that their data was more consistent with $\gamma_{mc}/\gamma_{mr} \approx 10$

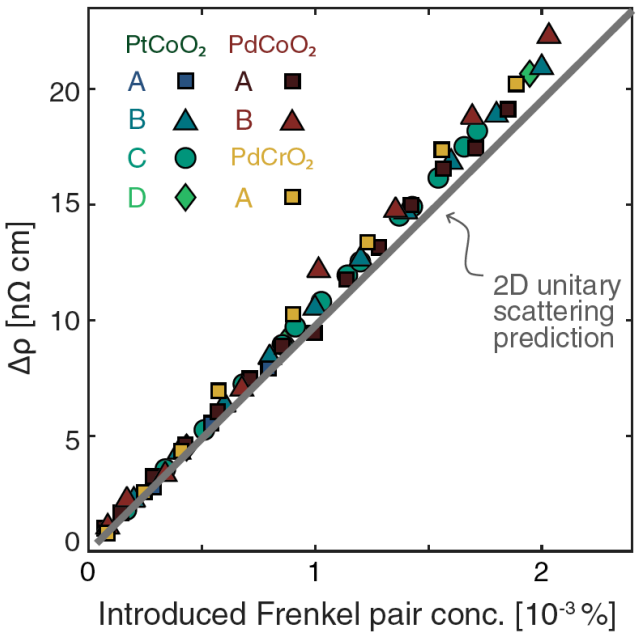

Figure 1.9: Electron irradiation induced resistivity increase in $PtCoO_2$, $PdCoO_2$, and $PdCrO_2$. Electron irradiation was used to introduce Frenkel pairs—the combination of a vacancy and an interstitial atom created when an atom is displaced. The increase in resistivity (relative to that prior to irradiation) versus concentration of introduced Frenkel pairs is similar to the unitary scattering prediction, implying that Frenkel pairs act as strong scatterers. From [61].

than a purely ballistic calculation, as shown in fig. 1.10 b & c.

Moll et al. [43] did not provide a conclusive interpretation as to the source of MC scattering observed in their experiment, but did discuss two possibilities. They commented that the rate of electron-electron scattering was uncertain because of the Fermi surface faceting. They also commented that electron-phonon scattering in the presence of phonon drag could be MC. Since then, both of these issues have been explored theoretically.

Cook and Lucas [18] studied electron-electron collisions in polygonal Fermi surfaces. They found that electron-electron scattering rates are modified relative to a circular Fermi surface. However, they noted that, given that $T \ll T_F$, electron-electron scattering was unlikely to be a significant factor in the data of Moll et al. [43]. They further noted that the unconventional width dependence of the resistivity only set in at the lowest temperatures. Based on these observations, they called into question a hydrodynamic interpretation of the data.

Levchenko and Schmalian [36] and later Huang and Lucas [29] studied electron-phonon hydrodynamics. We will defer a discussion of these results until later in this thesis.

Evidence for directional ballistic effects

The first evidence for "directional ballistic" effects came from the work of Bachmann et al. [4]. They studied TEF in $PdCoO_2$, an effect which had previously been observed in GaAs and graphene. The setup for such an experiment is shown in fig. 1.11 a. Electrons are injected through a narrow nozzle attached

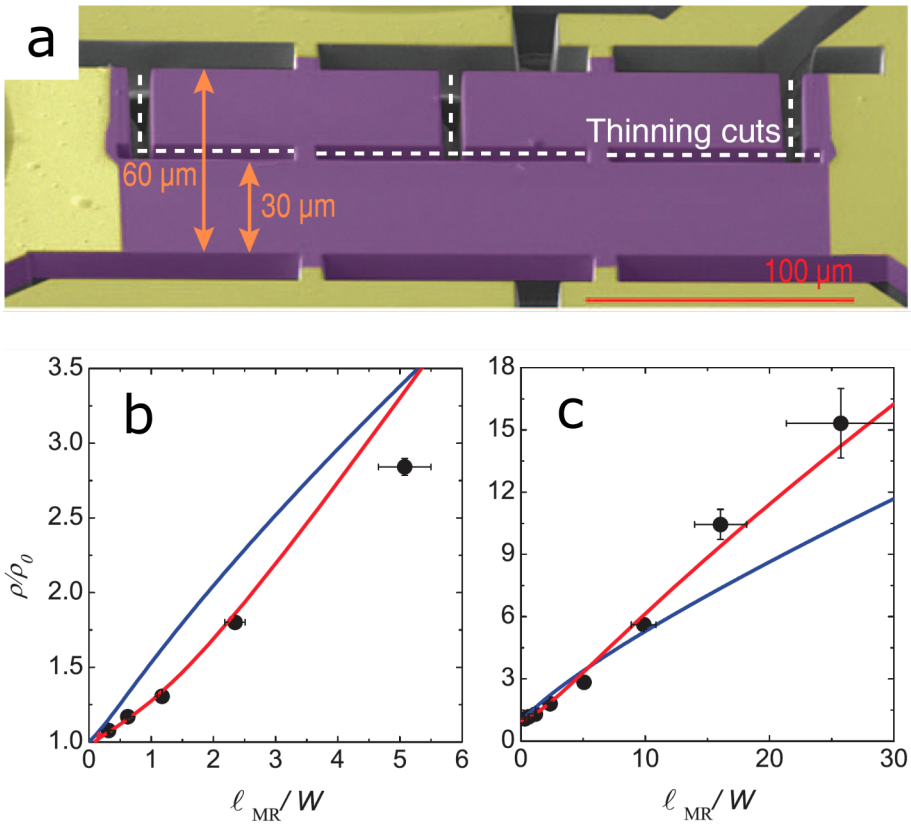

Figure 1.10: Evidence for viscous effects from mesoscopic transport in $PdCoO_2$. (a) $PdCoO_2$ channel fabricated by FIB which was successively thinned in order to measure the width-dependence of the resistivity. Shown at an intermediate stage in the process in which a 30 μm channel has been defined from a 60 μm channel. (b), (c) Ratio of resistivity ρ to bulk resistivity ρ_0 as a function of the ratio of the MR MFP l_{MR} to the channel width W. The full dataset is shown in (c), while (b) shows a more detailed view of the data at low values of l_{MR}/W. The blue line is the ballistic prediction. The red line is a calculation for MC scattering in excess of MR scattering, and provides a closer match to the data. From [43].

to a current source. An out-of-plane magnetic field induces in-plane cyclotron motion with cyclotron radius r_c. A receiver nozzle is placed a distance L from the injection nozzle and is connected to a voltmeter. When $L = n2r_c$ where n is an integer, electrons are focused onto the second nozzle leading to a voltage peak. In this study, the authors performed a TEF experiment for two different orientations of the FS relative to the nozzles. As shown in fig. 1.11 b & c, one orientation results in higher focussing peaks than the other.

Recent measurements by McGuinness et al. [41], shown in fig. 1.12, found new directional ballistic effects. They studied electrical transport in square junctions of $PdCoO_2$ and $PtCoO_2$, an experiment which had previously been done in GaAs and graphene. The authors produced two square junctions with different orientations relative to the FS and studied electrical properties as a function of square size w. At high temperature, when the MFP is smaller than w, the measurements are independent of w. At low temperature, when the MFP is greater than w, the measurements depend strongly on w. For one FS

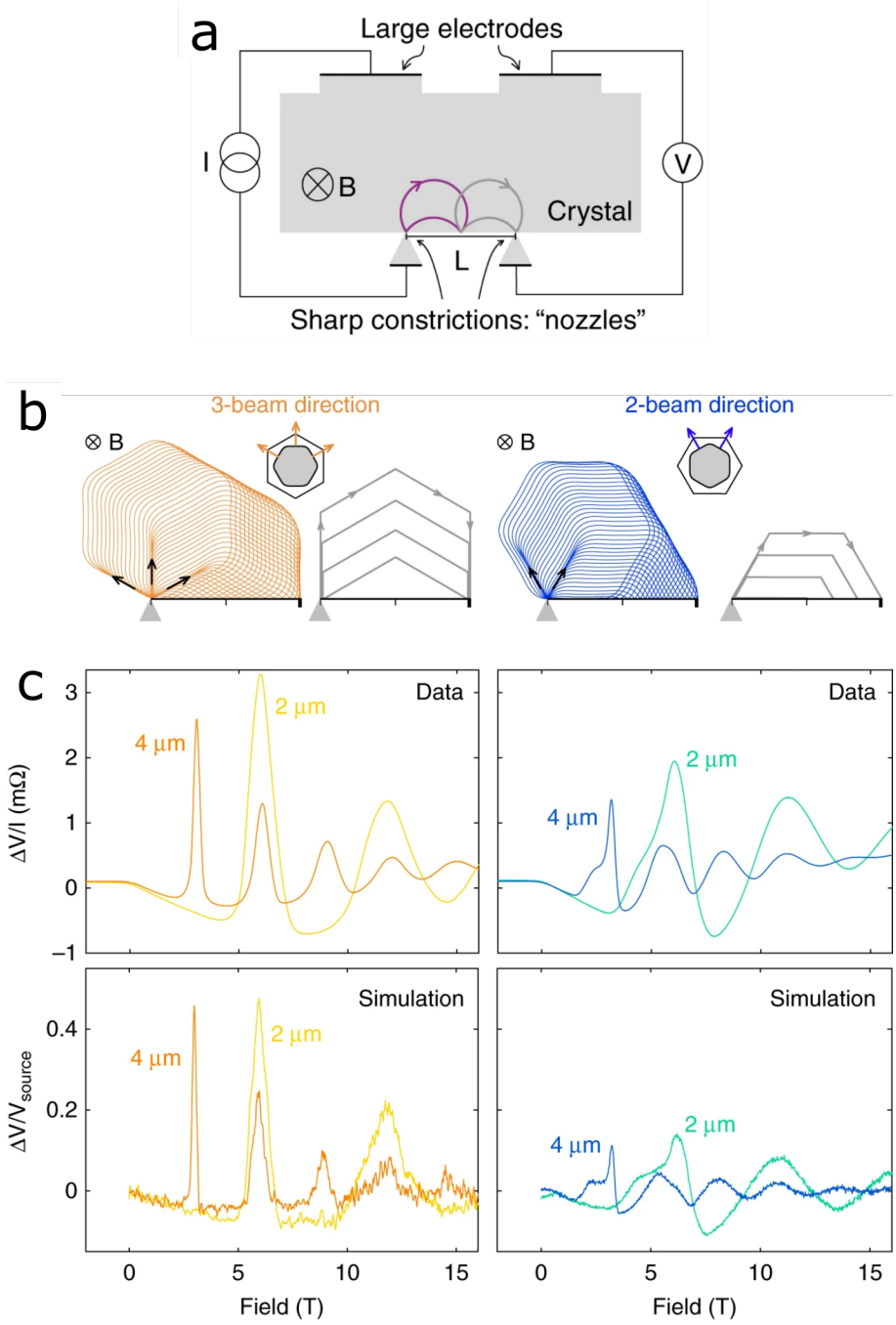

Figure 1.11: Anisotropic transverse electron focussing in $PdCoO_2$. (a) Schematic of a TEF experiment and depiction of electron trajectories for a circular FS. (b) Depiction of electron trajectories for two orientations of the Fermi surface relative to the injection nozzle. (c) Voltage as a function of magnetic field for nozzle separation lengths of 2 µm and 4 µm showing the expected peak structure. Measured peaks are larger on the left than on the right as a consequence of FS orientation (top), as confirmed by ballistic Monte Carlo simulations (bottom). From [4].

orientation, the results are independent of which "bend" is used. In the other FS orientation, the results vary strongly between the two bends.

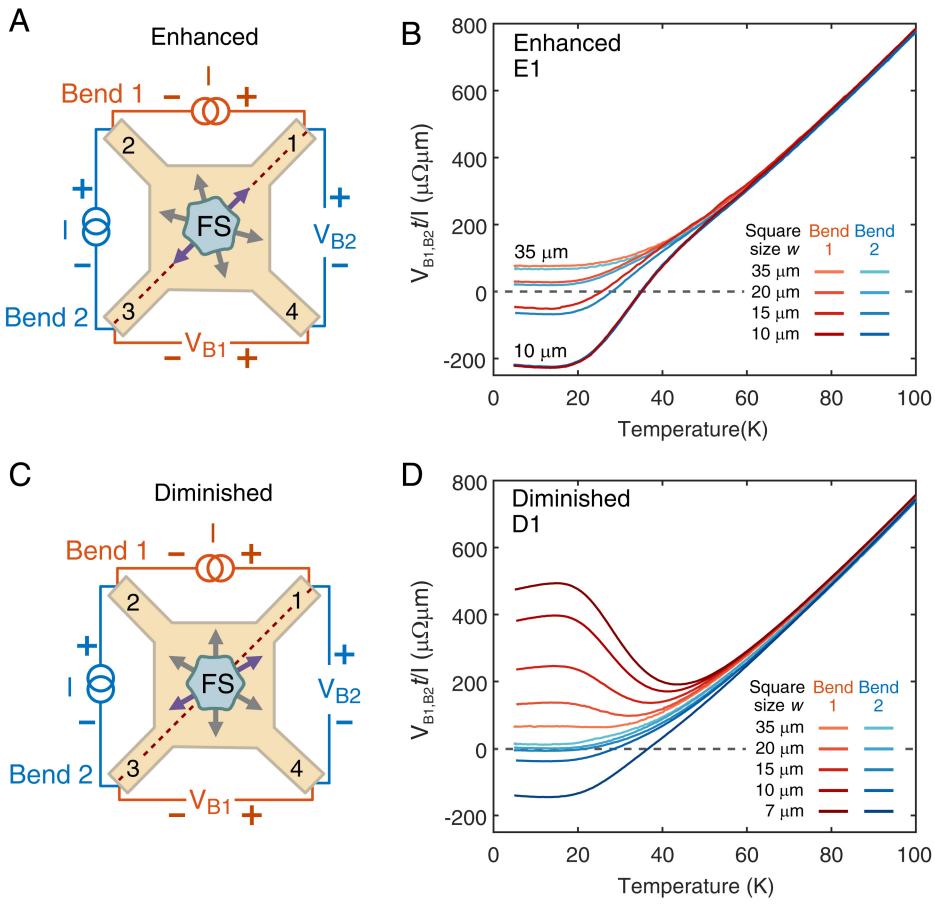

Figure 1.12: Anisotropic electrical transport in square junctions of $PtCoO_2$. Square junctions were fabricated for two different FS orientations, and in each junction the $I-V$ characteristic of two "bends" was measured. In all cases, V/I becomes width dependent at low-temperature upon entering the ballistic regime. For the high-symmetry junction (a), V/I is approximately equal for both bends (b). For the low-symmetry junction (c), V/I becomes highly anisotropic in the ballistic regime (d). From [41].

1.4 History of non-local electrodynamics

1.4.1 Classical skin effect

The Classical Skin Effect (CSE) corresponds to the standard textbook result for the propagation of an electromagnetic wave in a good conductor. Maxwell's equations lead to the following equation for the electric field:

$$\left(\nabla^2 - \frac{\partial^2}{\partial t^2}\right)\boldsymbol{E} = \mu_0 \frac{\partial}{\partial t}\boldsymbol{J}. \tag{1.25}$$

The CSE occurs if we assume the local version of Ohm's law, eq. (1.1). In this case, eq. (1.25) has the general solution

$$\boldsymbol{E} = \sum_i \boldsymbol{E}_{0i} e^{i(\boldsymbol{q}_i \cdot \boldsymbol{r} - \omega t)} \tag{1.26}$$

where the q_i are given by

$$q_\pm = \pm\sqrt{\frac{\omega^2}{c^2} + i\mu_0\omega\sigma}. \tag{1.27}$$

In a semi-infinite sample only the exponentially-decaying solution can exist and so $\boldsymbol{E}_{0-} = 0$. The simplest model of frequency-dependent conductivity is the Drude model, as given by

$$\sigma(\omega) = \varepsilon_0\omega_p^2 \frac{1}{\gamma - i\omega} \tag{1.28}$$

where ω_p is the plasma frequency and γ is the scattering rate. This has two limiting cases depending on how frequency compares to the scattering rate:

$$\frac{\sigma(\omega)}{\varepsilon_0\omega_p^2} = \begin{cases} \dfrac{1}{\gamma} & \gamma \gg \omega \text{ (Hagen-Rubens)} \\ -\dfrac{1}{i\omega} & \gamma \ll \omega \text{ (relaxation).} \end{cases} \tag{1.29}$$

In fact, the Drude model arises from the Boltzmann equation in the RTA under the assumption that the electronic distribution is spatially uniform, as will be discussed in section 2.2.6.

Finally, there is a third regime in the electromagnetic behaviour, the transmission regime, which is not manifested in the conductivity. The transmission regime occurs when the q_i are predominantly real, meaning that the electromagnetic fields decay negligibly as they propagate into the sample. From eqs. (1.27) and (1.28), the condition for the transmission regime in the context of the Drude model is

$$\omega > \begin{cases} \omega_p & \gamma \ll \omega \\ \dfrac{\omega_p^2}{\gamma} & \gamma \gg \omega. \end{cases} \tag{1.30}$$

1.4.2 Anomalous skin effect

Discovery

In the 1940s, Pippard [47] made temperature-dependent measurements of the DC conductivity σ and AC microwave-frequency surface conductance Σ of the metals Ag, Au, Sn, and Hg. Pippard's results are shown in fig. 1.13. Pippard found that for low σ (high temperature), $\Sigma \sim \sqrt{\sigma}$, as expected from the CSE. At high σ (low temperature), Pippard observed that Σ became independent of σ. Pippard proposed that this anomalous behaviour, now known as the Anomalous Skin Effect (ASE), was a result of the MFP becoming longer than the skin depth δ.

Pippard proposed a phenomenological picture for this phenomenon, which is known as Pippard's ineffectiveness concept. The logic is as follows: Only those electrons which undergo a collision within the skin layer are effective in the conduction process. The smaller the angle at which an electron is propagating relative to the sample's surface, the more likely it is to undergo a collision within the skin layer. If we consider only a fraction $\beta\delta/\lambda$ of electrons to be effective where β is a dimensionless coefficient, then we may define an effective conductivity

$$\sigma^{\text{eff}} = \beta\frac{\delta}{\lambda}\sigma \tag{1.31}$$

The classical skin depth is given by

$$\delta = \sqrt{\frac{2}{\mu_0\omega\sigma}}. \tag{1.32}$$

If we substitute σ^{eff} from eq. (1.31) for σ in eq. (1.32) and solve for δ, we obtain

$$\delta = \left(\frac{2}{\beta\mu_0\omega}\frac{\lambda}{\sigma}\right)^{1/3}. \tag{1.33}$$

Using the Drude model (eq. (1.28)) and that $\lambda = v_F/\gamma$, eq. (1.33) can be re-written as

$$\delta = \left(\frac{2}{\beta\mu_0\omega}\frac{v_F}{\varepsilon_0\omega_p^2}\right)^{1/3}. \tag{1.34}$$

For a metal, typically the temperature dependence of σ comes from that of γ, while ω_p and v_F are temperature independent. Therefore, the skin depth in eq. (1.34) is temperature independent. This explains Pippard's observation that Σ becomes independent of σ in the ASE: Σ (which depends on δ) becomes temperature independent regardless of temperature dependence in σ.

Theory for an isotropic three-dimensional Fermi surface

Soon after the publication of Pippard's results, Reuter and Sondheimer [51] published a kinetic model which has since served as the standard theory of the ASE. Here we will present the results of their work, though we will change the language and notation from that of the original work to better match the rest of this thesis.

In section 1.1, we stated that the most general form of Ohm's law is given by eq. (1.2):

$$J_i(\boldsymbol{r}) = \int d\boldsymbol{r}'\,\sigma_{ij}(\boldsymbol{r},\boldsymbol{r}')E_j(\boldsymbol{r}'). \tag{1.35}$$

If we assume translational invariance,[2] the conductivity can only depend on the relative coordinate $\boldsymbol{r}-\boldsymbol{r}'$ and eq. (1.35) becomes

$$J_i(\boldsymbol{r}) = \int d\boldsymbol{r}'\,\sigma_{ij}(\boldsymbol{r}-\boldsymbol{r}')E_j(\boldsymbol{r}'). \tag{1.36}$$

[2]The crystalline lattice breaks translational symmetry. However, the assumption of translational invariance is approximately valid at wavelengths large compared to the lattice spacing. All phenomena discussed in this thesis meet this criterion.

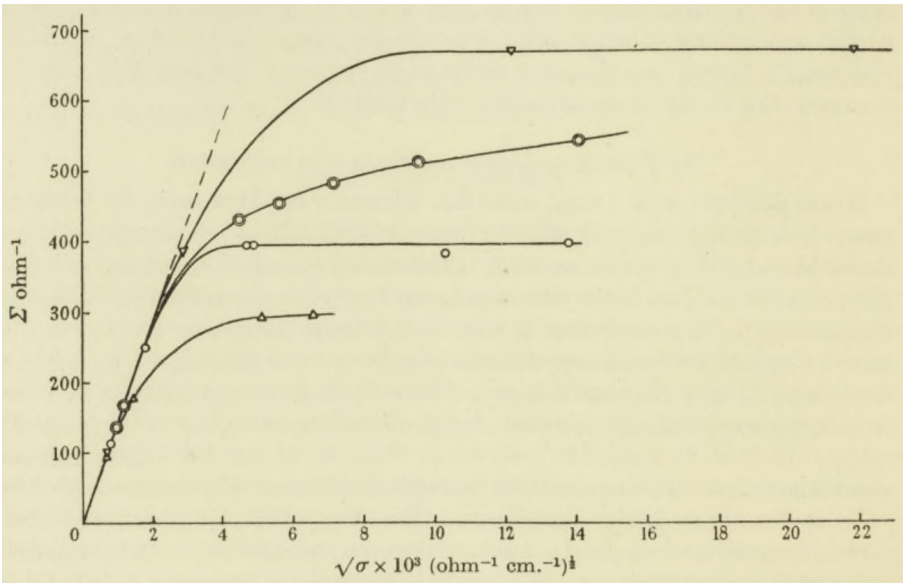

Figure 1.13: Discovery of the anomalous skin effect. Microwave surface conductance Σ versus square root of the DC conductivity σ at the same temperature. In the CSE, $\Sigma \sim \sqrt{\sigma}$, as observed for low σ. In the ASE, Σ is independent of σ, as observed for high σ. ∇ Sn, O Hg, o Ag, Δ Au. From [47].

Then, by the convolution theorem, eq. (1.36) can be expressed as

$$J_i(\boldsymbol{q}) = \sigma_{ij}(\boldsymbol{q}) E_j(\boldsymbol{q}) \tag{1.37}$$

where the wavevector $\boldsymbol{q}$ is the Fourier conjugate of $\boldsymbol{r} - \boldsymbol{r}'$.[3]

For a spherical FS and within the RTA, conductivity is given by

$$\sigma(q,\omega) = \varepsilon_0 \Omega_p^2 \frac{1}{\gamma - i\omega} Q\left(\frac{v_F q}{\gamma - i\omega}\right) \tag{1.38}$$

where

$$Q(s) = \frac{1}{2s^3}[(s^2+1)\arctan(s) - s]. \tag{1.39}$$

The function $Q(s)$ has the limiting behaviour

$$Q(s) = \begin{cases} \dfrac{1}{3} & s \ll 1 \\ \dfrac{\pi}{4s} & s \gg 1 \end{cases} \tag{1.40}$$

[3]Re-expressing eq. (1.36) as eq. (1.37) is only strictly valid when electrons scatter specularly at the sample's surface, in which case the integration in eq. (1.36) can be taken over all space. For diffuse scattering of electrons at the sample's surface, the integration is limited to the spatial domain of the sample. Nonetheless, even for diffuse scattering, experimentally-measurable quantities can be related to the wavevector dependent conductivity $\sigma_{ij}(\boldsymbol{q})$.

so that, in the parameter space of $\{\boldsymbol{q}, \omega\}$ there are three limiting cases:

$$\frac{\sigma(q,\omega)}{\varepsilon_0 \omega_p^2} = \begin{cases} \dfrac{1}{\gamma} & \gamma \gg \{\omega, v_F q\} \\ -\dfrac{1}{i\omega} & \omega \gg \{\gamma, v_F q\} \\ \dfrac{3\pi}{4 v_F q} & v_F q \gg \{\gamma, \omega\}. \end{cases} \tag{1.41}$$

For specular scattering, the surface impedance is given by

$$Z = \int_0^\infty dq \, \mathscr{A}(q,\omega) \tag{1.42}$$

with

$$\mathscr{A}(q,\omega) = \frac{1}{i\mu_0 \omega \sigma(q,\omega) - \omega^2/c^2 - q^2}. \tag{1.43}$$

We see that $Z(\omega)$ is a q-integrated function of $\sigma(q,\omega)$. In a sense, there is a feedback process involved in determining $Z(\omega)$. The conductivity determines the q values which contribute most to the integral, but the q value influences the conductivity.

Casimir and Ubbink [15] published a "phase diagram" which summarizes the resulting behaviour of the surface impedance in the phase space of $\{\gamma, \omega\}$ (fig. 1.14) as well as corresponding cartoon pictures for the physical interpretation of each regime (fig. 1.15). In the CSE, an electron undergoes many collisions within the skin layer. In the ASE, an electron propagates ballistically within the skin layer. In both the anomalous reflection and relaxation regimes, the shortest length scale is the distance an electron travels within a period of oscillation of the electromagnetic fields. The difference between these two regimes is how the MFP compares to the skin depth, which here is approximately the London penetration depth $\lambda_L \equiv c/\omega_p$. To leading order, the surface impedance has the following asymptotic behaviours:

$$Z(\omega) = \begin{cases} \mu_0 \lambda_L \gamma^{1/2} \omega^{1/2} e^{-i\pi/4} & \text{CSE} \\ \mu_0 c_1 \left(\dfrac{4\lambda_L^2 v_F}{3\pi} \right)^{1/3} \omega^{2/3} e^{-i\pi/3} & \text{ASE} \\ \mu_0 \lambda_L \omega e^{-i\pi/2} & \text{anomalous reflection \& relaxation regimes} \end{cases} \tag{1.44}$$

where c_1 depends on whether the scattering of electrons from the sample's boundaries is specular or diffuse:

$$c_1 = \begin{cases} \dfrac{4}{3\sqrt{3}} & \text{specular} \\ \dfrac{\sqrt{3}}{2} & \text{diffuse.} \end{cases} \tag{1.45}$$

In fact, the surface resistance $R = \mathrm{Re}(Z)$ differs between the anomalous reflection and relaxation regimes; in the former, it becomes highly sensitive to the nature of the boundary scattering. However, this differ-

ence only appears to sub-leading order in the asymptotic expansion.

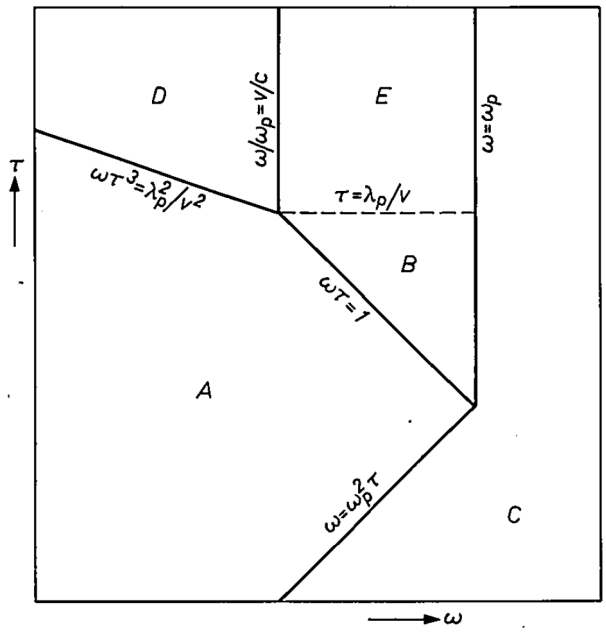

Figure 1.14: Diagram of skin effect regimes. Log-log plot of scattering time τ (inverse of scattering rate γ) versus frequency ω. (A) CSE, (B) relaxation regime, (C) transmission regime, (D) ASE, and (E) anomalous reflection regime. λ_p in the figure corresponds to our λ_L. v in the figure corresponds to our v_F. From [15].

Work on anisotropic Fermi surfaces

Sondheimer [57] went on to generalize the work of Reuter and Sondheimer [51] to spheroidal Fermi surfaces, as would arise with an anisotropic free-electron dispersion

$$\mathscr{E} = \frac{\hbar^2}{2m_a}\left(k_x^2 + k_y^2\right) + \frac{\hbar^2}{2m_c}k_z^2. \tag{1.46}$$

In this case, Sondheimer found that the asymptotic frequency dependence and phase of the surface impedance in the anomalous regime remained the same. Around the same time, Pippard [48] developed a phenomenological theory of the anomalous skin effect for an arbitrarily shaped Fermi surface. Pippard assumed that $Z \sim \omega^{2/3}$ was always true, and used the ineffectiveness concept to connect the prefactor to the curvature of the Fermi surface in a plane dependent on the orientation of the sample face being measured. Pippard went on to apply this theory to perform the first ever experimental determination of a FS, by measuring the ASE in Cu samples that had been cut in a series of directions relative to the crystal structure [49], as shown in figs. 1.16 and 1.17.

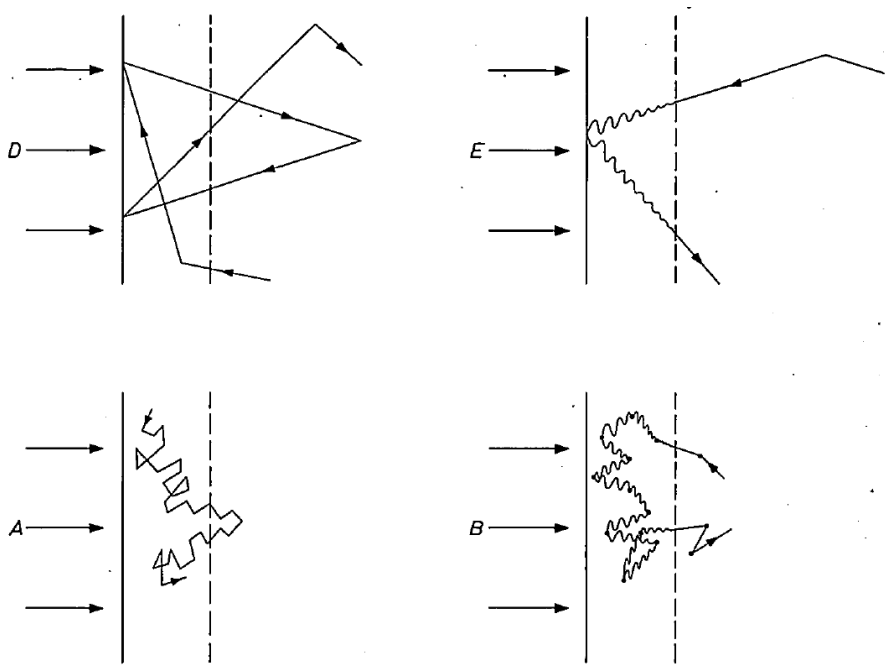

Figure 1.15: Electron trajectories in the skin layer in four skin effect regimes. Labels A, B, D and E refer to those in fig. 1.14. Horizontal arrows represent electromagnetic waves incident on the metal's surface. Dashed vertical line represents the skin layer. Zig-zag lines represent an electron undergoing collisions. Wavy lines represent oscillatory electron motion due to alternating fields. From [15].

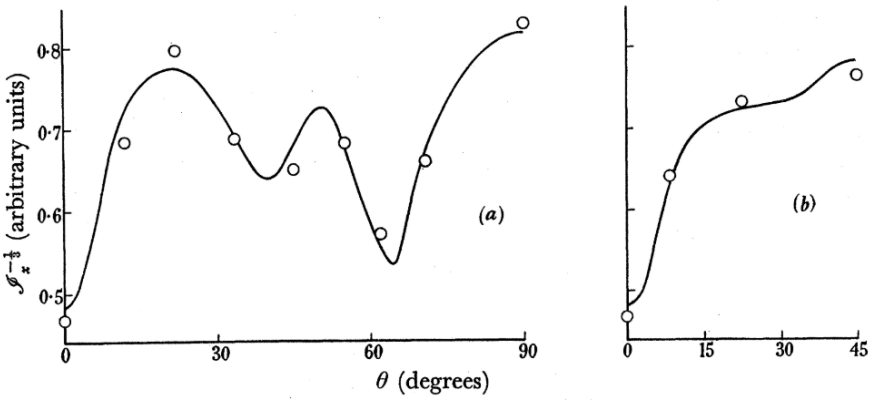

Figure 1.16: Anomalous skin effect data used to determine the Fermi surface of Cu. $\mathscr{I}_x^{-1/3}$ represents a Fermi surface integral proportional to the surface resistance. θ represents the angle of the normal to the sample's surface. In (a) it quantifies rotation about the (110) axis while in (b) it quantifies rotation about the (100) axis. In both cases, the (100) direction corresponds to $\theta = 0^\circ$. Circles are measurements and the line is a fit to a model of the Fermi surface geometry. From [49].

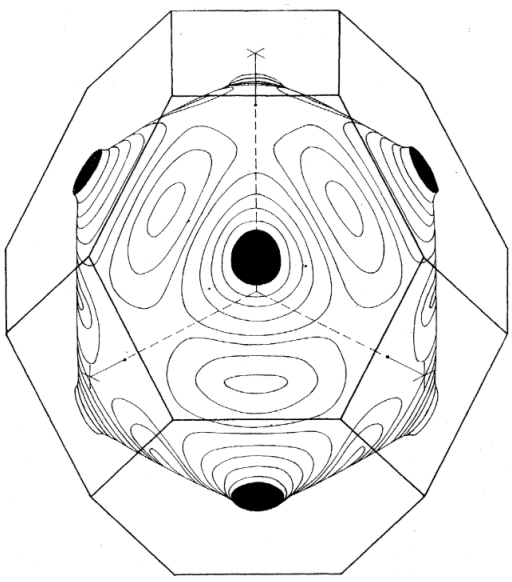

Figure 1.17: Fermi surface of Cu as determined from anomalous skin effect measurements. Based on the data from fig. 1.16. This was the first ever experimental determination of a Fermi surface. It revealed the "necks" where the Fermi surface intersects the hexagonal faces of the Brillouin zone boundaries, thus demonstrating the insufficiency of the free-electron model. From [49].

1.4.3 Viscous skin effect

Gurzhi [26] considered the AC electrodynamics of a charged, viscous fluid, as described by

$$\frac{\partial u}{\partial t} + \nu \frac{\partial^2 u}{\partial y^2} + \frac{e}{m} E_x = \gamma u, \tag{1.47}$$

where $\boldsymbol{u}$ is the flow velocity, leading to the conductivity

$$\sigma(q,\omega) = \varepsilon_0 \omega_p^2 \frac{1}{\gamma - i\omega + \nu q^2}. \tag{1.48}$$

This has the limiting behaviour

$$\frac{\sigma(q,\omega)}{\varepsilon_0 \omega_p^2} = \begin{cases} \dfrac{1}{\gamma} & \gamma \gg \{\omega, \nu q^2\} \\ -\dfrac{1}{i\omega} & \omega \gg \{\gamma, \nu q^2\} \\ \dfrac{1}{\nu q^2} & \nu q^2 \gg \{\gamma, \omega\}. \end{cases} \tag{1.49}$$

As a result, the surface impedance has a regime in which

$$Z(\omega) \propto \mu_0 \sqrt{\frac{\lambda_L^2 \nu}{\gamma}}\, \omega^{3/4} e^{-i3\pi/8} \tag{1.50}$$

which we call the Viscous Skin Effect (VSE). More recently, there have been several works considering essentially the same model in the case that ν arises from strong electron-electron interactions as described by Fermi liquid theory [22, 66, 67].

1.5 Outlook

The various instances of the size and skin effects introduced above, as they occur for an isotropic, free-electron, three-dimensional metal, are summarized in table 1.2.

The theory of the size effect for a single MFP was developed by Fuchs [24], Sondheimer [57] and for separate MR and MC mean free paths by [42]. However, in all cases, an isotropic Fermi surface was assumed. In chapter 2, we address the question of how to calculate the resistivity of a finite-size conductor with arbitrary Fermi surface. We apply these calculations to interpret our collaborators' measurements of $PdCoO_2$.

A kinetic theory of the anomalous skin effect was developed by Reuter and Sondheimer [51] for spherical Fermi surfaces, and later generalized to spheroidal Fermi surfaces by Sondheimer [57]. Pippard [47] developed an approximate theory for arbitrary Fermi surfaces. Meanwhile, a hydrodynamic theory was considered by Gurzhi [26] and later Forcella et al. [22]. In chapter 3, we develop the theory of the skin effect in the presence of both MR and MC scattering and for arbitrary Fermi surface geometry.

There exists debate as to the presence of MC scattering in $PdCoO_2$. While chapter 3 demonstrates that AC measurements of non-local electrodynamics can help differentiate these effects, there have never been AC spectroscopic measurements of non-local electrodynamics nor any AC measurements of non-local electrodynamics outside of the elemental metals. In chapter 4, we describe spectroscopic measurements of the skin effect in $PdCoO_2$ and interpret them in the context of the theory developed in chapter 3. Finally, in chapter 5 we summarize what has been learnt in this work and outline a number of future directions.

Regime	Resistivity ratio ρ/ρ_0	Surface impedance Z
Local/classical	1	$\propto \sqrt{\gamma_{\mathrm{MR}}\omega}e^{-i\pi/4}$
Viscous	$\propto \nu\lambda_{mr}/W^2$	$\propto \sqrt{\nu\lambda_{mr}}\omega^{3/4}e^{-i3\pi/8}$
Ballistic/anomalous	$\propto (\lambda_{mr}/W)/\log(\lambda_{mr}/W)$	$\propto \omega^{2/3}e^{-i\pi/3}$

Table 1.2: Summary of key size and skin effect regimes for an isotropic, free-electron, three-dimensional metal. In the middle column, ρ_0 is the bulk resistivity and W is the channel width. In the right column, ω is the angular frequency of the electromagnetic fields. ν is the viscosity and λ_{mr} is the momentum-relaxing mean free path.

Chapter 2

The size effect in $PdCoO_2$

2.1 Overview

In this chapter, we investigate the effect of Fermi surface anisotropy on the electrical conductivity of finite-size crystalline solids. The experimental results presented herein are mainly the work of Maja Bachmann while completing a doctorate under the supervision of Andrew Mackenzie and Philip Moll at the Max Planck Institute for Chemical Physics of Solids. The calculations are the work of the author.

In a bulk (i.e., infinite) crystalline solid, DC electrical conduction is described by a local relation

$$J_i = \sigma_{ij} E_j \tag{2.1}$$

where the symmetry of the local conductivity tensor σ_{ij} is dictated by the symmetries of the crystalline lattice. In principle, any finite-size solid breaks the symmetries of the crystalline lattice; in practice, this usually has no observable effect. For this effect to be observable, two ingredients are needed:

1. The electron MFP λ must be comparable to or greater than the minimum physical dimension of the solid W: $\lambda \geq W$. When this is the case, the scattering of electrons from the solid's boundaries will have an appreciable effect on its conductivity.

2. The Fermi surface must be sufficiently anisotropic.

Existing theoretical treatments of the size effect make the assumption of free-particle dispersion

$$\mathscr{E}_{\boldsymbol{k}} = \frac{\hbar^2 k^2}{2m} \tag{2.2}$$

either in 3D [24] or 2D [8], leading to an isotropic FS. Because the two materials in which the ballistic regime has been most widely studied—GaAs and graphene—have nearly isotropic Fermi surfaces, theory based on this assumption has been sufficient to date. In this chapter, we will see that the resistivity of narrow channels of $PdCoO_2$ develops anisotropy that is symmetry-forbidden in the context of the local conductivity tensor. Calculating this effect requires expanding on theoretical treatments of the size effect to include arbitrary Fermi surfaces, which is the main focus of this chapter.

2.2 Kinetic theory of electronic transport phenomena in solids, part I

The results in this chapter and the next are based in the kinetic theory of transport phenomena in solids. In order to introduce the relevant background information only as needed, we will split it between the present section and part II in the next chapter. The material in the remainder of this chapter will rely on the results of the present section (part I). The material in the next chapter will build on both the information of part I and part II.

2.2.1 Electrons in a periodic potential

In a perfect crystal, electrons are subject to a potential with the periodicity of the Bravais lattice. The single-electron Hamiltonian in this case is

$$\hat{H} = -\frac{\hbar^2}{2m}\nabla^2 + U(\boldsymbol{r}) \tag{2.3}$$

where the lattice potential U satisfies

$$U(\boldsymbol{r}+\boldsymbol{R}) = U(\boldsymbol{r}) \tag{2.4}$$

for all Bravais lattice vectors $\boldsymbol{R}$. Bloch's theorem states that the eigenstates of $\hat{H}$ are given by

$$\phi_{n\boldsymbol{k}}(\boldsymbol{r}) = e^{i\boldsymbol{k}\cdot\boldsymbol{r}} u_{n\boldsymbol{k}}(\boldsymbol{r}) \tag{2.5}$$

with corresponding eigenvalues $\mathscr{E}_{n\boldsymbol{k}}$ and where

$$u_{n\boldsymbol{k}}(\boldsymbol{r}+\boldsymbol{R}) = u_{n\boldsymbol{k}}(\boldsymbol{r}) \tag{2.6}$$

for all Bravais lattice vectors $\boldsymbol{R}$. The quantum number $\boldsymbol{k}$ is known as crystal momentum. While it acts analogously to momentum in some ways, $\hbar\boldsymbol{k} \neq \boldsymbol{p}$. Bloch states are not eigenstates of the momentum operator $\hat{\boldsymbol{p}} = (\hbar/i)\nabla$:

$$\hat{\boldsymbol{p}}\phi_{n\boldsymbol{k}} = \hbar\boldsymbol{k}\phi_{n\boldsymbol{k}} + e^{i\boldsymbol{k}\cdot\boldsymbol{r}}\frac{\hbar}{i}\nabla u_{n\boldsymbol{k}}(\boldsymbol{r}). \tag{2.7}$$

However, the velocity operator $\hat{\boldsymbol{v}} = (\hbar/mi)\nabla$ for a Bloch state has a non-zero expectation value. We will refer to this quantity simply as the Bloch state's velocity:

$$\boldsymbol{v}_{n\boldsymbol{k}} \equiv \langle\phi_{n\boldsymbol{k}}|\,\hat{\boldsymbol{v}}\,|\phi_{n\boldsymbol{k}}\rangle = \frac{1}{\hbar}\nabla_{\boldsymbol{k}}\mathscr{E}_{n\boldsymbol{k}} \tag{2.8}$$

where $\nabla_{\boldsymbol{k}}$ represents the vector differential operator with respect to crystal momentum $\boldsymbol{k}$.[1] From here on we shall suppress the band index n.

[1] We use the nabla symbol ∇ without subscript to represent the vector differential operator with respect to real space coordinate $\boldsymbol{r}$, as per convention.

2.2.2 Semiclassical dynamics

In the semiclassical model of electron dynamics, the periodic potential is treated quantum mechanically (as per section 2.2.1) while the effect of external fields is treated classically. Electrons are treated as wave packets of Bloch states. If the spread Δk of the wave packet is small compared to the Brillouin zone, then eq. (2.8) corresponds to taking the wave packet's group velocity $\nabla_{\boldsymbol{k}}\omega$. This implies a real-space spread Δr large compared with the lattice constants, which restricts the semiclassical model to external fields with wavelength much greater than the lattice constants. Electron dynamics in the absence of collisions are then described by

$$\dot{\boldsymbol{r}} = \boldsymbol{v}_{\boldsymbol{k}} = \frac{1}{\hbar}\nabla_{\boldsymbol{k}}\mathscr{E}_{\boldsymbol{k}} \tag{2.9}$$

and

$$\hbar\dot{\boldsymbol{k}} = -e\left[\boldsymbol{E}(\boldsymbol{r},t) + \frac{1}{c}\boldsymbol{v}_{\boldsymbol{k}} \times \boldsymbol{H}(\boldsymbol{r},t)\right]. \tag{2.10}$$

2.2.3 Boltzmann equation

Kinetic theory is based on a statistical description of the distribution of particles in single-particle phase space. The single-particle distribution function $f_{\boldsymbol{k}}(\boldsymbol{r},t)$ is defined such that $f_{\boldsymbol{k}}(\boldsymbol{r},t)\,d\boldsymbol{r}\,d\boldsymbol{k}/(2\pi\hbar)^3$ is the mean number of particles at time t in the phase-space element $d\boldsymbol{r}\,d\boldsymbol{k}$. (Note that we will use the common notational convention of indicating a function A of $\boldsymbol{k}$ as $A(\boldsymbol{k}) = A_{\boldsymbol{k}}$.) The Boltzmann equation tracks how the single-particle distribution function evolves with time, and is given by:

$$\left(\frac{\partial}{\partial t} + \hat{D}\right) f_{\boldsymbol{k}}(\boldsymbol{r},t) = \mathscr{C}[f_{\boldsymbol{k}}(\boldsymbol{r},t)]. \tag{2.11}$$

The streaming operator $\hat{D}$ is given by

$$\hat{D} = \dot{\boldsymbol{r}} \cdot \nabla_{\boldsymbol{r}} + \dot{\boldsymbol{k}} \cdot \nabla_{\boldsymbol{k}} \tag{2.12}$$

with $\dot{\boldsymbol{r}}$ and $\dot{\boldsymbol{k}}$ given by eqs. (2.9) and (2.10), and describes how $f_{\boldsymbol{k}}(\boldsymbol{r},t)$ changes as particles' phase space coordinates evolve continuously under semiclassical motion. The collision integral $\mathscr{C}$ describes how $f_{\boldsymbol{k}}(\boldsymbol{r},t)$ is modified when scattering events lead to a discontinuous change in particles' phase space coordinates. In other words, the left hand side tracks the semiclassical dynamics of wave packets of Bloch states—i.e., the eigenstates of the Hamiltonian for the interaction of electrons with stationary ions. On the right hand side, the collision integral takes into account the effect of electron-impurity, electron-phonon, and electron-electron interactions.

We are interested in describing the linear response to weak perturbations. Therefore, we expand the distribution function about its equilibrium value f_0:

$$f_{\boldsymbol{k}}(\boldsymbol{r},t) = f_0(\mathscr{E}_{\boldsymbol{k}}) + \delta f_{\boldsymbol{k}}(\boldsymbol{r},t) \tag{2.13}$$

where f_0 is the Fermi-Dirac distribution

$$f_0 = \frac{1}{\exp[(\mathscr{E}_{\boldsymbol{k}} - \mu)/k_B T(\boldsymbol{r})] + 1}. \tag{2.14}$$

Linear response is then found by retaining only the terms to linear order in $\delta f_{\boldsymbol{k}}$ in the Boltzmann equation. It is often convenient to write $\delta f_{\boldsymbol{k}}$ as

$$\delta f_{\boldsymbol{k}} = w_{\boldsymbol{k}} \psi_{\boldsymbol{k}} \tag{2.15}$$

where

$$w_{\boldsymbol{k}} = f_0(1 - f_0) = k_B T \left(-\frac{\partial f_0}{\partial \mathscr{E}_{\boldsymbol{k}}} \right). \tag{2.16}$$

The Boltzmann equation can be applied to describe a system's response to perturbations by an electric field, a magnetic field, a temperature gradient, or combinations thereof. We now specialize to the case of only an applied electric field, which is relevant to the work in this thesis. To linear order, we have

$$\left(\frac{\partial}{\partial t} + \hat{D} \right) f_{\boldsymbol{k}}(\boldsymbol{r},t) = \left(\frac{\partial}{\partial t} + \boldsymbol{v}_{\boldsymbol{k}} \cdot \nabla_{\boldsymbol{r}} \right) \delta f_{\boldsymbol{k}}(\boldsymbol{r},t) + e\boldsymbol{E}(\boldsymbol{r},t) \cdot \boldsymbol{v}_{\boldsymbol{k}} \left(-\frac{\partial f_0}{\partial \mathscr{E}_{\boldsymbol{k}}} \right). \tag{2.17}$$

2.2.4 Importance of the Fermi surface

It is often the case that we are interested in taking the sum over all states of some quantity A which is a function of crystal momentum $\boldsymbol{k}$. It is well-known that in the thermodynamic limit, this can be written as an integral:

$$\frac{1}{V} \sum_{\boldsymbol{k},\sigma} A_{\boldsymbol{k}} = \frac{2}{(2\pi)^d} \int d\boldsymbol{k} A_{\boldsymbol{k}}. \tag{2.18}$$

A particularly useful way of decomposing the integral over $\boldsymbol{k}$ is as an integral over energy $\mathscr{E}$ and surfaces of constant energy $\mathscr{S}(\mathscr{E})$:

$$\frac{2}{(2\pi)^d} \int d\boldsymbol{k} A_{\boldsymbol{k}} = \frac{2}{(2\pi)^d} \int d\mathscr{E} \int_{\mathscr{S}(\mathscr{E})} dS A_{\boldsymbol{k}} \tag{2.19}$$

We will frequently encounter functions of the type

$$A_{\boldsymbol{k}} = \left(-\frac{\partial f_0}{\partial \mathscr{E}_{\boldsymbol{k}}} \right) a_{\boldsymbol{k}}. \tag{2.20}$$

We may then make use of the property of the Fermi-Dirac distribution that

$$\lim_{T \to 0} -\frac{\partial f_0}{\partial \mathscr{E}_{\boldsymbol{k}}} \to \delta(\mathscr{E}_{\boldsymbol{k}} - \mathscr{E}_F) \tag{2.21}$$

so that

$$\frac{2}{(2\pi)^d} \int d\boldsymbol{k} A_{\boldsymbol{k}} = \frac{2}{(2\pi)^d} \int_{\mathscr{S}_F} \frac{dS}{\hbar v_{\boldsymbol{k}}} a_{\boldsymbol{k}} \tag{2.22}$$

where $\mathscr{S}_F$ is the Fermi surface, defined by $\mathscr{S}(\mathscr{E}_{\boldsymbol{k}} = \mathscr{E}_F)$ where $\mathscr{E}_F$ is the Fermi energy. The limit in eq. (2.21) is valid whenever $T \ll T_F$ where $T_F \equiv \mathscr{E}_F/k_B$. In metals, the high density of electrons means that $T \ll T_F$ over all temperatures typically accessible in a laboratory. This illustrates the centrality of the Fermi surface in determining the transport properties of metals.

2.2.5 The relaxation time approximation

The collision integral tracks how scattering processes modify the distribution function for the state $\boldsymbol{k}$. We will defer a more in-depth treatment of its properties until chapter 3; for now, we will describe it in broad strokes. Its exact form depends on the type of scattering process being considered. In general, the integrand of the collision integral depends on

1. the electronic distribution function for state $\boldsymbol{k}$,
2. the distribution functions for the other states involved in the scattering process, and
3. the scattering probabilities for scattering an electron into and out of state $\boldsymbol{k}$.

The scattering probabilities for a given process are commonly determined via Fermi's golden rule. The integral is over the quantum numbers specifying the other states involved in the scattering processes, so that one arrives at a description of the net effect of all scattering on the distribution function for state $\boldsymbol{k}$.

In the presence of scattering, the Boltzmann equation is an integro-differential equation for $f_{\boldsymbol{k}}$ which is in general difficult to solve. To overcome this, a common approach is to use the RTA to make estimates of transport properties. The RTA corresponds to assuming that the collision integral $\mathscr{C}$ is given by

$$\mathscr{C} = -\frac{1}{\tau}\,\delta f_{\boldsymbol{k}}. \tag{2.23}$$

Once this phenomenological assumption is made, the Boltzmann equation can then be solved more straightforwardly. Physically, eq. (2.23) means that collisions act to decay the entire non-equilibrium distribution function $\delta f_{\boldsymbol{k}}$ at a rate $1/\tau$. An example of a scenario for which the RTA is strictly justified is the scattering of electrons from a dilute ensemble of randomly-distributed, point-like impurities.

2.2.6 The Drude model

Before moving on, it is instructive to see how the Drude model can be derived from the Boltzmann equation. The Drude model arises under two assumptions: (1) the RTA, and (2) the assumption that the distribution function is uniform, i.e., independent of $\boldsymbol{r}$, so that $\nabla_{\boldsymbol{r}}\delta f_{\boldsymbol{k}} = 0$. Using $\psi_{\boldsymbol{k}}(t) = \psi_{\boldsymbol{k}}(\omega)e^{-i\omega t}$, the Boltzmann equation can be solved straightforwardly as

$$\psi_{\boldsymbol{k}}(\omega) = -\frac{e}{k_B T}\boldsymbol{E}(\omega)\cdot\boldsymbol{v}\frac{1}{1/\tau - i\omega}. \tag{2.24}$$

Electrical current is given by

$$\boldsymbol{J} = -2e\frac{1}{(2\pi)^d}\int d\boldsymbol{k}\,\boldsymbol{v}_{\boldsymbol{k}}\delta f_{\boldsymbol{k}} \tag{2.25}$$

and using the local version of Ohm's law, we find

$$\sigma_{ij}(\omega) = \varepsilon_0 \omega_{p,ij}^2 \frac{1}{1/\tau - i\omega} \tag{2.26}$$

where

$$\varepsilon_0 \omega_{p,ij}^2 \equiv \frac{2e^2}{(2\pi)^d} \int d\boldsymbol{k} \left(-\frac{\partial f_0}{\partial \mathscr{E}_{\boldsymbol{k}}} \right) v_{\boldsymbol{k}i} v_{\boldsymbol{k}j}. \tag{2.27}$$

2.3 Theory of the size effect for a metal of arbitrary dispersion

In this section, we develop the theory of the size effect for an arbitrary three-dimensional dispersion. We then show that this general treatment reproduces the results of previous treatments for isotropic Fermi surfaces [8, 24]. Next, we apply the result to the case of $PdCoO_2$.

We consider a channel of width W extending from $y = 0$ to $y = W$. The distribution function then has the form

$$f_{\boldsymbol{k}}(y) = f_0 + \delta f_{\boldsymbol{k}}(y) \tag{2.28}$$

where, as before, f_0 is the equilibrium distribution function and $\delta f_{\boldsymbol{k}}(y)$ represents a small deviation from equilibrium. The linearized Boltzmann equation in the presence of an electric field $\boldsymbol{E}$ and in the RTA is given by

$$v_{\boldsymbol{k}y} \frac{\partial \delta f_{\boldsymbol{k}}(y)}{\partial y} + \frac{e}{\hbar} \boldsymbol{E} \cdot \boldsymbol{v}_{\boldsymbol{k}} \left(-\frac{\partial f_0}{\partial \mathscr{E}_{\boldsymbol{k}}} \right) = -\frac{1}{\tau} \delta f_{\boldsymbol{k}}(y). \tag{2.29}$$

We assume diffuse scattering at the boundaries of the channel. Using $\delta f_{\boldsymbol{k}}^{+(-)}$ to denote the non-equilibrium distribution function of electrons with $v_{\boldsymbol{k}y} > 0$ ($v_{\boldsymbol{k}y} < 0$), this imposes the conditions

$$\begin{aligned} \delta f_{\boldsymbol{k}}^{+}(0) &= 0 \\ \delta f_{\boldsymbol{k}}^{-}(W) &= 0. \end{aligned} \tag{2.30}$$

This has the solution

$$\delta f_{\boldsymbol{k}}(y) = \frac{e\tau}{\hbar} \boldsymbol{E} \cdot \boldsymbol{v}_{\boldsymbol{k}} \left(\frac{-\partial f_0}{\partial \mathscr{E}_{\boldsymbol{k}}} \right) g_{\boldsymbol{k}}(y) \tag{2.31}$$

where

$$g_{\boldsymbol{k}}(y) = \begin{cases} 1 - \exp\left(-\dfrac{y}{\tau v_{\boldsymbol{k}y}} \right) & v_{\boldsymbol{k}y} > 0, \\ 1 - \exp\left(\dfrac{W - y}{\tau v_{\boldsymbol{k}y}} \right) & v_{\boldsymbol{k}y} < 0. \end{cases} \tag{2.32}$$

We define a spatially-dependent conductivity tensor by

$$\sigma_{ij} \equiv \frac{J_i(y)}{E_j}. \tag{2.33}$$

Using eqs. (2.22) and (2.25), we get

$$\sigma_{ij}(y) = \frac{e^2\tau}{4\pi^3}\int_{\mathscr{S}_F} dS \frac{v_{\boldsymbol{k}i}v_{\boldsymbol{k}j}}{v_{\boldsymbol{k}}} g_{\boldsymbol{k}}(y). \tag{2.34}$$

Next we obtain a spatially-averaged conductivity tensor as

$$\begin{aligned}\bar{\sigma}_{ij} &\equiv \frac{1}{W}\int_0^W dy\, \sigma_{ij}(y) \\ &= \frac{e^2\tau}{4\pi^3}\int_{S_F} dS \frac{v_{\boldsymbol{k}i}v_{\boldsymbol{k}j}}{v_{\boldsymbol{k}}} \bar{g}_{\boldsymbol{k}}(y)\end{aligned} \tag{2.35}$$

where

$$\bar{g}_{\boldsymbol{k}} = 1 - \frac{\tau|v_{\boldsymbol{k}y}|}{W}\left[1 - \exp\left(-\frac{W}{\tau|v_{\boldsymbol{k}y}|}\right)\right]. \tag{2.36}$$

The bulk conductivity tensor $\sigma_{ij}^{\text{bulk}}$ in eq. (2.26) can be obtained from eq. (2.35) by setting $\bar{g}_{\boldsymbol{k}} = 1$. Resistivity is found by inverting the spatially-averaged conductivity tensor:

$$\rho_{ij} = \bar{\sigma}_{ij}^{-1}. \tag{2.37}$$

For a Fermi surface $\mathscr{S}_F$ parametrized by the Fermi vector $\boldsymbol{k}_F(g,h)$ with $g \in (g_1, g_2)$ and $h \in (h_1, h_2)$, we define a vector

$$\boldsymbol{n}(g,h) = \frac{\partial \boldsymbol{k}_F(g,h)}{\partial g} \times \frac{\partial \boldsymbol{k}_F(g,h)}{\partial h} \tag{2.38}$$

where $n(g,h) = |\boldsymbol{n}(g,h)|$. Then the integral over the Fermi surface is given by

$$\int_{\mathscr{S}_F} dS = \int_{g_1}^{g_2} dg \int_{h_1}^{h_2} dh\, n(g,h). \tag{2.39}$$

The unit vector normal to the Fermi surface—and thus parallel to the Fermi velocity—is given by

$$\hat{\boldsymbol{n}}(g,h) = \frac{\boldsymbol{n}(g,h)}{n(g,h)}. \tag{2.40}$$

2.3.1 Check against previous results

Spherical Fermi surface

For a free-particle dispersion (eq. (2.2)) in 3D, the Fermi surface is parameterized by

$$\boldsymbol{k}_F(\theta,\phi) = k_F\left[\sin\theta\cos\phi\,\boldsymbol{i} + \sin\theta\sin\phi\,\boldsymbol{j} + \cos\phi\,\boldsymbol{k}\right] \tag{2.41}$$

and the Fermi velocity can be found from eqs. (2.2) and (2.8) as

$$\boldsymbol{v}_F(\theta,\phi) = v_F\left[\sin\theta\cos\phi\,\boldsymbol{i} + \sin\theta\sin\phi\,\boldsymbol{j} + \cos\theta\,\boldsymbol{k}\right] \tag{2.42}$$

where $mv_F = \hbar k_F$. Inserting eqs. (2.41) and (2.42) into eqs. (2.35) and (2.36) reproduces exactly the results of Fuchs [24], as in eqs. (1.14) and (1.15).

Circular Fermi surface

For a free-particle dispersion in 2D, we have

$$\boldsymbol{k}_F(\phi) = k_F\,[\cos\phi\,\boldsymbol{i} + \sin\phi\,\boldsymbol{j}] \tag{2.43}$$

and

$$\boldsymbol{v}_F(\phi) = v_F\,[\cos\phi\,\boldsymbol{i} + \sin\phi\,\boldsymbol{j}] \tag{2.44}$$

which, when combined with eqs. (2.35) and (2.36), produce the results of Beenakker and van Houten [8], as in eq. (1.16).

2.4 $PdCoO_2$

2.4.1 Fermi surface parameterization

In a two-dimensional approximation, the Fermi surface of $PdCoO_2$ can be parametrized as

$$\boldsymbol{k}_F(\phi, \phi_0, k_z) = \rho(\phi - \phi_0 - \pi/2)[\cos\phi\,\boldsymbol{i} + \sin\phi\,\boldsymbol{j}] + k_z\boldsymbol{k} \tag{2.45}$$

with

$$\rho(\phi) = \sum_\mu k_\mu \cos(\mu\phi) \tag{2.46}$$

where the k_μ are listed in table 2.1. k_z is the component of $\boldsymbol{k}_F$ along the c-axis of the crystal structure (cf. fig. 1.3), with $k_z \in (-\pi/d, \pi/d)$ and $d = 17.743/3$ Å. ϕ is the angle in the plane perpendicular to the c-axis with $\phi \in (0, 2\pi)$, while ϕ_0 parameterizes the channel orientation by controlling the orientation of the FS relative to the coordinate system.

Here we assume that the Fermi velocity has a constant magnitude v_F:

$$\boldsymbol{v}_{\boldsymbol{k}} = v_F\hat{\boldsymbol{n}}_{\boldsymbol{k}} \tag{2.47}$$

for $\boldsymbol{k}$ on the FS $\mathscr{S}_F$, as justified by electronic structure calculations [44] and ARPES measurements [60]. We use $v_F = 7.5 \times 10^5$ m/s.

μ	k_μ [Å^{-1}]
0	0.9518
6	0.0444
12	0.0048

Table 2.1: Fermi surface harmonics of $PdCoO_2$ in two-dimensional parameterization from [60].

2.4.2 Results

Using only the shape of the Fermi surface, we can calculate $\rho_{ij}/\rho_{xx}^{\text{bulk}}$, the ratio of the resistivity ρ_{ij} of a finite width channel to the longitudinal resistivity ρ_{xx}^{bulk} of an infinitely wide channel. (Here the subscript x refers to any direction in the plane perpendicular to the c-axis.) This depends only on W/λ, the ratio of the channel width W to the bulk MFP $\lambda = v_F/\tau$. The calculated angle-dependence of the longitudinal and transverse resistivities is shown in fig. 2.1 for two values of W/λ.

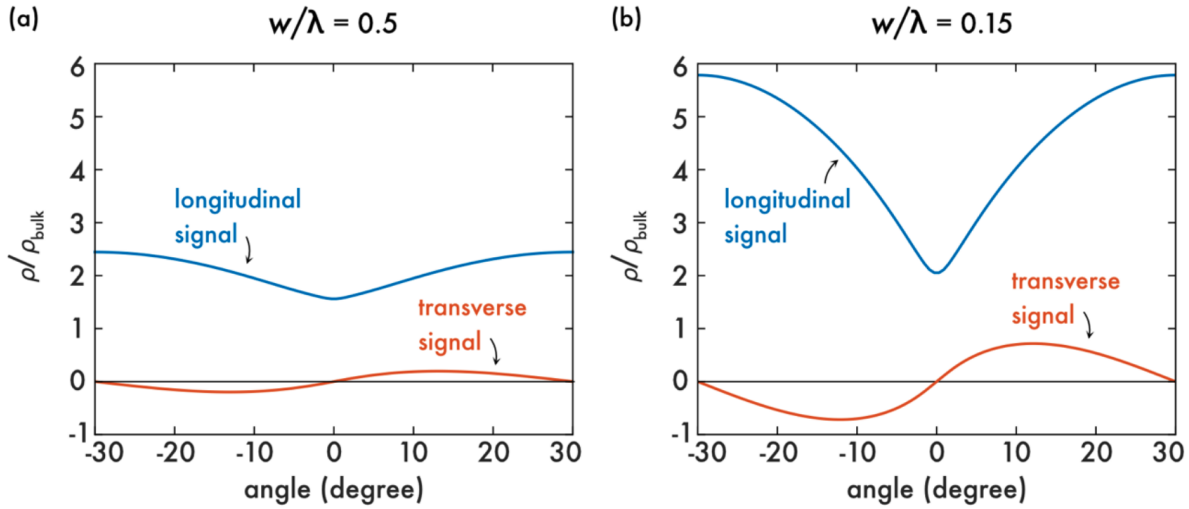

Figure 2.1: Calculated angle dependent resistivity of $PdCoO_2$ at two ratios of channel width W to MFP λ. Resistivity ρ is normalized by the bulk value ρ_{bulk}. Angles are defined in fig. 2.2 a. From [5].

2.5 Experimental results

2.5.1 Longitudinal resistivity

A FIB was used to create multiple channels of differing orientations in series in the same sample of $PdCoO_2$, as shown in fig. 2.2a. Based on the symmetry of the crystalline lattice, the full unique angular range corresponds to a range of 30°. This range was spanned by four equally-spaced channel angles.

The temperature-dependent apparent MFP $\lambda^{\text{apparent}}$, as inferred from resistivity measurements, becomes width dependent at low temperature, as shown in fig. 2.2b. This is consistent with the onset of the size effect at low temperature as the bulk MFP λ^{bulk} becomes greater than W. In other words, the channels are in a diffusive (local) regime at high temperature and a ballistic regime at low temperature. As the channels enter the ballistic regime, anisotropy develops in the resistivity, as shown in fig. 2.2c.

While the properties of the Fermi surface alone determine how ρ varies with W/λ, the experimental data is for $\rho(T)$ at fixed W. To make a direct comparison, it is necessary to determine $\lambda(T)$. To do so, we fit the temperature-dependent resistivity of a 155 μm channel, as reported in [44], which we assume to be in the bulk limit. The data and fit are shown in fig. 2.3. We fit to a phenomenological temperature

dependence

$$\rho_{xx}^{\text{bulk}}(T) = \rho_\alpha + \frac{\rho_\beta}{e^{T_0/T} - 1}. \tag{2.48}$$

The second term, which has a Bose-Einstein-like form, was motivated by the observed $\rho_{xx}^{\text{bulk}} \sim e^{-T/T_0}$ behaviour at low temperature and $\rho_{xx}^{\text{bulk}} \sim T$ behavior at high temperature. We then determined $\tau(T)$ from the fit to $\rho_{xx}^{\text{bulk}}(T)$. Having done so, it was then possible to perform the calculations shown in fig. 2.2d, showing a good match to the data in fig. 2.2c.

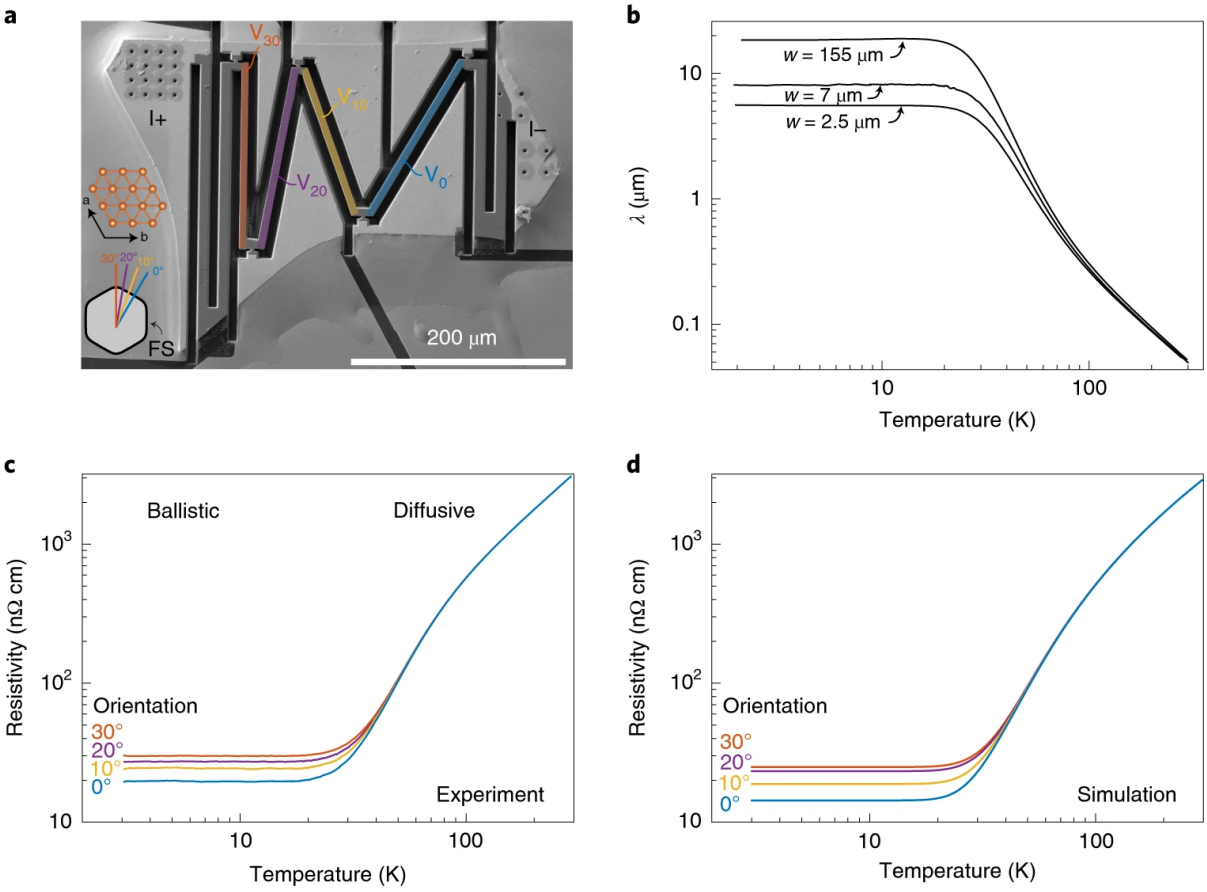

Figure 2.2: Anisotropic in-plane resistivity in narrow channels of $PdCoO_2$. (a) Scanning electron microscope image of FIB microstructured crystal comprising four channel orientations. The real-space orientation of the FS relative to the crystal is shown. (b) Temperature-dependent MFP for the 30° orientation at several channel thicknesses, inferred from the measured resistivity. The MFP becomes width dependent at low temperature, indicating the onset of the ballistic regime (c) Measured temperature-dependent longitudinal resistivities of the four channels. The resistivities are equal in the diffusive regime but become anisotropic in the ballistic regime. (d) Results from kinetic calculation. From [5].

It is instructive to compare the FS of $PdCoO_2$ with an isotropic FS. As shown in fig. 2.4a, the difference in FS geometry alone does not appear to be drastic. However, the FS geometry determines the distribution of velocity directions, as the Fermi velocity is perpendicular to the Fermi surface. As shown in fig. 2.4b, the distribution of velocity directions in $PdCoO_2$ is strongly peaked along six directions,

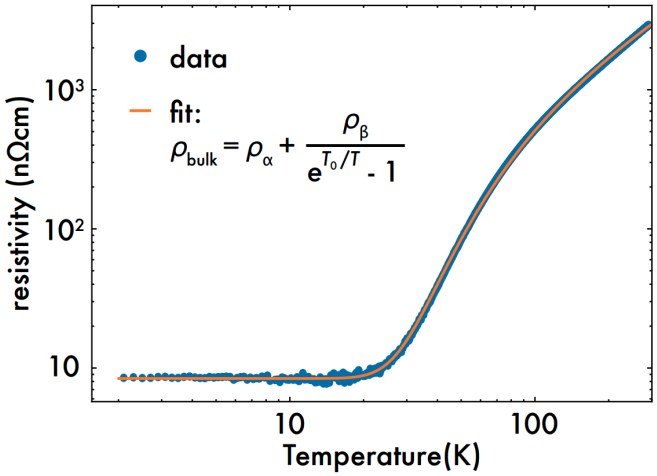

Figure 2.3: Phenomenological fit to temperature-dependent bulk resistivity. This fit was used to obtain a temperature-dependent bulk MFP to use as an input to the kinetic calculation. From [5].

corresponding to the flat portions of the FS.

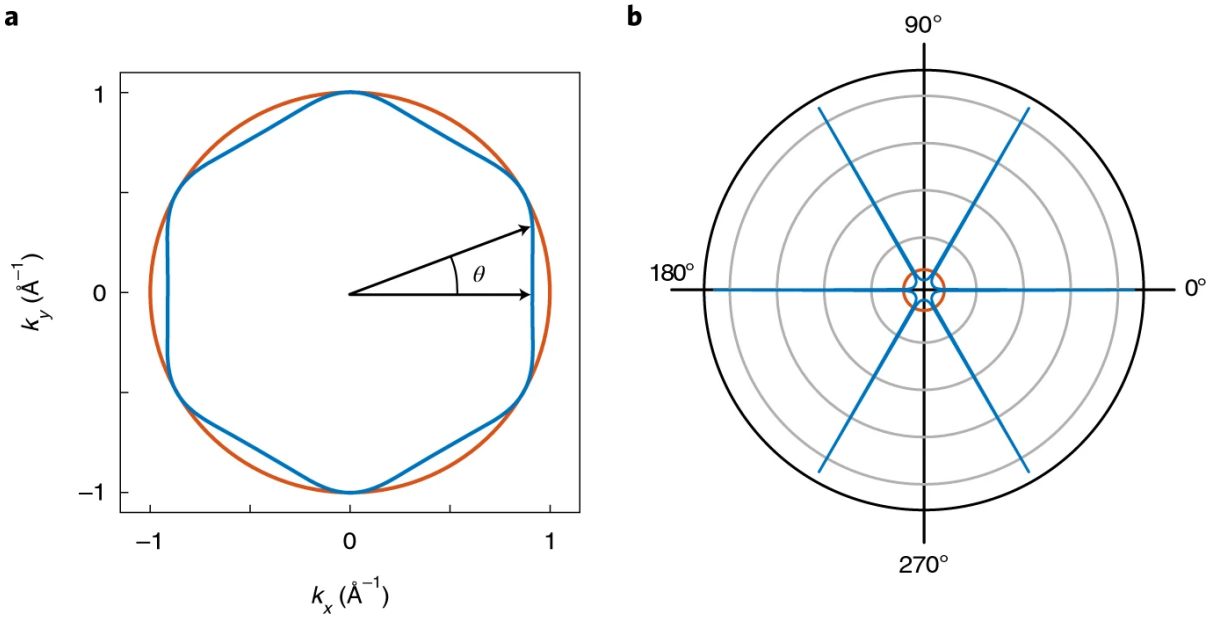

Figure 2.4: Effect of Fermi surface geometry on distribution of Fermi velocity directions. (a) The FS of $PdCoO_2$ (blue) compared with a circular FS (red). The relative difference in the magnitude of the Fermi momentum at a given angle is never large. (b) Angular distribution of Fermi velocity directions for the two FSs for equal normalization. Each facet of the $PdCoO_2$ Fermi surface results in a large number of states with the same Fermi velocity direction. From [5].

Figure 2.5 illustrates how a velocity direction distribution peaked along six direction plays out in narrow channels of different orientations. For a circular FS, collisions at the boundary limit the MFP

of essentially all of the electrons, in a manner which is dependent on the angle that they make with the channel. The orientation of the channel makes no difference. For a hexagonal FS, there exists an orientation in which a third of electrons make no collisions with the sample's boundaries and are thus unaffected by variations in the channel's width.

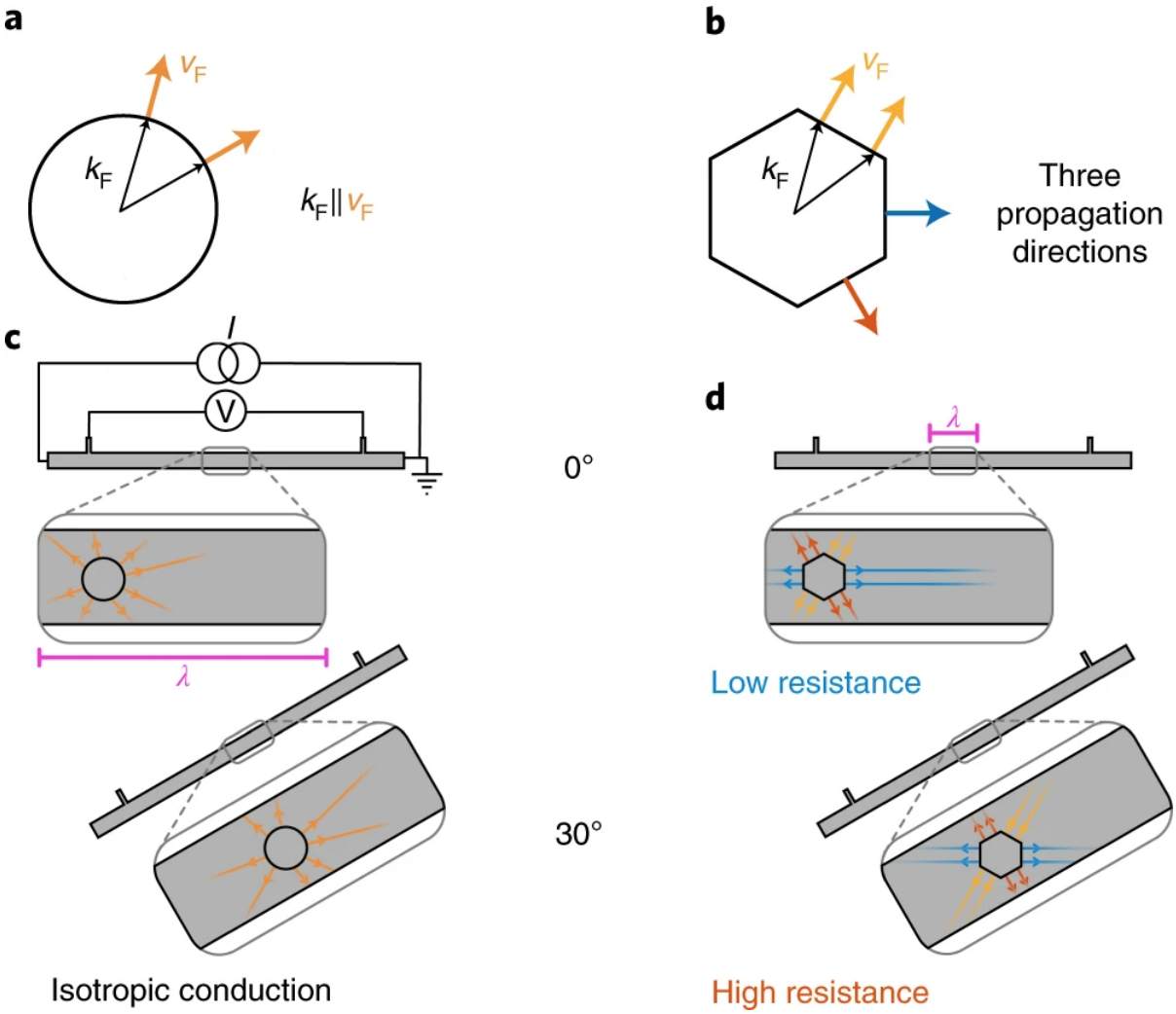

Figure 2.5: Ballistic electron propagation for a circular versus hexagonal Fermi surface. (a) For a circular FS, the Fermi velocity v_F and Fermi momentum k_F are always parallel. (b) For a hexagonal FS they are not, and there are only three possible Fermi velocity directions. (c) The resistance of a channel does not depend on its orientation for a circular FS. (d) For a hexagonal FS, a channel aligned parallel to a direction of electron propagation will show lower resistance than a channel aligned perpendicular to a direction of electron propagation. From [5].

2.5.2 Transverse resistivity

When a channel is oriented along a low-symmetry direction, there will be an imbalance in the number of electrons propagating toward the two boundaries of the channel, as illustrated in fig. 2.6a. While for

a bulk sample, symmetry dictates that the transverse resistivity must be zero, in a finite sample, one might expect that it would be possible for a transverse voltage to develop in this situation. One further expects that channels tilted by equal but opposite angles away from a high-symmetry direction would yield equal but opposite transverse voltages. To test these ideas, two channels were fabricated at $\pm 3°$, as shown in fig. 2.6b.

Figure 2.6c shows the results of these measurements. At low temperature, when the MFP becomes comparable to the channel width, a transverse voltage develops. As expected, the voltages for the two opposite angles are equal in magnitude and opposite in sign. As shown in fig. 2.6d, calculations capture the temperature dependence of the data well.

One complication arises in the comparison of data and calculations here. The measurements of transverse resistivity are inevitably contaminated by a longitudinal contribution as a result of imperfect contact alignment. In subtracting this contribution from the measurement, it is assumed that the transverse signal is zero at high temperature. In order to facilitate a direct comparison between data and calculations, the calculations were given the same treatment as the data and were set to zero at 120 K.

2.6 Outlook

The present work invites several future research directions. The delafossite metals $PtCoO_2$ and $PdCrO_2$ have similarly nearly-hexagonal Fermi surfaces, but with slightly different warping parameters. Furthermore, they are also of sufficiently high conductivity that the ballistic regime is attainable. This provides the opportunity to test the predictive ability of the theoretical treatment developed in this chapter. Similar effects are likely to occur in other classes of high-conductivity materials as well. For example, gated bilayer graphene has a nearly triangular Fermi surface.

An interesting consequence of this work is the potential for finite-size-induced anisotropy to confound studies of other phenomena. For example, the area of nematic and smectic electronic phases is of widespread interest within condensed matter physics. Here, resistivity anisotropy that is forbidden by the symmetry of the crystalline lattice is often used as evidence for electronically-driven symmetry-breaking states. In the Weyl semi-metal WP_2, the MFP is sufficiently long that even as-grown crystals may enter the ballistic regime.

Technologically, these results are relevant to the miniaturization of electrical conductors. With sufficiently small dimensions, conductors will enter the ballistic regime even at elevated temperatures. In this case, their conductivity will be limited by boundary scattering. The present results show that conductivity can be significantly increased by channel orientation. This effect is expected to grow with decreasing width, as shown in fig. 2.7.

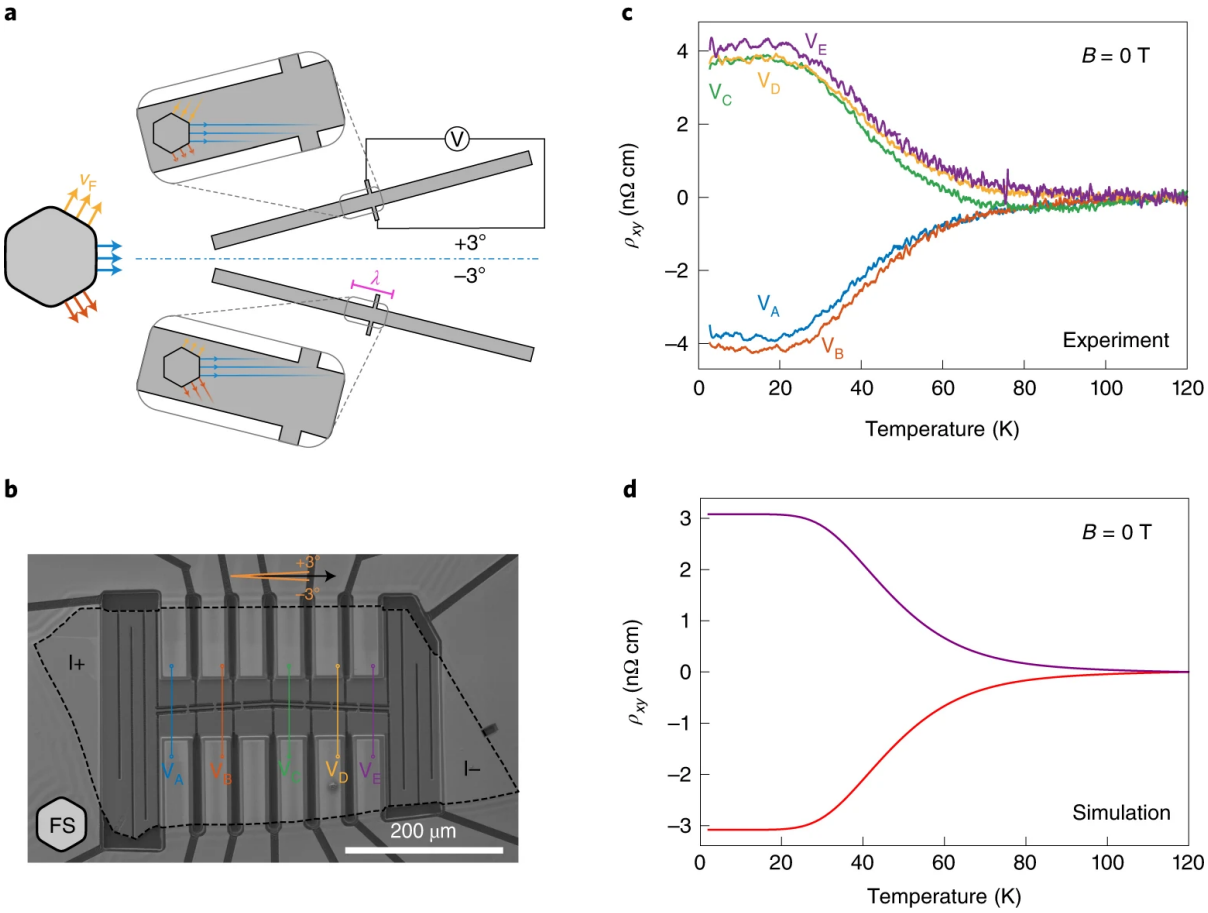

Figure 2.6: Transverse resistivity in narrow channels of $PdCoO_2$. (a) Illustration of electron propagation for channels oriented along low-symmetry directions of the FS. (b) Scanning electron microscope image of FIB microstructured crystal for the measurement of transverse resistivity at $\pm 3°$. (c) Measured transverse resistivity. A non-zero transverse resistivity develops at low temperature with antisymmetric values at $\pm 3°$. The values are not strongly dependent on the position of the voltage contacts along the current path. (d) Result of kinetic calculation. From [5].

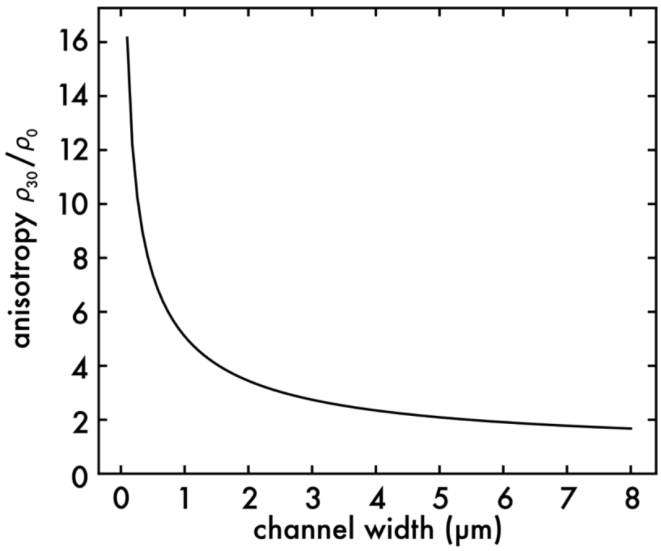

Figure 2.7: Calculated width-dependent resistivity anisotropy in $PdCoO_2$ at 2 K. The anisotropy is predicted to increase rapidly with decreasing channel width. From [5].

Chapter 3

Generalized theory of the skin effect

3.1 Overview

In this chapter, we develop a generalized theory of the skin effect. Relative to previous theoretical work on the skin effect, we introduce two generalizations:

1. *Arbitrary Fermi surface geometry*. The original kinetic theory of the Boltzmann equation by Reuter and Sondheimer [51] considered a spherical FS. Later, Sondheimer [57] generalized to a spheroidal FS. While Pippard [48] developed a phenomenological theory that was argued to cover arbitrary FS, the treatment was not rooted in kinetic theory. Here we develop a kinetic theory valid for arbitrary FS. As we will see, the results highlight the limitations of Pippard's phenomenological treatment.

2. *Arbitrary rates of momentum-relaxing and momentum-conserving scattering*. Theories of the skin effect to date can be grouped into two categories. On the one hand, the works of Reuter and Sondheimer [51], Sondheimer [57], while based in kinetic theory, made the RTA—assuming a single relaxation rate for the decay of the non-equilibrium distribution function. As a result, these works cannot capture the effect of frequent MC collisions, leading to viscous behaviour. On the other hand, the works of Forcella et al. [22], Gurzhi [26] were rooted in a continuum description of a charged, viscous fluid. By design, these works capture viscous behaviour. However, they are rooted in an a priori assumption of frequent MC scattering. Being rooted in a continuum description, they cannot capture the ASE, which is an inherently statistical phenomenon. By incorporating separate MC and MR scattering rates into a kinetic description, we are able to capture all regimes.

3.2 Kinetic theory of transport phenomena in solids, part II

Before presenting our results, we will cover some additional background from kinetic theory, building on that presented in chapter 2.

3.2.1 Conserved quantities

Consider a quantity $\chi_{\boldsymbol{k}}$ which is a function of crystal momentum. An associated density ρ_χ can be defined as

$$\rho_\chi(\boldsymbol{r},t) \equiv \int_{\boldsymbol{k}} \chi_{\boldsymbol{k}} f_{\boldsymbol{k}}(\boldsymbol{r},t) \tag{3.1}$$

where $f_{\boldsymbol{k}}$ is the electronic distribution function and $\int_{\boldsymbol{k}}$ represents an integral over all Bloch states

$$\int_{\boldsymbol{k}} \cdots \equiv \frac{2}{(2\pi)^d} \int d\boldsymbol{k} \cdots \tag{3.2}$$

where a factor of 2 has been included to account for spin degeneracy. An associated current J_χ can be defined as

$$\boldsymbol{J}_\chi(\boldsymbol{r},t) \equiv \int_{\boldsymbol{k}} \boldsymbol{v}_{\boldsymbol{k}} \chi_{\boldsymbol{k}} f_{\boldsymbol{k}}(\boldsymbol{r},t). \tag{3.3}$$

Multiplying the distribution function by $\chi_{\boldsymbol{k}}$ and integrating the Boltzmann equation over all Bloch states yields

$$\frac{\partial \rho_\chi(\boldsymbol{r},t)}{\partial t} + \nabla \cdot \boldsymbol{J}_\chi(\boldsymbol{r},t) = \mathscr{C}\left[\chi_{\boldsymbol{k}} f_{\boldsymbol{k}}(\boldsymbol{r},t)\right]. \tag{3.4}$$

A quantity $\chi_{\boldsymbol{k}}$ which has the property that $\mathscr{C}[\chi_{\boldsymbol{k}}] = 0$ is known as a collisional invariant. Equation (3.4) expresses that collisional invariants are conserved quantities.

3.2.2 Properties of linearized collision operator

In section 2.2.3, we introduced the idea of expanding the distribution function about equilibrium as

$$f_{\boldsymbol{k}}(\boldsymbol{r},t) = f_0 + w_{\boldsymbol{k}} \psi_{\boldsymbol{k}} \tag{3.5}$$

where $w_{\boldsymbol{k}} = f_0(1-f_0)$ and f_0 is the Fermi-Dirac distribution function. We discussed that linear response was described by keeping only terms up to linear order in $\psi_{\boldsymbol{k}}$. The linear term of the collision integral is known as the linearized collision operator $\hat{C}$ and is formally defined by

$$\hat{C}\psi_{\boldsymbol{k}} \equiv \frac{1}{w_{\boldsymbol{k}}} \int_{\boldsymbol{k}'} \frac{\delta \mathscr{C}_{\boldsymbol{k}}}{\delta \psi_{\boldsymbol{k}'}} \psi_{\boldsymbol{k}'}. \tag{3.6}$$

It can be shown that $\hat{C}$ is Hermitian and negative semidefinite, meaning that it is diagonalizable and its eigenvalues are real and are ≤ 0 [55]. In this context, collisional invariants can be understood as eigenfunctions of $\hat{C}$ with an eigenvalue of zero.

3.2.3 Surface impedance

For a semi-infinite medium occupying the half-space $z > 0$, surface impedance is defined as

$$Z = \left.\frac{E_x}{H_y}\right|_{z=0}. \tag{3.7}$$

Using Faraday's law, this becomes

$$Z(\omega) = i\mu_0\omega \left.\frac{E_x(z,\omega)}{\partial E_x(z,\omega)/\partial z}\right|_{z=0}. \tag{3.8}$$

The electric field is governed by the wave equation

$$\left(\frac{\partial^2}{\partial z^2} + \frac{\omega^2}{c^2}\right) E_x(z,\omega) = -i\mu_0\omega J_x(z,\omega). \tag{3.9}$$

The relevant boundary conditions for a kinetic theory relate to the specular or diffuse nature of the scattering of the electrons at the sample's surface. We have

$$J_x^{s(d)}(z,\omega) = \int_{-\infty(0)}^{\infty} dz' \sigma_{xx}(z-z',\omega) E_x(z',\omega) \tag{3.10}$$

where the superscript s (d) denotes specular (diffuse) scattering. Defining the photon propagator as

$$\mathscr{A} = \frac{1}{i\mu_0\omega\sigma(q,\omega) + \omega^2/c^2 - q^2} \tag{3.11}$$

we have that [51]

$$Z^s(\omega) = i\mu_0\omega\frac{2}{\pi}\int_0^{\infty} dq\, \mathscr{A}(q,\omega) \tag{3.12}$$

and [21]

$$Z^d(\omega) = i\mu_0\omega\left(\int_0^{\infty} dq \ln\left[\frac{1}{q^2\mathscr{A}(q,\omega)}\right]\right)^{-1}. \tag{3.13}$$

3.3 Results

3.3.1 Collision operator

Here we are interested in deriving a collision operator for which momentum is relaxed at a higher rate than all other modes of the non-equilibrium distribution function. We take the Fourier transform of the Boltzmann equation and keep terms to linear order in $\psi_{\boldsymbol{k}}$ to obtain

$$[-i\omega + i\boldsymbol{v}_{\boldsymbol{k}}\cdot\boldsymbol{q}]\psi_{\boldsymbol{k}}(\boldsymbol{q},\omega) + \frac{e}{k_B T}\boldsymbol{E}(\boldsymbol{q},\omega)\cdot\boldsymbol{v}_{\boldsymbol{k}} = -\hat{C}_{\boldsymbol{k}}\psi_{\boldsymbol{k}}(\boldsymbol{q},\omega) \tag{3.14}$$

where $\hat{C}$ is the linearized collision operator

$$\hat{C}\psi_{\boldsymbol{k}} = \frac{1}{w_{\boldsymbol{k}}}\int_{\boldsymbol{k}'}\frac{\delta\mathscr{C}_{\boldsymbol{k}}}{\delta\psi_{\boldsymbol{k}'}}\psi_{\boldsymbol{k}'}. \tag{3.15}$$

Let $\psi_{\boldsymbol{k}}$ be an element of a function space with inner product

$$\langle\phi|\psi\rangle = \int_{\boldsymbol{k}} w_{\boldsymbol{k}}\phi^*_{\boldsymbol{k}}\psi_{\boldsymbol{k}}. \tag{3.16}$$

We use as a basis the complete and orthonormal set of eigenfunctions $\chi_{\boldsymbol{k},m}$ of the collision operator:

$$\hat{C}\chi_{\boldsymbol{k},m} = \gamma_{\boldsymbol{k},m}\chi_{\boldsymbol{k},m} \tag{3.17}$$

with

$$\sum_m \left|\chi_{\boldsymbol{k},m}\right\rangle \left\langle\chi_{\boldsymbol{k},m}\right| = 1 \tag{3.18}$$

and

$$\left\langle\chi_{\boldsymbol{k},m}\middle|\chi_{\boldsymbol{k},m'}\right\rangle = \delta_{m,m'}. \tag{3.19}$$

We assume that the eigenfunctions $\chi_{\boldsymbol{k},m}$ include

$$\chi_{\boldsymbol{k},0} = c_0 \tag{3.20}$$

and

$$\chi_{\boldsymbol{k},i} = c_i c_0 \hat{v}_{\boldsymbol{k},i} \tag{3.21}$$

where $i \in \{x,y,z\}$ and that the eigenvalue spectrum is given by

$$\gamma_{\boldsymbol{k},m} = \begin{cases} 0 & m = 0 \\ \gamma^{\mathrm{mr}}_{\boldsymbol{k},i} & m = i \\ \gamma^{\mathrm{mc}}_{\boldsymbol{k}} & \text{otherwise.} \end{cases} \tag{3.22}$$

This describes a scenario in which collisions conserve charge, relax momentum in the i direction at a rate $\gamma^{\mathrm{mr}}_{\boldsymbol{k},i}$, and relax all other modes at a rate $\gamma^{\mathrm{mc}}_{\boldsymbol{k}}$. Using eq. (3.18), we may write the collision operator as

$$\hat{C} = \gamma^{\mathrm{mc}}_{\boldsymbol{k}}(1 - \left|\chi_{\boldsymbol{k},0}\right\rangle \left\langle\chi_{\boldsymbol{k},0}\right|) - \sum_i \delta\gamma_{\boldsymbol{k},i} \left|\chi_{\boldsymbol{k},i}\right\rangle \left\langle\chi_{\boldsymbol{k},i}\right| \tag{3.23}$$

where $\delta\gamma_{\boldsymbol{k},i} \equiv \gamma^{\mathrm{mc}}_{\boldsymbol{k}} - \gamma^{\mathrm{mr}}_{\boldsymbol{k},i}$.

Throughout, we will use that

$$\int_{\boldsymbol{k}} \cdots \equiv \frac{2}{(2\pi)^d}\int d\boldsymbol{k} \cdots = \frac{2}{(2\pi)^d\hbar}\int_0^\infty d\mathscr{E} \int_{\mathscr{S}(\mathscr{E})} \frac{dS}{v_{\boldsymbol{k}}} \cdots . \tag{3.24}$$

Furthermore, we will assume that $T \ll T_F$ such that

$$\int_{\boldsymbol{k}} -\frac{\partial f_0}{\partial \mathscr{E}_{\boldsymbol{k}}} \cdots = \frac{2}{(2\pi)^d\hbar}\int_{\mathscr{S}_F} \frac{dS}{v_{\boldsymbol{k}}} \cdots \tag{3.25}$$

where $\mathscr{S}_F$ is the Fermi surface $\mathscr{S}(\mathscr{E}_{\boldsymbol{k}} = \mathscr{E}_F)$. Finally, for simplicity, we will assume that on the Fermi surface the magnitude of the velocity is isotropic: $\boldsymbol{v}_{\boldsymbol{k}} = v_F\hat{\boldsymbol{v}}_{\boldsymbol{k}}$ for $\boldsymbol{k}$ on $\mathscr{S}_F$.

The constants c_0 and c_i are determined by eq. (3.19). We find

$$\frac{1}{c_0^2} = \frac{2k_BT}{(2\pi)^d\hbar v_F} S_F \tag{3.26}$$

and

$$\frac{1}{c_i^2} = \int_{\mathscr{S}_F} \frac{dS}{S_F} \hat{v}_{\boldsymbol{k}i}^2 \tag{3.27}$$

where

$$S_F \equiv \int_{\mathscr{S}_F} dS. \tag{3.28}$$

We can now rewrite the collision integral as

$$\hat{C}\psi_{\boldsymbol{k}} = \gamma_{\boldsymbol{k}}^{\mathrm{mc}} \psi_{\boldsymbol{k}} - \gamma_{\boldsymbol{k}}^{\mathrm{mc}} n_0 - \sum_i c_i^2 \delta\gamma_{\boldsymbol{k},i} \hat{v}_{\boldsymbol{k}i} p_i \tag{3.29}$$

where

$$n_0 \equiv \int_{\mathscr{S}_F} \frac{dS}{S_F} \psi_{\boldsymbol{k}} \tag{3.30}$$

and

$$p_i \equiv \int_{\mathscr{S}_F} \frac{dS}{S_F} \hat{v}_{\boldsymbol{k}i} \psi_{\boldsymbol{k}} \tag{3.31}$$

The solution to the Boltzmann equation is then

$$\psi_{\boldsymbol{k}}(\boldsymbol{q},\omega) = \frac{-\frac{e}{k_B T}\boldsymbol{E}(\boldsymbol{q},\omega)\cdot\boldsymbol{v}_{\boldsymbol{k}} + \gamma_{\boldsymbol{k}}^{\mathrm{mc}} n_0(\boldsymbol{q},\omega) + \sum_i c_i^2 \delta\gamma_{\boldsymbol{k},i}\, \hat{v}_{\boldsymbol{k}i}\, p_i(\boldsymbol{q},\omega)}{\gamma_{\boldsymbol{k}}^{\mathrm{mc}} - i\omega + i\boldsymbol{v}_{\boldsymbol{k}}\cdot\boldsymbol{q}}. \tag{3.32}$$

Because we are ultimately interested in finding the transverse conductivity, as is relevant to measurements of surface impedance, we take $\boldsymbol{E} \perp \boldsymbol{q}$ with $\boldsymbol{E} \parallel \hat{\boldsymbol{\alpha}}$ and $\boldsymbol{q} \parallel \hat{\boldsymbol{\beta}}$. We define

$$\langle \mathscr{A} \rangle \equiv \int_{\mathscr{S}_F} \frac{dS}{S_F} \frac{\mathscr{A}}{\gamma_{\boldsymbol{k}}^{\mathrm{mc}} - i\omega + i v_F \hat{v}_{\boldsymbol{k}\beta} q}. \tag{3.33}$$

We find that

$$\begin{pmatrix} \gamma_{\boldsymbol{k}}^{\mathrm{mc}}\langle 1\rangle - 1 & c_\beta^2\delta\gamma_{\boldsymbol{k},\beta}\langle \hat{v}_{\boldsymbol{k}\beta}\rangle & c_\alpha^2\delta\gamma_{\boldsymbol{k},\alpha}\langle \hat{v}_{\boldsymbol{k}\alpha}\rangle & c_\gamma^2\delta\gamma_{\boldsymbol{k},\gamma}\langle \hat{v}_{\boldsymbol{k}\gamma}\rangle \\ \gamma_{\boldsymbol{k}}^{\mathrm{mc}}\langle \hat{v}_{\boldsymbol{k}\beta}\rangle & c_\beta^2\delta\gamma_{\boldsymbol{k},\beta}\langle \hat{v}_{\boldsymbol{k}\beta}^2\rangle - 1 & c_\alpha^2\delta\gamma_{\boldsymbol{k},\alpha}\langle \hat{v}_{\boldsymbol{k}\beta}\hat{v}_{\boldsymbol{k}\alpha}\rangle & c_\gamma^2\delta\gamma_{\boldsymbol{k},\gamma}\langle \hat{v}_{\boldsymbol{k}\beta}\hat{v}_{\boldsymbol{k}\gamma}\rangle \\ \gamma_{\boldsymbol{k}}^{\mathrm{mc}}\langle \hat{v}_{\boldsymbol{k}\alpha}\rangle & c_\beta^2\delta\gamma_{\boldsymbol{k},\beta}\langle \hat{v}_{\boldsymbol{k}\alpha}\hat{v}_{\boldsymbol{k}\beta}\rangle & c_\alpha^2\delta\gamma_{\boldsymbol{k},\alpha}\langle \hat{v}_{\boldsymbol{v}\alpha}^2\rangle - 1 & c_\gamma^2\delta\gamma_{\boldsymbol{k},\gamma}\langle \hat{v}_{\boldsymbol{k}\alpha}\hat{v}_{\boldsymbol{k}\gamma}\rangle \\ \gamma_{\boldsymbol{k}}^{\mathrm{mc}}\langle \hat{v}_{\boldsymbol{k}\gamma}\rangle & c_\beta^2\delta\gamma_{\boldsymbol{k},\beta}\langle \hat{v}_{\boldsymbol{k}\gamma}\hat{v}_{\boldsymbol{k}\beta}\rangle & c_\alpha^2\delta\gamma_{\boldsymbol{k},\alpha}\langle \hat{v}_{\boldsymbol{k}\gamma}\hat{v}_{\boldsymbol{k}\alpha}\rangle & c_\gamma^2\delta\gamma_{\boldsymbol{k},\gamma}\langle \hat{v}_{\boldsymbol{k}\gamma}^2\rangle - 1 \end{pmatrix} \begin{pmatrix} n_0 \\ p_\beta \\ p_\alpha \\ p_\gamma \end{pmatrix} = \frac{e}{k_B T} E_y v_F \begin{pmatrix} \langle \hat{v}_{\boldsymbol{k}\alpha}\rangle \\ \langle \hat{v}_{\boldsymbol{k}\beta}\hat{v}_{\boldsymbol{k}\alpha}\rangle \\ \langle \hat{v}_{\boldsymbol{k}\alpha}^2\rangle \\ \langle \hat{v}_{\boldsymbol{k}\gamma}\hat{v}_{\boldsymbol{k}\alpha}\rangle \end{pmatrix} \tag{3.34}$$

and assuming three mirror planes, we get

$$\begin{pmatrix} \gamma_{\boldsymbol{k}}^{\mathrm{mc}}\langle 1\rangle - 1 & c_\beta^2\delta\gamma_{\boldsymbol{k},\beta}\langle \hat{v}_{\boldsymbol{k}\beta}\rangle & 0 & 0 \\ \gamma_{\boldsymbol{k}}^{\mathrm{mc}}\langle \hat{v}_{\boldsymbol{k}\beta}\rangle & c_\beta^2\delta\gamma_{\boldsymbol{k},\beta}\langle \hat{v}_{\boldsymbol{k}\beta}^2\rangle - 1 & 0 & 0 \\ 0 & 0 & c_\alpha^2\delta\gamma_{\boldsymbol{k},\alpha}\langle \hat{v}_{\boldsymbol{v}\alpha}^2\rangle - 1 & 0 \\ 0 & 0 & 0 & c_\gamma^2\delta\gamma_{\boldsymbol{k},\gamma}\langle \hat{v}_{\boldsymbol{k}\gamma}^2\rangle - 1 \end{pmatrix} \begin{pmatrix} n_0 \\ p_\beta \\ p_\alpha \\ p_\gamma \end{pmatrix} = \frac{e}{k_B T} E_y v_F \begin{pmatrix} 0 \\ 0 \\ \langle \hat{v}_{\boldsymbol{k}\alpha}^2\rangle \\ 0 \end{pmatrix} \tag{3.35}$$

To ensure that $\psi_{\boldsymbol{k}} = 0$ when $\boldsymbol{E} = 0$, we must also have $n_0 = p_\beta = 0$. For p_α we have

$$p_\alpha = -\frac{eEv_F}{k_BT}\frac{\langle \hat{v}^2_{\boldsymbol{k}\alpha}\rangle}{1 - c^2_\alpha \delta\gamma_{\boldsymbol{k},\alpha}\langle \hat{v}^2_{\boldsymbol{k}\alpha}\rangle} \tag{3.36}$$

so that

$$\psi_{\boldsymbol{k}} = -\frac{eEv_F}{k_BT}\frac{1}{\gamma^{\mathrm{mc}}_{\boldsymbol{k}} - i\omega + iqv_F\hat{v}_{\boldsymbol{k}\beta}}\frac{\hat{v}_{\boldsymbol{k}\alpha}}{1 - c^2_{\hat{\boldsymbol{y}}}\delta\gamma_{\boldsymbol{k},\alpha}\langle \hat{v}^2_{\boldsymbol{k}\alpha}\rangle}. \tag{3.37}$$

3.3.2 Reference Fermi surface geometries

In the remainder of this chapter, we will apply the kinetic theory developed in the previous section to several Fermi surface geometries, working in two dimensions for simplicity.

1. *Circular*: We are interested in the behaviour of a perfectly isotropic Fermi surface.

2. *Square*: A square Fermi surface is in some sense the most "extreme" anisotropic Fermi surface geometry (which still possesses two mirror planes): it has the most anisotropic distribution of Fermi velocity directions.

3. *Hexagonal*: A hexagonal geometry lies in between the square and circular geometries in terms of the anisotropy of the distribution of Fermi velocity directions. This makes the hexagonal geometry useful for exploring the sensitivity of conductivity and surface impedance to anisotropy. The hexagonal geometry is also of interest because it approximates the Fermi surface of $PdCoO_2$. However, the focus of this chapter will be on a more general analysis; we defer considerations specific to $PdCoO_2$ to the following chapter.

3.3.3 Conductivity

Electrical current is given by

$$\boldsymbol{J} = -e\int_{\boldsymbol{k}} \boldsymbol{v}_{\boldsymbol{k}} f_{\boldsymbol{k}}. \tag{3.38}$$

Via

$$J_i(\boldsymbol{q},\omega) = \sigma_{ij}(\boldsymbol{q},\omega)E_j(\boldsymbol{q},\omega) \tag{3.39}$$

and assuming $\delta\gamma_{\boldsymbol{k},\alpha}$ to be $\boldsymbol{k}$-independent, we find the non-local transverse conductivity for $\boldsymbol{E} \parallel \hat{\boldsymbol{\alpha}}$ and $\boldsymbol{q} \parallel \hat{\boldsymbol{\beta}}$ as

$$\sigma(q,\omega) = \varepsilon_0\Omega_p^2\frac{G_0(q,\omega)}{1 - c^2_\alpha\delta\gamma_\alpha G_0(q,\omega)} \tag{3.40}$$

where

$$G_0(q,\omega) \equiv \langle \hat{v}^2_{\boldsymbol{k}\alpha}\rangle = \int_{\mathscr{S}_F}\frac{dS}{S_F}\frac{\hat{v}^2_{\boldsymbol{k}\alpha}}{\gamma^{\mathrm{mc}}_{\boldsymbol{k}} - i\omega + iqv_F\hat{v}_{\boldsymbol{k}\beta}}. \tag{3.41}$$

and

$$\Omega_p^2 \equiv \sum_i \omega^2_{p,ii} \tag{3.42}$$

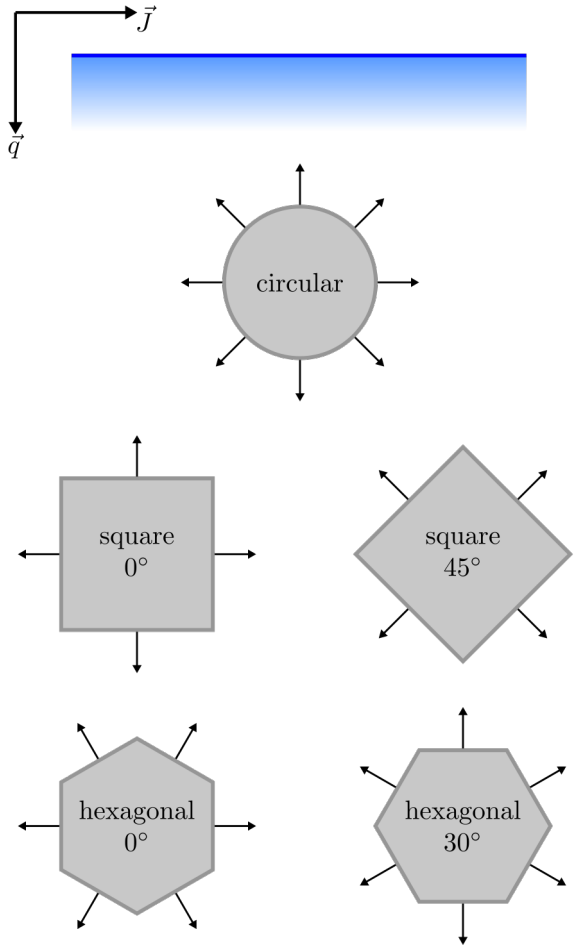

Figure 3.1: Reference Fermi surface geometries. We will apply our kinetic theory to these five geometries. Their labels and orientation relative to the current $\vec{J}$ and wavevector $\vec{q}$ directions are shown. The sample's surface is represented in dark blue and the skin layer in light blue.

where plasma frequency is given by

$$\varepsilon_0 \omega_{p,ii}^2 = \frac{e^2 v_F^2}{{c_0}^2 k_B T} \int_{\mathscr{S}_F} \frac{dS}{S_F} \hat{v}_{\boldsymbol{k}i}^2. \tag{3.43}$$

We note that eq. (3.41) can be rewritten as

$$G(\boldsymbol{q}, \omega) = \frac{1}{\gamma^{\mathrm{mc}} - i\omega} g\left(\frac{q v_F}{\gamma^{\mathrm{mc}} - i\omega}\right) \tag{3.44}$$

with

$$g(s) = \int_{\mathscr{S}_F} \frac{dS}{S_F} \frac{\hat{v}_{\boldsymbol{k}\alpha}^2}{1 + i\hat{v}_{\boldsymbol{k}\beta}\, s}. \tag{3.45}$$

For each of the reference Fermi surfaces considered here

$$\lim_{s\to 0} g(s) = \frac{1}{2}. \tag{3.46}$$

The full form of $g(s)$ for each geometry as well as the asymptotic behaviour as $s \to \infty$ is given in table 3.1.

Fermi surface	$g(s)$	$\lim_{s\to\infty} g(s)$
Circular	$\frac{\sqrt{s^2+1}-1}{s^2}$	$\frac{1}{s}$
Square 0°	$\frac{1}{2}$	$\frac{1}{2}$
Hexagonal 0°	$\frac{2+s^2}{4+3s^2}$	$\frac{1}{3}$
Square, 45°	$\frac{1}{2+s^2}$	$\frac{1}{s^2}$
Hexagonal, 30°	$\frac{2}{4+s^2}$	$\frac{2}{s^2}$

Table 3.1: $g(s)$ for reference Fermi surface geometries (cf. eq. (3.45)). In all cases, $\lim_{s\to 0} g(s) = 1/2$. The behaviour of the non-local transverse conductivity $\sigma(q,\omega)$ is set by the behaviour of $g(s = qv_F/(\gamma^{\mathrm{mc}} - i\omega))$ (cf. eqs. (3.40) and (3.44)).

Circular

In the limit that $qv_F \ll 1$, the conductivity reduces to that of the Drude model:

$$\frac{\sigma(q,\omega)}{\varepsilon_0\Omega_p^2} = \frac{1}{2}\frac{1}{\gamma_{mr} - i\omega}. \tag{3.47}$$

We see that for local electrodynamics, the conductivity is unaffected by MC scattering. In the limit that $qv_F \gg 1$, we have

$$\frac{\sigma(q,\omega)}{\varepsilon_0\Omega_p^2} = \frac{1}{v_F q} + \frac{\gamma_{mr} - i\omega + \delta\gamma}{(v_F q)^2} \tag{3.48}$$

To leading order, we have

$$\frac{\sigma(q,\omega)}{\varepsilon_0\Omega_p^2} = \frac{1}{v_F q}. \tag{3.49}$$

While the prefactor is different, this $\sigma \sim 1/q$ behaviour for $qv_F \gg 1$ is exactly what is responsible for the ASE in three dimensions for a spherical FS (cf. eq. (1.41)). In the limit that $\delta\gamma \to \infty$, we have

$$\frac{\sigma(q,\omega)}{\varepsilon_0\Omega_p^2} = \frac{\delta\gamma}{(v_F q)^2} \tag{3.50}$$

This is the behaviour associated with a viscous, charged fluid with viscosity

$$\nu = \frac{v_F^2}{2\delta\gamma} \tag{3.51}$$

(cf. section 1.4.3).

Polygonal

We note that for the four polygonal geometries, $g(s)$ takes the form

$$g(s) = \frac{n_0 + n_2 s^2}{2n_0 + d_2 s^2} \tag{3.52}$$

where n_0, n_2, and d_2 are non-negative integers. This results in a conductivity of the form

$$\frac{\sigma(q,\omega)}{\varepsilon_0 \Omega_p^2} = \frac{(\gamma_{mr} - i\omega + \delta\gamma)^2 n_0 + n_2 (v_F q)^2}{2(\gamma_{mr} - i\omega)(\gamma_{mr} - i\omega + \delta\gamma)^2 n_0 + [(\gamma_{mr} - i\omega + \delta\gamma) d_2 - 2\delta\gamma n_2](v_F q)^2} \tag{3.53}$$

for which we will now analyze the limiting behaviors. For all geometries, the conductivity reduces to the Drude conductivity for $qv_F \ll 1$:

$$\frac{\sigma(q,\omega)}{\varepsilon_0 \Omega_p^2} = \frac{1}{2} \frac{1}{\gamma_{mr} - i\omega}. \tag{3.54}$$

For $qv_F \gg 1$, several different cases emerge.

The square 45° and hexagonal 30° geometries have $n_2 = 0$ and $d_2 = 1$. When $qv_F \gg 1$, we have

$$\frac{\sigma(q,\omega)}{\varepsilon_0 \Omega_p^2} = n_0 \frac{\delta\gamma + \gamma_{mr} - i\omega}{(v_F q)^2}. \tag{3.55}$$

where n_0 is 1 for the square 45° geometry and 2 for the hexagonal 30° geometry.

For the square 0° geometry, σ is independent of $v_F q$ and is exactly the Drude conductivity, eq. (3.54), for all parameter ranges. For the hexagonal 0° geometry with $qv_F \gg 1$ we have

$$\frac{\sigma(q,\omega)}{\varepsilon_0 \Omega_p^2} = \frac{1}{3(\gamma_{mr} - i\omega + \delta\gamma) - 2\delta\gamma} + \frac{2(\gamma_{mr} - i\omega + \delta\gamma)^3}{[3(\gamma_{mr} - i\omega + \delta\gamma) - 2\delta\gamma]^2 (v_F q)^2}. \tag{3.56}$$

To leading order, we have:

$$\frac{\sigma(q,\omega)}{\varepsilon_0 \Omega_p^2} = \frac{1}{3} \frac{1}{\gamma_{mr} + \delta\gamma/3 - i\omega} \tag{3.57}$$

Similarly to the square 0° geometry, the conductivity takes a Drude form except with the substitutions

$$\omega_p^2 \to \frac{2}{3}\omega_p^2 \tag{3.58}$$

and

$$\gamma_{mr} \to \gamma_{mr} + \delta\gamma/3 \tag{3.59}$$

However, for $\delta\gamma \to \infty$, we see that viscous behaviour emerges:

$$\frac{\sigma(q,\omega)}{\varepsilon_0 \Omega_p^2} = \frac{2\delta\gamma}{(v_F q)^2}. \tag{3.60}$$

3.3.4 Surface impedance

We now proceed to examine the behaviour of the surface impedance Z based on the conductivities σ of Section 3.3.3. We analyzed σ as a function of $\boldsymbol{q}$ and ω. Z is a q-integrated function of σ. The weight of the contribution from a given q is determined self-consistently via Maxwell's equations, and will depend on ω, v_F, ω_p, γ_{mr} and $\delta\gamma$. For a metal, it is appropriate to take the limit $T \ll T_F$ at experimentally accessible temperatures, and so one can expect v_F and ω_p to be temperature independent. Therefore, it is instructive to examine the behaviour of Z as a function of ω and γ_i. In practice, one would actually measure $Z(\omega, T) = Z(\omega, \gamma_i(T))$.

First, we examine where crossovers in the surface impedance may possibly occur based on dimensional analysis. The boundaries are displayed in Figure 3.2. Table 3.2 identifies the regimes which were identified and named by Casimir and Ubbink [15]. Table 3.3 identifies the equations describing the boundaries for the left side of Figure 3.2. Table 3.4 identifies the equations describing the boundaries for the right side. Finally, Table 3.5 outlines the definitions of the various relevant length scales.

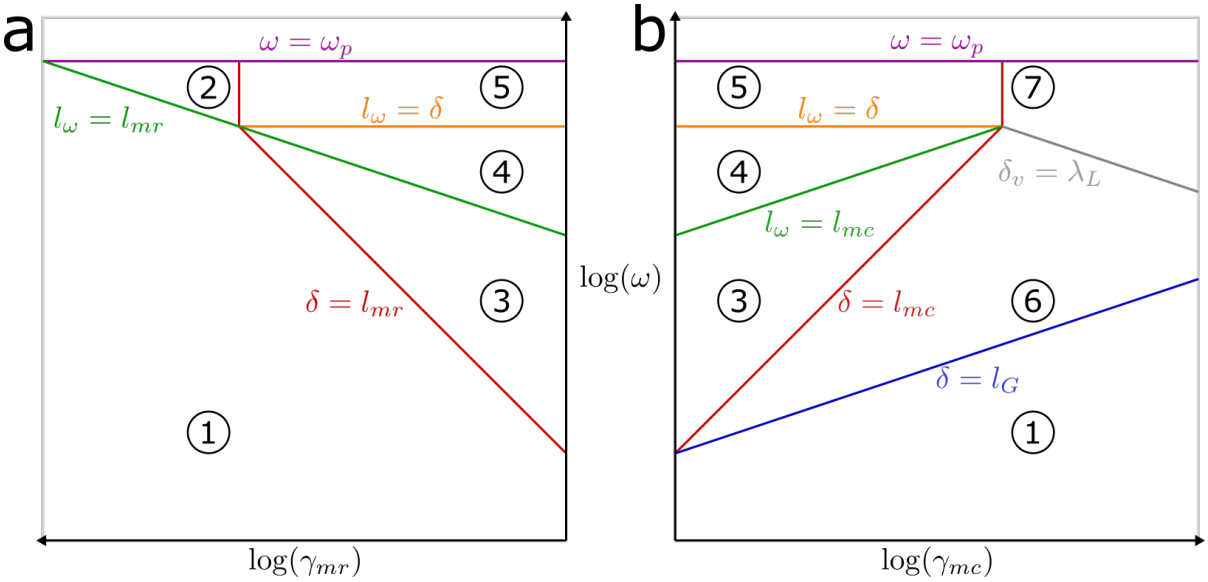

Figure 3.2: Possible crossover locations in the skin effect, as deduced by comparing the various length scales involved. (a) Log-log plot of MR scattering rate versus frequency. (b) Log-log plot of MC scattering rate versus frequency. The two plots meet at their minimum horizontal values, i.e. the fixed value of γ_{mc} for plot (a) is the minimum value of γ_{mc} for plot(b) and vice versa.

Region	Existing name
1	Classical skin effect
2	Relaxation
3	–*
4	–*
5	Anomalous reflection
6	Viscous skin effect
7	–

* Known together as anomalous skin effect.

Table 3.2: Existing nomenclature in literature.

Boundary	By length scales	By $\omega - \gamma_{mr}$ relation
1 - 2, 3 - 4	$l_\omega = l_{mr}$	$\omega = \gamma_{mr}$
1 - 3	$\delta = l_{mr}$	$\omega = (\lambda_L/v_F)^2\gamma_{mr}^3$
2 - 5	$\delta = l_{mr}$	$\gamma_{mr} = v_F/\lambda_L$
4 - 5	$l_\omega = \delta$	$\omega = v_F/\lambda_L$

Table 3.3: Definitions of boundaries in $\omega - \gamma_{mr}$ diagram.

Boundary	By length scales	By $\omega - \gamma_{mc}$ relation
3 - 4	$l_\omega = l_{mc}$	$\omega = \gamma_{mc}$
3 - 6	$\delta = l_{mc}$	$\omega = (\lambda_L/v_F)^2\gamma_{mc}^3$
5 - 7	$\delta = l_{mc}$	$\gamma_{mc} = v_F\lambda_L$
4 - 5	$l_\omega = \delta$	$\omega = v_F/\lambda_L$
1 - 6	$\delta = l_G$	$\omega = (\lambda_L/v_F)^2\gamma_{mr}^2\gamma_{mc}$
6 - 7	$\delta_v = \lambda_L$	$\omega = (v_F/\lambda_L)^2\gamma_{mc}^{-1}$

Table 3.4: Definitions of boundaries in $\omega - \gamma_{mc}$ diagram.

Symbol	Definition	Meaning
λ_L	c/ω_p	London penetration depth
l_ω	v_F/ω	Distance travelled during one oscillation of fields
l_G	$\sqrt{l_{mc}l_{mr}}$	Gurzhi length
δ_v	$\left(\lambda_L^2 l_\omega l_{mc}\right)^{1/4}$	Skin depth in viscous regime

Table 3.5: Definitions of length scales.

Next, we examine the actual behaviour of the surface impedance for circular, square, and hexagonal Fermi surfaces. It is instructive to note that the asymptotic forms of the conductivity found in the

previous section can always be written in the form

$$\frac{\sigma(q,\omega)}{\varepsilon_0\omega_p^2} \approx a(v_F q)^{-\alpha}[\gamma^{1-\beta}(-i\omega)^{\beta}]^{\alpha-1} \tag{3.61}$$

where $\alpha \in \{0,1,2\}$, $\beta \in \{0,1\}$, a is a dimensionless constant, and γ is some linear combination of γ_{mr} and $\delta\gamma$. For specular (diffuse) boundary scattering, this corresponds to an asymptotic impedance of the form

$$Z^{s(d)} = \mu_0 c_1^{s(d)} c_2 \omega^{\eta} \exp[-i(\pi/2)\eta] \tag{3.62}$$

where we have

$$\eta = \frac{1+\alpha+\beta(1-\alpha)}{2+\alpha} \tag{3.63}$$

$$c_2 = \left(\frac{\lambda_L^2 v_F^{\alpha}\gamma^{(\beta-1)(\alpha-1)}}{a}\right)^{1/(2+\alpha)} \tag{3.64}$$

$$c_1^s = \frac{2}{\pi}\Gamma\left(\frac{\alpha+1}{\alpha+2}\right)\Gamma\left(\frac{\alpha+3}{\alpha+2}\right) \tag{3.65}$$

$$c_1^d = \pi\left[\Gamma\left(\frac{1}{\alpha+2}\right)\Gamma\left(\frac{\alpha+1}{\alpha+2}\right)\right]^{-1}. \tag{3.66}$$

In table 3.6 we examine how boundary conditions affect the magnitude of the asymptotic values of the surface impedance. We see that only for $\alpha = 1$ do the boundary conditions have an effect. The ratio we find between the two cases, 8/9, is exactly that originally found by Reuter and Sondheimer [51].

It is worth noting that the analysis herein is limited by the assumption that the conductivity is given by eq. (3.61), which considers only leading-order terms in the expansion of the conductivity. It turns out that in region 5 (cf. fig. 3.2), the surface impedance is strongly dependent on boundary conditions. In this region, we get $\eta = 1$ and the analysis above captures the dominant behaviour of the impedance, namely $Z \propto \omega e^{-i(\pi/2)}$. There is in fact, a finite real part of the impedance in which the sensitivity to boundary conditions is manifested, but this only appears by considering the second-order terms in the expansion of the conductivity.

α	c_1^s	c_1^d	c_1^s/c_1^d
0	1	1	1
1	$\frac{4}{3\sqrt{3}}$	$\frac{\sqrt{3}}{2}$	$\frac{8}{9}$
2	$\frac{1}{\sqrt{2}}$	$\frac{1}{\sqrt{2}}$	1

Table 3.6: Influence of boundary conditions on magnitude of surface impedance.

Circular geometry

In the plane defined by $\gamma_{mc} = \gamma_{mr}$, we see that the qualitative behaviour matches that for a spherical FS, as first presented by Casimir and Ubbink [15]. In the $\gamma_{mc} - \omega$ plane, we see the appearance of a viscous regime. As predicted by Gurzhi, the onset of this regime occurs for $l_G > \delta$ and the regime persists until $l_{mc} > \delta$. A previously unidentified boundary on this regime is defined by $\delta_\nu = \lambda_L$.

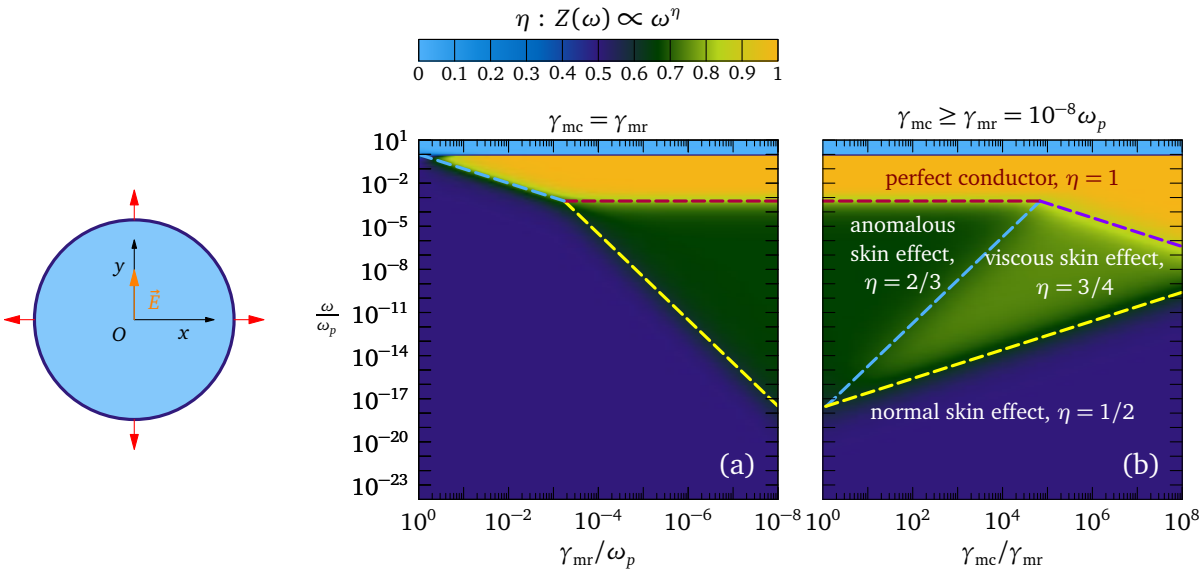

Figure 3.3: Surface impedance for circular geometry. $\vec{E} \parallel y$ and $\vec{q} \parallel x$. The two plots meet at their minimum horizontal values. From [69].

Square 0° and hexagonal 0° geometries

In these two geometries, for a large portion of the FS, the electrons are propagating perfectly parallel to the electric field $\boldsymbol{E}$ (and thus perfectly perpendicular to the wavevector $\boldsymbol{q}$).

In the case of the square 0° geometry (fig. 3.4, bottom), all states which contribute to the current are also perfectly parallel to the electric field. Therefore, there is no wavevector dependence whatsoever. The surface impedance is exactly that found for the Drude model, with no dependence on $\delta\gamma$. Both the ASE and the VSE are suppressed. Physically, both originate from the fact that electrons only propagate parallel to the sample's surface. Because they do not travel in and out of the skin layer, they cannot become ineffective, suppressing the ASE. Because there is no way to couple momentum between different layers parallel to the sample's surface, there can be no viscous effects, suppressing the VSE.

The case of the hexagonal 0° geometry (fig. 3.5, bottom) is similar to that of the square 0° geometry, though the deviations from the circular geometry are less extreme. In regions 3 and 4, this geometry also exhibits Drude-like behaviour. For $\delta\gamma = 0$, the only deviation from true Drude behaviour is that the apparent plasma frequency is reduced by a factor of 2/3. This can be understood by appeal to the ineffectiveness concept: deep in regions 3 and 4, the skin depth is much shorter than the MFP. The edges of the hexagonal FS with electrons propagating parallel to the sample's surface are exhibiting

Drude (local) behaviour, while the electrons from all other edges have become ineffective. For $\delta\gamma > 0$, the scattering rate that enters the Drude-like behaviour is $\gamma_{mr} + \delta\gamma/3$. Unlike the square geometry 0°, here the VSE is not suppressed. In region 6, with $l_G < \delta < l_{mc}$, the edges of the hexagonal Fermi surface with electrons not propagating parallel to the samples surface are effective in contributing to the coupling of transverse momentum, giving rise to viscous behaviour.

Square 45° and hexagonal 30° geometries

For both the square 45° geometry (fig. 3.4 top) and hexagonal 30° geometry (fig. 3.5 top), a surprising behaviour emerges: viscous behaviour is present in region 3, even for $\delta\gamma = 0$. This is interesting because it means that viscous behaviour does not have to originate from frequent MC scattering. In these geometries and in the absence of excess MC scattering, viscous behaviour arises as a result of the combination of (1) MR scattering, in which an electron's velocity is randomized, and (2) the symmetry of the discrete number of allowed velocity directions that the electron can randomly scatter into. In region 4, both geometries exhibit $\eta = 1/2$ behaviour, which is typically associated with the CSE. However, aside from the same η, all other aspects of the behaviour are different. The CSE occurs as a result of $\alpha = 0, \beta = 0$ whereas here $\alpha = 2, \beta = 1$. Therefore, the two have different dependences on λ_L, v_F, γ_{mr}, and $\delta\gamma$. The behaviour across regions 3 and 4 can be understood as viscous behaviour with a frequency dependent viscosity

$$\nu(\omega) = \frac{v_F^2}{\delta\gamma - i\omega} \tag{3.67}$$

which takes the limiting behaviours

$$\nu(\omega) = \begin{cases} \dfrac{v_F^2}{\delta\gamma} & \text{region 3} \\ \dfrac{v_F^2}{-i\omega} & \text{region 4.} \end{cases} \tag{3.68}$$

Viscosity tensor for hexagonal symmetry

It is interesting to note that the asymptotic conductivity and surface impedance in region 4 is identical for the two hexagonal geometries. This is not the case for the two square geometries. In fact, this is a consequence of the fact that systems with hexagonal symmetry have an isotropic viscosity tensor. Interestingly, this fact is exploited in computational fluid dynamics, where spatially-discretized fluid simulations are performed on hexagonally-symmetric lattices to ensure isotropy [23].

3.4 Outlook

In this chapter, we have derived the transverse, non-local conductivity for a metal of arbitrary FS and with separate rates of MR and MC scattering. We applied our result to a circular FS, and showed that we could capture both ASE and the VSE, unifying simpler models that captured only the former [51, 57] or the latter [22, 26]. We showed that polygonal Fermi surfaces lead to significant differences

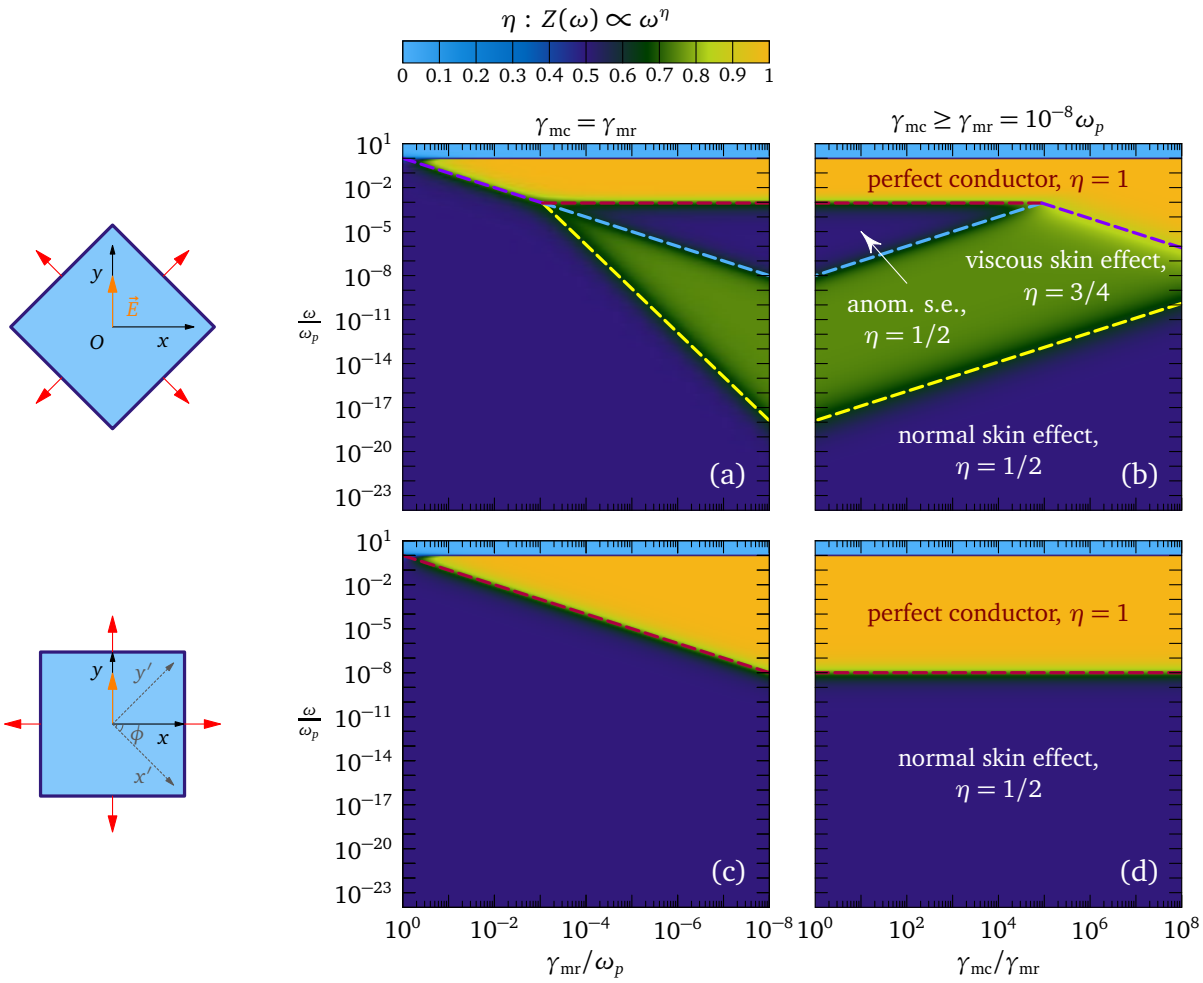

Figure 3.4: Surface impedance for square geometries. $\vec{E} \parallel y$ and $\vec{q} \parallel x$. The two plots meet at their minimum horizontal values. From [69].

in the phenomenology of non-local electrodynamics. For square or hexagonal FSs aligned such that a significant fraction of electrons propagate parallel to the sample's surface, there is a suppression of non-locality. For square and hexagonal FSs rotated by π/N (where N is the order of the polygon), we saw that viscous behaviour emerged even in the absence of frequent MC collisions. The square FS represents the most extreme possible deviation from a circular FS among materials with isotropic local conductivity tensors. The hexagonal FS represents an intermediate case, and also demonstrates the special property of lattices with six-fold rotational symmetry: namely, an isotropic viscosity tensor.

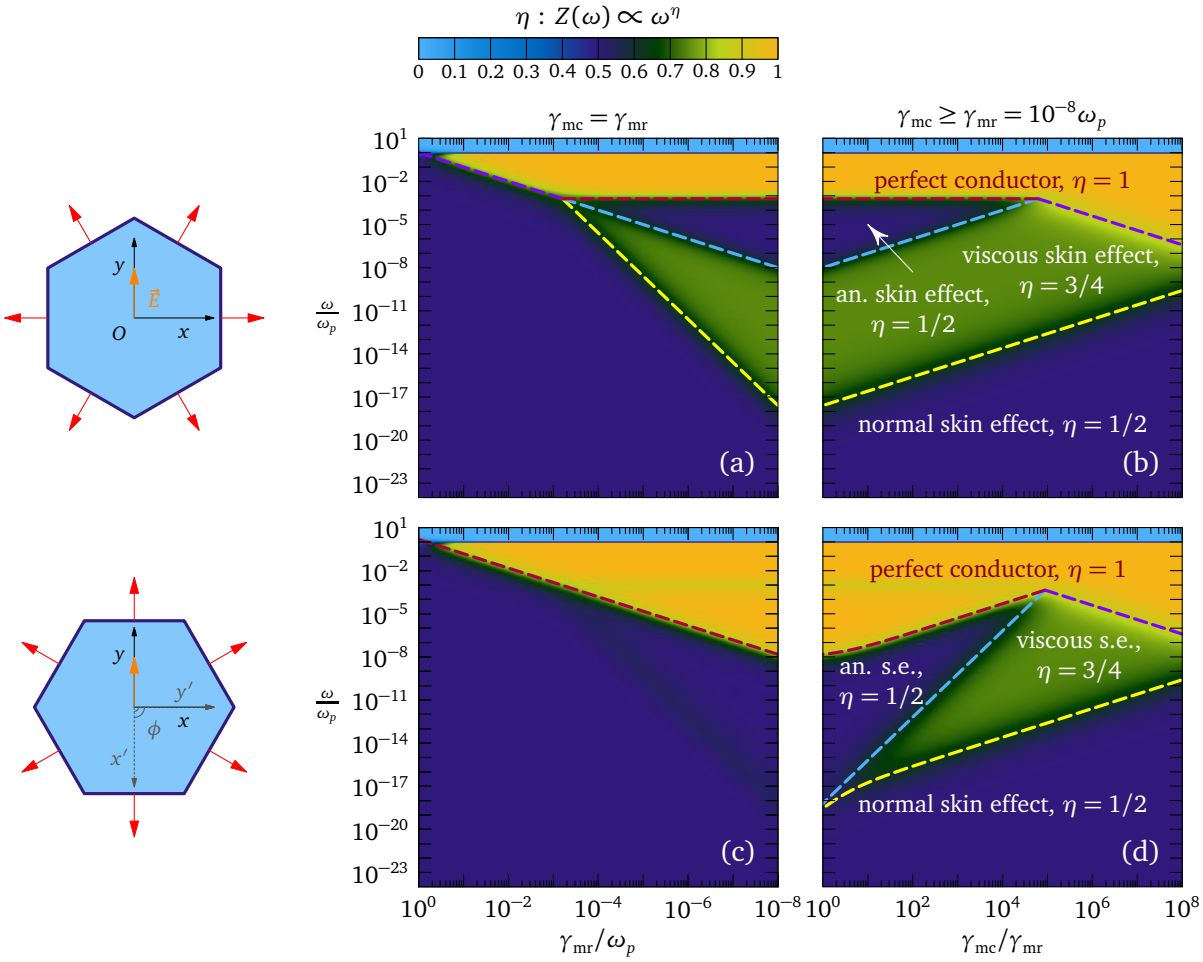

Figure 3.5: Surface impedance for hexagonal geometries. $\vec{E} \parallel y$ and $\vec{q} \parallel x$. The two plots meet at their minimum horizontal values. From [69].

Chapter 4

The skin effect in $PdCoO_2$

4.1 Overview

In this chapter, we describe microwave-frequency measurements of $PdCoO_2$. These measurements were aimed at differentiating between diffusive, ballistic, and viscous effects and at examining directional effects arising from Fermi surface anisotropy.

In section 4.2, we describe the microwave spectroscopy technique that was employed in these measurements. Spectroscopic techniques in this frequency range are scarce, and this particular technique is unique to our lab.

While many treatments of the electrodynamics of conducting media are based on solving Maxwell's equations at the planar interface to a semi-infinite medium, the electrodynamics of finite bodies are, in general, more complicated. While in many cases it is possible to use sample geometries which permit simplifying assumptions, this work necessitated using geometries which require going beyond these standard simplifying assumptions. This is the topic of section 4.3.

Finally, in section 4.4, we present and discuss our results.

4.2 Experimental technique

Here we describe the experimental technique used in this work. As in-depth descriptions are available elsewhere [12, 63, 64], here we focus only on the essential elements of its operation. The basis of the technique is that (1) a spatially-uniform magnetic field of variable microwave frequency is applied to a sample, and (2) the power absorbed by the sample is detected bolometrically. We will consider these two steps in sections 4.2.1 and 4.2.2.

4.2.1 Detection

Bolometric detection

We start with a review of the basic principle of bolometric detection [52, 64], as illustrated in fig. 4.1. A bolometer consists of an absorbing element, which converts incident electromagnetic radiation to

heat, in thermal contact with a resistive thermometer. The combination is attached to a heat sink at temperature T_0 via thermal conductance K. The absorbing element, thermometer, and thermal link have a heat capacity C. The resistive thermometer, with resistance R_B, is biased with a constant current I_B, which determines the bolometer temperature T_B according to

$$I_B^2 R_B(T_B) = K(T_B - T_0). \tag{4.1}$$

An incident radiant power P_S raises the bolometer temperature by an amount[1]

$$\delta T_B = \frac{P_S}{K} \tag{4.2}$$

with time constant $\tau = C/K$. The corresponding change in bolometer voltage is given by

$$\delta V_B = I_B \left(\frac{dR_B}{dT}\right)_{T_B} \delta T_B + \mathcal{O}(\delta {T_B}^2) \tag{4.3}$$

The responsivity of the bolometer for incident radiant power $P_S e^{-i\omega t}$ is

$$S \equiv \frac{\delta V_B}{P_S} = \left(\frac{dR_B}{dT}\right)_{T_B} \frac{I_B/K}{1 - i\omega\tau}, \tag{4.4}$$

exhibiting low-pass behaviour. A key simplifying assumption in the above is the treatment in terms of lumped thermal elements. Indeed, for our implementation of bolometric detection, a treatment in terms of distributed thermal elements has been shown to yield a better quantitative description of the responsivity [12]. However, the key qualitative features of the responsivity remain the same.

Sample stage

In our technique, the sample under test serves as the absorbing element. The sample and resistive thermometer are attached to a sapphire plate, as shown in fig. 4.2. Sapphire is used in part because its high thermal diffusivity ensures that it is isothermal on the time scale of bolometer operation. The sapphire plate is epoxied into the bore of a quartz tube. The quartz tube serves as a thermal link to the liquid helium bath, which acts as a heat sink.

A key requirement for using bolometric detection with the sample as the absorbing element is the ability to electromagnetically shield the thermometry. As will be described in section 4.2.2, microwave fields are delivered to the sample via a waveguide. The sample is inserted into the waveguide through a hole. The cutoff frequency for the propagation of electromagnetic modes through this hole is inversely proportional to its radius. This means that, at microwave frequencies, we can make a hole that is simultaneously large enough to allow mm-sized samples to pass while being small enough that the

[1] Here we are neglecting thermal feedback. The expected temperature rise $\delta T_B = P_S/K$ is modified by the fact that δT_B leads to a change in R_B, modifying the bias heating. This can be captured via an effective thermal conductance $K_e = K - I_B^2 (dR_B/dT)_{T_B}$. In practice, this effect should be captured by our calibration procedure, which is performed after I_B and T_B have already been set.

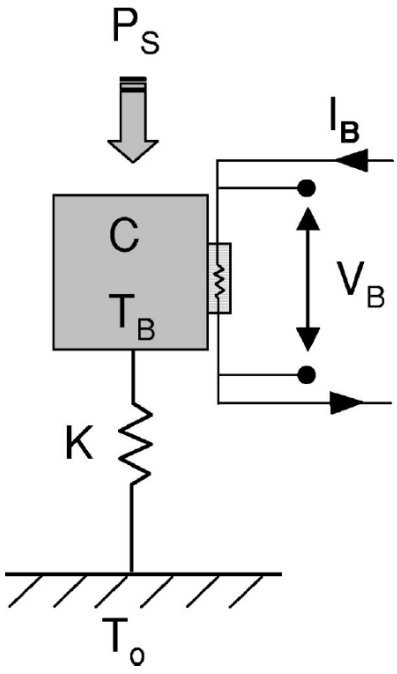

Figure 4.1: Principle of bolometric detection. Incident radiative power raises the temperature of the bolometer relative to that of that of a heat sink, as measured via a resistive thermometer. From [64].

cutoff frequency is greater than our maximum operating frequency. The same cannot be accomplished at infrared frequencies.

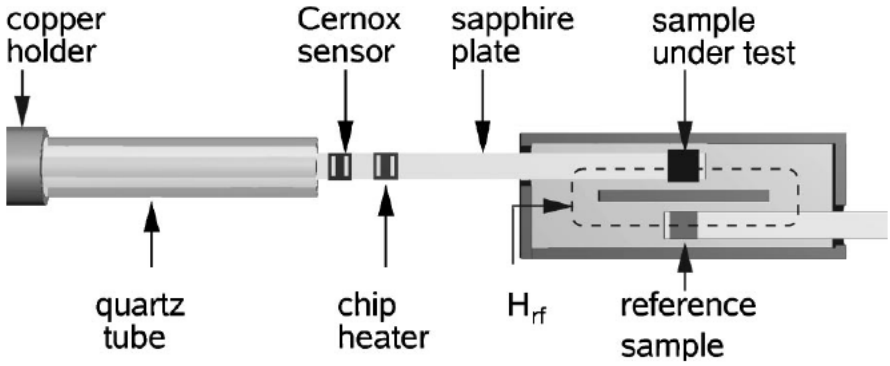

Figure 4.2: Sample stage of the bolometric microwave spectrometer and cross section of coaxial transmission line. The sample is mounted on an isothermal sapphire plate and inserted into the transmission line where it absorbs power from a spatially-uniform, microwave-frequency magnetic field. The resulting rise in temperature is measured via a resistive thermometer ("Cernox sensor"). The quartz tube provides a weak thermal link to a liquid helium bath. The heater provides an in-situ calibration of the bolometric responsivity. A reference sample, placed at an electromagnetically equivalent position, serves to calibrate the absolute magnetic field strength. From [64].

Signal processing

Microwave power is amplitude-modulated by a square wave and the resulting AC variation in thermometer voltage δV_B is measured. The thermometer voltage is band-pass filtered and amplified before being digitized. The component at the modulation frequency is then determined via a home-built software-defined lock-in detection system. The modulation frequency is typically $\sim$1 Hz and is set by the balance of two considerations: (1) the higher the modulation frequency, the lower the $1/f$ noise, and (2) the lower the modulation frequency, the greater the responsivity of the bolometric detection, which exhibits low-pass behaviour.

Calibration 1: Bolometric responsivity

To extract the power absorbed by the sample from the measured AC thermometer voltage δV, we must determine the bolometric responsivity. A heater is attached to the sapphire plate at a position external to the transmission line. After determining the resistance R_{htr} of the heater, we can apply a known power with amplitude $P_{\mathrm{htr}} = I_{\mathrm{htr}}^2 R_{\mathrm{htr}}$ to the heater, square wave-modulated at the intended modulation frequency of the microwave power. We then measure the responsivity to heater power as

$$S_{\mathrm{htr}} \equiv \frac{\delta V}{P_{\mathrm{htr}}} \tag{4.5}$$

We then assume that the responsivity to microwave power $S_{\mu\mathrm{w}}$ is equivalent to S_{htr}, and determine the power absorbed by the sample from the response to microwave power as

$$P = S_{\mathrm{htr}} \delta V. \tag{4.6}$$

$S_{\mu\mathrm{w}}$ and S_{htr} may differ due to the finite thermal diffusivity of the sapphire plate or the thermal dynamics of the connection between the sample and the sapphire plate (which is made via vacuum grease). However, assuming a good connection between sample and sapphire plate, these differences in responsivity occur at modulation frequencies higher than the corner frequency set by the thermal behaviour intrinsic to the sample holder, which sets the maximum practical modulation frequency anyway. In fact, a poor thermal connection between sample and sapphire plate may be identified via a lag in the thermometer response for applied microwave power as compared to that for applied heater power.

4.2.2 Microwave circuitry

Waveguide

We want to expose the sample under study to a spatially-uniform magnetic field of known polarization. To do so we use a rectangular transmission line. By using a broad septum, acting as the centre conductor of the transmission line, we create large regions of uniform magnetic field in the transverse electromagnetic (TEM) mode. To create an electric field node, we short circuit the transmission line with a metallic end wall and insert the sample into the transmission line as close to this end wall as possible. While the

TEM mode propagates at all frequencies, transverse electric (TE) and transverse magnetic (TM) modes propagate above their respective cutoff frequencies. The upper frequency limit of the apparatus is set by the lowest frequency at which one of the TE or TM modes forms a resonant standing wave. This occurence is problematic because it leads to asymmetry in the transmission line, causing a breakdown of the calibration described in section 4.2.2.

Calibration 2: Absolute magnetic field strength

Standing waves in the microwave circuitry result in a microwave power delivered to the sample that is strongly frequency-dependent. Key to the success of this experimental technique is an in-situ reference sample placed at an electromagnetically equivalent position—the mirror position with respect to the septum (see fig. 4.2). We use an AgAu alloy with 70:30% atomic composition. By virtue of being an alloy, we can expect its surface resistance to be isotropic and to exhibit the CSE over the entirety of our frequency range. Its surface resistance is then entirely determined by its known resistivity. This sample is used to calibrate the strength of the applied magnetic field H_0, controlling for the frequency-dependent effect of standing waves as shown in fig. 4.3.

4.2.3 Comparison with other techniques

Here we briefly compare bolometric microwave spectroscopy (BMS) to alternative microwave-frequency techniques.

Cavity perturbation

The microwave cavity perturbation (MCP) technique has historically been the primary technique for microwave measurements. In this technique, the power transmitted or reflected by a resonant microwave cavity is measured with and without a sample present. The sample acts to perturb the resonance. The change in resonance width is related to the sample's surface resistance R, and the shift in the resonance frequency is related to the sample's surface reactance X.

An advantage of MCP over BMS is that the full complex impedance $Z = R + iX$ is measured by MCP whereas only R is measured by BMS. In the limit of local electrodynamics, knowledge of both R and X is sufficient to directly determine the full complex conductivity $\sigma = \sigma_1 + i\sigma_2$, whereas knowledge of R alone is insufficient. There are, however, methods of indirectly determining the complex conductivity from R alone, e.g. via Kramers-Kronig relations, though these always rely on certain assumptions.

Another advantage of MCP is that it retains sensitivity up to room temperature, whereas the sensitivity of BMS is limited to low temperatures. This is because the resolution of MCP is set by the resonance width of the empty cavity, which depends on the cavity's temperature. Using a sapphire hot finger, the sample's temperature can be raised while keeping the cavity at base temperature.

An obvious disadvantage of MCP is that it is restricted to a small number of discrete resonance frequencies.

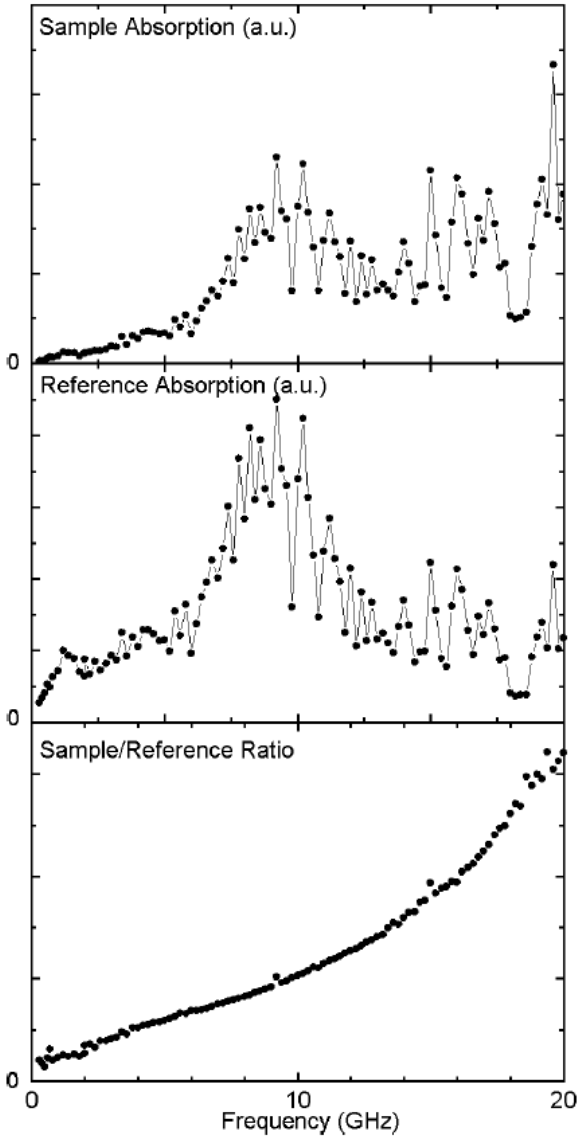

Figure 4.3: Calibration of microwave field strength in the bolometric microwave spectrometer. In the raw sample and reference signals, the intrinsic frequency dependence is hidden by a strongly frequency-dependent magnetic field strength as a result of standing waves in the microwave circuitry. Taking the ratio of the two signals eliminates the dependence on magnetic field strength, revealing a clear trend coming from the frequency dependent surface resistance of the two samples. From [64].

Corbino spectroscopy

Corbino microwave spectroscopy (CMS) is another spectroscopic technique in the GHz range. In this technique, a sample short circuits the end of a coaxial transmission line. The complex reflection coefficient S_{11} is measured using a vector network analyzer. A key advantage of CMS over BMS is that it measures a complex quantity.

A disadvantage of CMS is that its sensitivity depends on impedance matching between the coaxial line (which has a characteristic impedance of $50\,\Omega$) and the sample. This limitation is particularly severe in the present context of measuring highly conductive materials in which the surface impedance at microwave frequencies is typically $\sim 1\,\mathrm{m}\Omega$.

Another disadvantage of CMS is the lack of flexibility in terms of geometry. As is evident from the previous chapter, in the non-local regime, one must consider the wavevector direction being probed, on top of the usual consideration of current direction. In $PdCoO_2$, it is of interest to take measurements with wavevectors within the highly-conductive *ab* planes, which necessitates applying fields to the thin edges of platelet samples. This would not be possible with CMS.

4.3 Sample geometry & electromagnetic induction

In chapter 3, we were interested in how FS geometry and ballistic and viscous effects were manifested in the optical conductivity and in the surface impedance, as defined for a semi-infinite sample. At infrared frequencies and above, a ray optics paradigm is valid and one may consider the incidence of electromagnetic radiation at a single sample surface. The relevant observables then include reflectance and transmittance. However, one can deduce that the regimes of interest in $PdCoO_2$ occur at microwave frequencies. Here, the free-space electromagnetic wavelength $\lambda_0 = c/f$ is much greater than the sample dimensions. To make contact between the quantities discussed in chapter 3 and those that are actually measured at these frequencies, one must consider the application of Maxwell's equations to finite bodies.

4.3.1 General considerations

Because we are interested in highly-conducting materials, we may consider the regime of quasi-magnetostatics (see fig. 4.4) and make the corresponding simplifications to Maxwell's equations. Charge relaxation occurs on a time scale much shorter than those of interest, so we may set $\rho_f = 0$. Furthermore, we may neglect the displacement current, as the dominant dynamical phenomenon in this regime is electromagnetic induction. We are left with the quasi-magnetostatic Maxwell's equations:

$$\nabla \cdot \boldsymbol{E} = 0 \tag{4.7}$$

$$\nabla \cdot \boldsymbol{H} = 0 \tag{4.8}$$

$$\nabla \times \boldsymbol{E} = i\mu_0 \omega \boldsymbol{H} \tag{4.9}$$

$$\nabla \times \boldsymbol{H} = \sigma \boldsymbol{E}. \tag{4.10}$$

These can be combined to yield a diffusion equation for $\boldsymbol{E}$ and $\boldsymbol{H}$:

$$\left(\nabla^2 + k^2\right) \begin{Bmatrix} \boldsymbol{E} \\ \boldsymbol{H} \end{Bmatrix} = 0 \tag{4.11}$$

where

$$k = \sqrt{i\mu_0 \omega \sigma} = \frac{1+i}{\delta}. \tag{4.12}$$

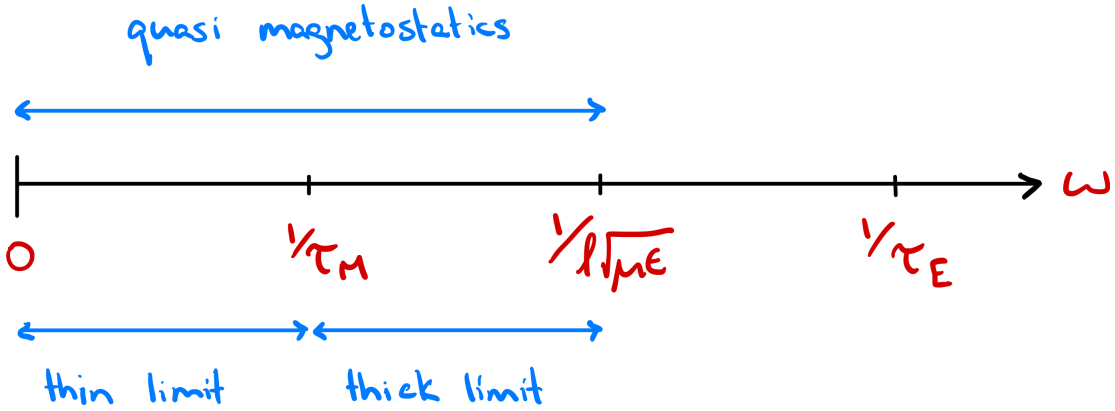

Figure 4.4: Electromagnetic regimes for a good conductor. The equations of quasimagnetostatics (eqs. (4.7) to (4.10)) apply when $\omega \ll 1/\tau_E$ where $\tau_E \equiv \varepsilon/\sigma$ and $\omega \ll 1/l\sqrt{\mu\varepsilon}$ where l is a characteristic physical dimension of the conductor. Taking $\mu = \mu_0$, $\varepsilon = \varepsilon_0$, and $l = 1\,\text{mm}$ leads to an upper limit of 300 GHz. The boundary between the thin and thick limits is given by $\omega \approx 1/\tau_M$ with $\tau_M \equiv \mu\sigma l^2$, or equivalently $l \approx \delta$. Adapted from [72].

We now wish to analyze general aspects of the qualitative behaviour of a good conductor in an external magnetic field H_0. We consider a medium with conductivity σ, $\varepsilon = \varepsilon_0$ and $\mu = \mu_0$. We will focus on two properties: the net magnetization

$$\bar{\boldsymbol{M}} \equiv \frac{\boldsymbol{m}}{V} = \frac{\sigma}{2V} \int d^3 r\, \boldsymbol{r} \times \boldsymbol{E} \tag{4.13}$$

and power dissipation

$$P = \frac{\sigma}{2} \int d^3 r\, |\boldsymbol{E}|^2. \tag{4.14}$$

One may distinguish between two regimes based on the size of the skin depth δ relative to the sample's dimensions. Using l to represent a characteristic sample dimension, the "thin" limit corresponds to $l \ll \delta$ while the "thick" limit corresponds to $\delta \ll l$. In these two cases, we may use the estimates

$$\nabla \sim \begin{cases} 1/l & l \ll \delta \\ 1/\delta & \delta \ll l. \end{cases} \tag{4.15}$$

We may then use eqs. (4.9), (4.10) and (4.15) to estimate the behaviour of the induced fields of $\boldsymbol{E}_{\text{ind}}$ and $\boldsymbol{H}_{\text{ind}}$ in terms of the series expansions. The first order term for E comes from substituting $H = H_0$ in eq. (4.9):

$$E_{\text{ind}}^{(1)} \sim \begin{cases} i\mu_0 \omega l H_0 & l \ll \delta \\ i\mu_0 \omega \delta H_0 & \delta \ll l. \end{cases} \tag{4.16}$$

We then substitute $E_{\text{ind}}^{(1)}$ into eq. (4.10) to find $H_{\text{ind}}^{(1)}$:

$$H_{\text{ind}}^{(1)} \sim \begin{cases} il^2/\delta^2 H_0 & l \ll \delta \\ iH_0 & \delta \ll l. \end{cases} \tag{4.17}$$

Continuing the procedure to find the second-order term for E_{ind}, we get:

$$E_{\text{ind}}^{(2)} \sim \begin{cases} \mu_0 \omega l^3/\delta^2 H_0 & l \ll \delta \\ \mu_0 \omega \delta H_0 & \delta \ll l. \end{cases} \tag{4.18}$$

Finally, we may use the estimate

$$\int d^3 r \sim \begin{cases} l^3 & l \ll \delta \\ l^2 \delta & \delta \ll l \end{cases} \tag{4.19}$$

which is motivated by the fact that for $l \ll \delta$, current flows through the entire volume of the conducting body, whereas for $\delta \ll l$, the skin effect means that current only flows in a small volume of depth δ within the surface.

We arrive at the results

$$\text{Re}(\bar{M}) \sim \begin{cases} \mu_0^2 \omega^2 \sigma^2 l^4 H_0 & l \ll \delta \\ H_0 & \delta \ll l \end{cases} \tag{4.20}$$

$$\text{Im}(\bar{M}) \sim \begin{cases} \mu_0 \omega \sigma l^2 & l \ll \delta \\ 1/\sqrt{\mu_0 \omega \sigma} & \delta \ll l \end{cases} \tag{4.21}$$

$$P \sim \begin{cases} \mu_0^2 \omega^2 \sigma l^5 H_0^2 & l \ll \delta \\ \sqrt{\mu_0 \omega/\sigma} l^2 H_0^2 & \delta \ll l. \end{cases} \tag{4.22}$$

We emphasize that we have arrived at these results independently of any assumptions about sample geometry. They will be relied upon heavily in sections 4.3.2 and 4.3.3.

Example: conducting sphere

Here we consider the specific example of a conducting sphere, for which the solution is known for arbitrary l/δ, and is shown in fig. 4.5.

Magnetization is given by [10]

$$\frac{\bar{M}}{H_0} = \frac{3}{2}\frac{j_2(ka)}{j_0(ka)} \tag{4.23}$$

where $j_n(\xi)$ are spherical Bessel functions of the first kind, a is the radius. This has the asymptotic behaviour

$$-\mathrm{Re}\left(\frac{\bar{M}}{H_0}\right) = \begin{cases} \dfrac{(\mu_0\omega\sigma)^2 a^4}{105} & a \ll \delta \\ \dfrac{3}{2} & \delta \ll a \end{cases} \tag{4.24}$$

and

$$\mathrm{Im}\left(\frac{\bar{M}}{H_0}\right) = \begin{cases} \dfrac{\mu_0\omega\sigma\, a^2}{10} & a \ll \delta \\ \dfrac{9}{2\sqrt{2}a\sqrt{\mu_0\omega\sigma}} & \delta \ll a. \end{cases} \tag{4.25}$$

We see that eqs. (4.24) and (4.25) match the form deduced via general arguments in eqs. (4.20) and (4.21). We see in particular that

$$\lim_{\delta/a\to 0}\frac{\bar{M}}{H_0} = -\frac{3}{2}. \tag{4.26}$$

This is exactly the well-known result one obtains at $\omega = 0$ for a perfectly diamagnetic sphere ($\mu = 0$).

Power is given by [10]

$$\frac{P}{H_0^2} = \pi a^3 \mu_0 \omega\, \mathrm{Im}\left[\frac{j_2(ka)}{j_0(ka)}\right] \tag{4.27}$$

and has the asymptotic behaviour

$$\frac{P}{H_0^2} = \begin{cases} \dfrac{\pi\mu_0^2\omega^2\sigma a^5}{15} & a \ll \delta \\ \dfrac{3\pi}{\sqrt{2}}\sqrt{\dfrac{\mu_0\omega}{\sigma}}a^2 & \delta \ll a. \end{cases} \tag{4.28}$$

We see that eq. (4.28) matches the form deduced via general arguments in eq. (4.22).

4.3.2 Magnetization

Here we consider magnetization, for which the treatment of finite bodies is better developed. For a linear magnetic medium, a body's magnetization $M(\boldsymbol{r})$ is related to the internal field $H(\boldsymbol{r})$ via the susceptibility χ:

$$M(\boldsymbol{r}) = \chi H(\boldsymbol{r}). \tag{4.29}$$

Ellipsoids

In ellipsoids, $H(\boldsymbol{r})$ is related to the applied magnetic field $H_0(\boldsymbol{r})$ via a demagnetizing factor N via

$$H(\boldsymbol{r}) = H_0(\boldsymbol{r}) - NM(\boldsymbol{r}) \tag{4.30}$$

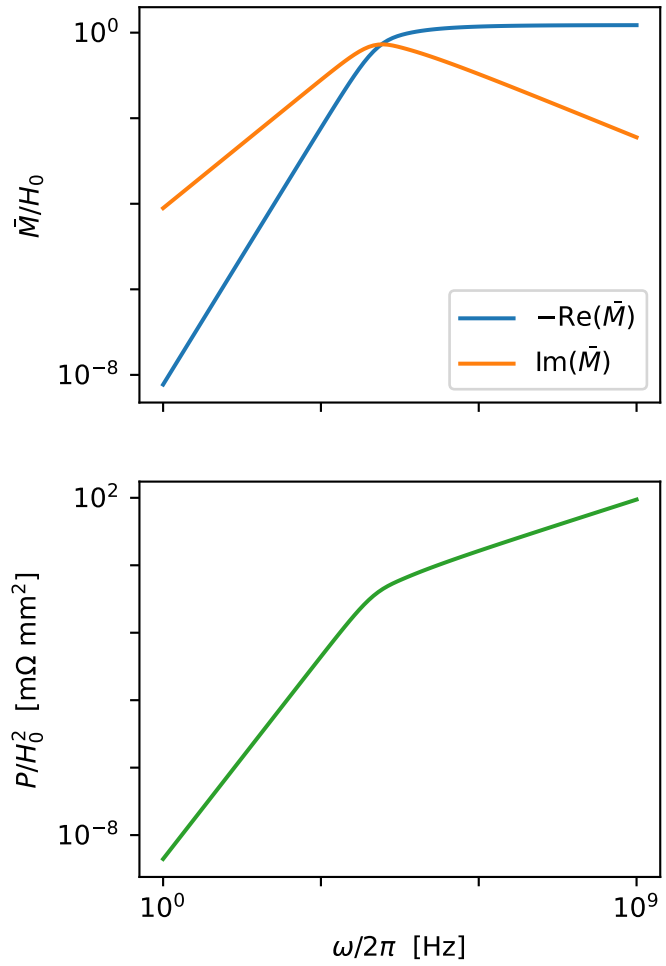

Figure 4.5: Magnetization and power dissipation for a conducting sphere with a radius of 1 mm, $\varepsilon = \varepsilon_0$, $\mu = \mu_0$ and $\sigma = 1\,\mu\Omega\,\mathrm{cm}$. Two limiting behaviours occur according to how the skin depth δ compares to the radius a: in the low-frequency limit, $a \ll \delta$; in the high-frequency limit, $\delta \ll a$.

so that

$$M(\boldsymbol{r}) = \frac{\chi}{1+\chi N} H_0(\boldsymbol{r}). \tag{4.31}$$

For an ellipsoid with dimensions a, b, and c and taking c to be the dimension parallel to $\boldsymbol{H}_0$, the demagnetizing factor is given by [50]

$$N = \frac{abc}{2} \int_0^\infty ds \, \frac{1}{(s+c^2)\sqrt{(s+a^2)(s+b^2)(s+c^2)}}. \tag{4.32}$$

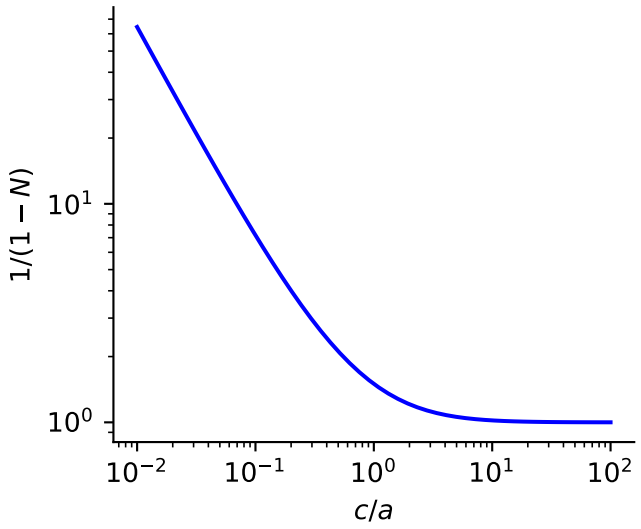

Figure 4.6: Demagnetizing factor of a spheroid as a function of aspect ratio. The magnetic field is applied along c. N is the demagnetizing factor and $1/(1-N)$ is the factor that relates the magnitudes of the effective magnetization and applied magnetic field.

Arbitrary shapes

For arbitrary shapes, a relationship between $H(\boldsymbol{r})$ and $H_0(\boldsymbol{r})$ as in eq. (4.30) does not exist in general. However, one may introduce an equation analogous to eq. (4.31) for effective, integral quantities. Assuming a constant external field, we have

$$\bar{M} = \bar{\chi} H_0 \tag{4.33}$$

with

$$\bar{\chi} = \frac{\chi}{1+\chi N} \tag{4.34}$$

where the effective magnetization $\bar{\boldsymbol{M}}$ is defined in terms of the total magnetic moment $\boldsymbol{m}$ as

$$\bar{\boldsymbol{M}} \equiv \frac{\boldsymbol{m}}{V} \tag{4.35}$$

and where N is now an effective demagnetizing factor. For a given sample geometry and susceptibility χ, if the magnetic moment $\boldsymbol{m}$ can be computed, then N can be found as

$$N = \frac{1}{\bar{\chi}} - \frac{1}{\chi}. \tag{4.36}$$

While for an ellipsoid, N is only a function of sample geometry, for an arbitrary shape, N is, in general, also a function of χ.

For a strongly diamagnetic sample, an established approximation scheme is the following: (1) Find N for the geometry of interest for a perfect diamagnet ($\chi = -1$), which is a function of only geometry;

(2) Use this N to infer the intrinsic susceptibility χ from measurements of M using eq. (4.34) [50].

4.3.3 Power absorption

Surface impedance boundary condition

The surface impedance boundary condition (SIBC) is a boundary condition for the tangential $\boldsymbol{E}$ and $\boldsymbol{H}$ fields at the surface of a good conductor:

$$\boldsymbol{E}_t = Z_s \boldsymbol{H}_t \times \hat{n} \tag{4.37}$$

where $\hat{n}$ is a unit normal pointing into the material. Certain conditions must be met for this condition to be valid [54]:

1. The requirements of the quasi-magnetostatic regime must be met.
2. The minimum radius of curvature and minimum thickness of the conductor must be large compared to the skin depth.
3. The variation of the electromagnetic fields in directions along the surface must be small compared to the variation in the normal direction.

In our work, we measured cylindrical samples of hexagonal cross-section which consist of piecewise flat surfaces. The only place in which the above assumptions are not met is at the edges joining flat surfaces, at which the radius of curvature goes to zero. In practice, it has been found that the details of sharp edges matter for non-linear but not for linear properties [11].

Definition of power factor

Time-averaged electromagnetic power dissipated in a sample is given by

$$P = \int \bar{\boldsymbol{S}} \cdot d\boldsymbol{A} = \frac{1}{2}\mathrm{Re}\left[\int dA\, E_t \times H_t^*\right] \tag{4.38}$$

where $\bar{\boldsymbol{S}}$ is the time-averaged Poynting vector. Assuming the surface impedance approximation, we have

$$P = \frac{1}{2} R^{\mathrm{eff}} \int dS\, K^2 \tag{4.39}$$

where R^{eff} is the effective surface resistance and K is the magnitude of the effective surface current

$$\boldsymbol{K} = \hat{\boldsymbol{n}} \times \boldsymbol{H} \tag{4.40}$$

where $\hat{\boldsymbol{n}}$ is the outward pointing normal vector of the sample's surface and $\boldsymbol{H}$ is the magnetic field at the surface. We consider the case of an applied field $\boldsymbol{H}_0$ along the z direction:

$$\boldsymbol{H}_0 = H_0 \hat{\boldsymbol{z}}. \tag{4.41}$$

We define a "power factor" α as

$$\alpha \equiv \frac{1}{SH_0^2}\int dS\,K^2 \tag{4.42}$$

where

$$S = \int dS \tag{4.43}$$

such that power absorption can be written as

$$P = \frac{1}{2}\alpha R^{\text{eff}} S H_0^2. \tag{4.44}$$

For a conductor with $\delta \ll l$, to lowest order, α is independent of conductivity and equivalent to that for a perfect conductor of the same shape [34], as can be deduced from eq. (4.22). Therefore, to relate our power absorption measurements to a surface resistance, we performed simulations of perfectly conducting samples of the relevant shapes to find their power factors.

Power factor of of an ellipsoid

Here we derive the power factor of an ellipsoid. We consider this case because the ellipsoid is the lowest-symmetry geometry for which the internal induced magnetic field is uniform, a fact which enables an analytic solution. To our knowledge, this is an original result. We have

$$\boldsymbol{H} = H\hat{\boldsymbol{z}}. \tag{4.45}$$

Using that

$$H = \frac{1}{1+\chi N}H_0 \tag{4.46}$$

we may further write

$$\alpha = \frac{\beta}{(1+\chi N)^2} \tag{4.47}$$

so that

$$\beta = \frac{1}{SH^2}\int dS\,K^2. \tag{4.48}$$

For a general ellipsoid, we find that

$$\beta = \frac{1}{S}\int_0^{2\pi} d\phi \int_0^{\pi} d\theta\, \frac{c^2 \sin^4\theta\,(b^2\cos^2\phi + a^2\sin^2\phi)}{\sin\theta\sqrt{c^2\sin^2\theta\,(b^2\cos^2\phi + a^2\sin^2\phi) + a^2b^2\cos^2\theta}} \tag{4.49}$$

with

$$S = \int_0^{2\pi} d\phi \int_0^{\pi} d\theta\, \sin\theta\sqrt{c^2\sin^2\theta\,(b^2\cos^2\phi + a^2\sin^2\phi) + a^2b^2\cos^2\theta}. \tag{4.50}$$

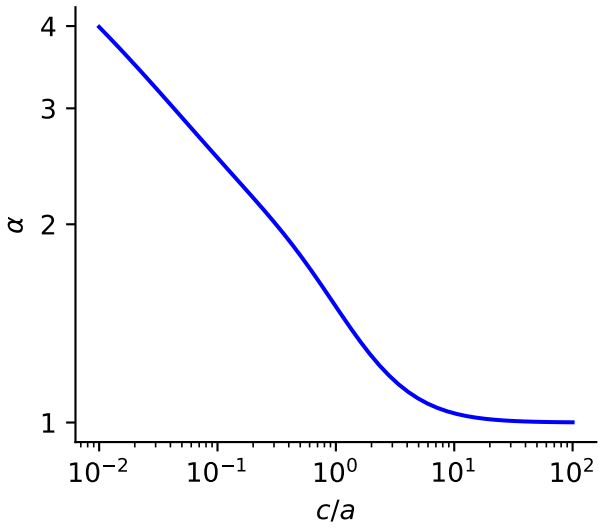

Figure 4.7: Power factor of a spheroid as a function of aspect ratio. The magnetic field is applied along c. We have defined the power factor so that it quantifies the geometric enhancement of power absorption per unit area relative to that for a semi-infinite medium.

4.4 Results

The FS of $PdCoO_2$ (fig. 4.8b) immediately suggests three extremal wavevector directions for which to perform measurements: $\boldsymbol{q} \| < 110 >$ ("0"), $\boldsymbol{q} \| < 100 >$ ("30"), and $\boldsymbol{q} \| < 001 >$ ("c"). Samples of $PdCoO_2$ grow as platelets with in-plane dimensions aroumd 1 mm and typical thicknesses of 10s of μm. To reflect the underlying symmetry of the crystal structure, we cut samples to have hexagonal cross section, with lateral dimensions of about 0.5 mm. We applied a spatially-uniform, microwave-frequency magnetic field parallel to the c axis, inducing eddy currents which flow in loops perpendicular to the magnetic field. This establishes two skin regions: near the edges of the two large hexagonal faces, with wavevector along the c axis, and on the six small rectangular faces, with wavevector perpendicular to the c axis (fig. 4.8c).

By measuring three different sample geometries—two orientations relative to the crystal structure and two thicknesses—we obtained the necessary data to determine the three components we sought.

Platelet samples were cut into hexagons using a high-precision wire saw with a 50 μm tungsten wire and 50 nm Al_2O_3 abrasive suspended in glycerin. The orientation of the crystals was determined via their growth edges, which are oriented perpendicular to the crystallographic axes. A goniometer mounted to the wire saw was used to rotate the samples in between cuts. Samples 1 and 2 were cut from the same original crystal. For Sample 3, a smaller thickness was desired and so it was cut from a separate original crystal from the same batch. The sample dimensions listed in table 4.1 were determined via optical microscopy.

To quantitatively interpret our measurements, it was necessary to account for the extrinsic geometric effects which lead to a difference between the externally applied, spatially-uniform magnetic field $\boldsymbol{H}_0$ and the magnetic field $\boldsymbol{H}(\boldsymbol{r})$ at the sample's surface. To do so, we relied on power factors, as introduced

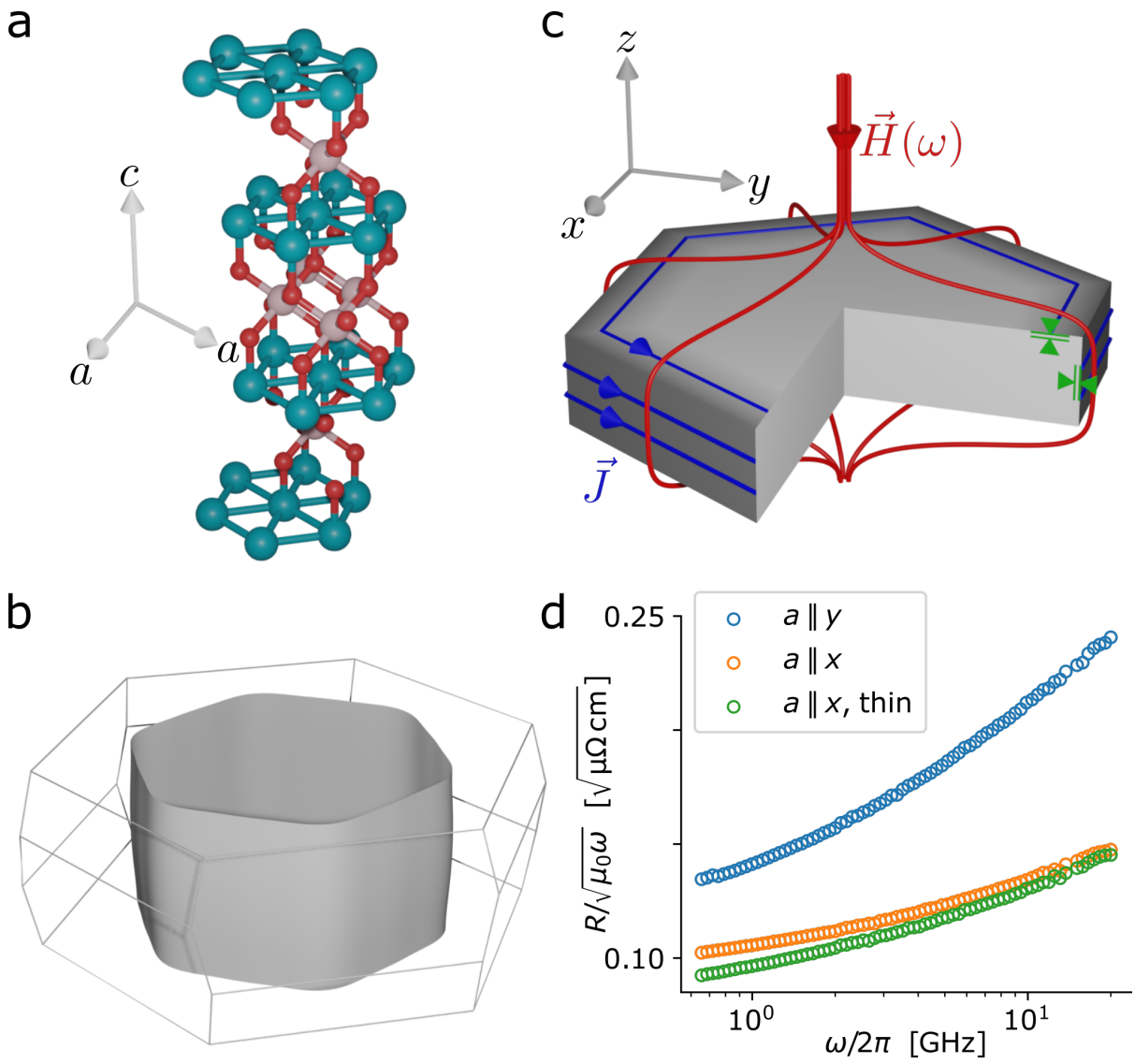

Figure 4.8: Microwave spectroscopy measurements of $PdCoO_2$. (a) $PdCoO_2$ crystal structure, belonging to the trigonal crystal system. (b) $PdCoO_2$'s hexagonally faceted Fermi surface, as determined via ARPES and quantum oscillations. (c) Measurement geometry. Samples, which grow naturally as thin platelets, were cut into hexagons to reflect the 6-fold rotational symmetry of the crystal structure. A microwave-frequency magnetic field is applied along z. This induces eddy currents (blue) acting to screen the magnetic field (red) from the interior of the sample. The resulting field strength at the sample's surface (grey shading) is highest on the side faces but also becomes appreciable toward the edges of the top and bottom faces. Because the skin depth is much smaller than the sample dimensions, this gives rise to two separate "skin regions" (indicated by green arrows). In both, current flows in the (001) plane and the wavevector is perpendicular to the surface. The measured signal contains a mixture of the two skin regions that depends on the sample's aspect ratio. (d) Raw data. We measured three samples, with two different cut orientations and two different aspect ratios. When the sample is cut with $a \parallel x$, $\boldsymbol{q} \parallel \langle 110 \rangle$ ("30") on the side faces; when the sample is cut with $a \parallel y$, $\boldsymbol{q} \parallel \langle 100 \rangle$ ("0") on the side faces. Varying the aspect ratio enables isolating the contribution from the top and bottom faces, where $\boldsymbol{q} \parallel c$. All three measurements differ—by symmetry, this can only occur for non-local electrodynamics. From [6].

Sample	Hexagonal face area [mm^2]	Hexagonal face perimeter [mm]	Thickness [μm]	Cut orientation
1	0.187	1.72	88	$a \parallel x$
2	0.169	1.62	79	$a \parallel y$
3	0.191	1.76	49	$a \parallel y$

Table 4.1: Sample information. The cut orientations refer to the directions defined in fig. 4.8.

in section 4.3.3. This relies on the assumption that the skin depth is much less than the sample dimensions. To verify this assumption, in fig. 4.9 we estimated the skin depth across our measurement range using the classical expression. Comparison to table 4.1 shows that this assumption is indeed valid.

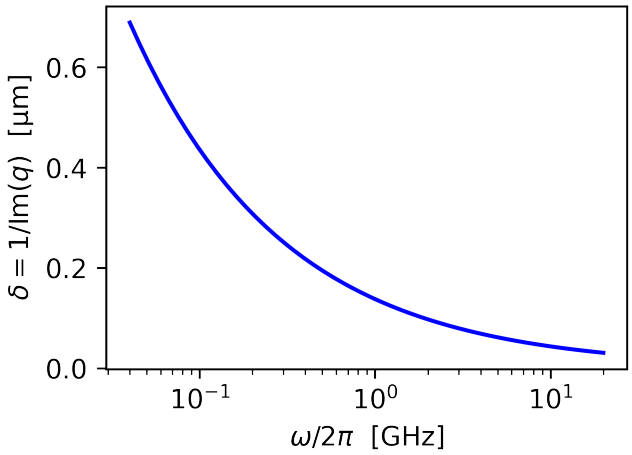

Figure 4.9: Classical skin depth of $PdCoO_2$ across the range of measured frequencies. From [6].

We studied the power factor α as a function of sample aspect ratio c/a for several different shapes, as shown in fig. 4.10. For spheroids, it was possible to treat the problem analytically. For cylinders and hexagonal prisms, finite-element simulations were performed [14]. Because the axial symmetry of cylinders allows for faster convergence of simulation results, this shape was studied over a wide range of aspect ratios. Since the simulation of hexagonal prisms was more resource-intensive, we only focused on directly relevant aspect ratios. Within the range of aspect ratios relevant to the samples studied here, all three shapes yielded similar results.

Because $\delta \ll \{c,a\}$, R^{eff} can be viewed as a sum of two independent components: $R_\perp$ comes from the faces perpendicular to $\boldsymbol{H}_0$ (the two large hexagonal faces) and $R_\parallel$ comes from the faces parallel to $\boldsymbol{H}_0$ (the six small rectangular faces). The relative contribution of the two components is set by a weight $w_\perp$:

$$R^{\text{eff}} = w_\perp R_\perp + (1 - w_\perp) R_\parallel \tag{4.51}$$

The weight $w_\perp$ can be found via the variation of the tangential magnetic field strength over the surface

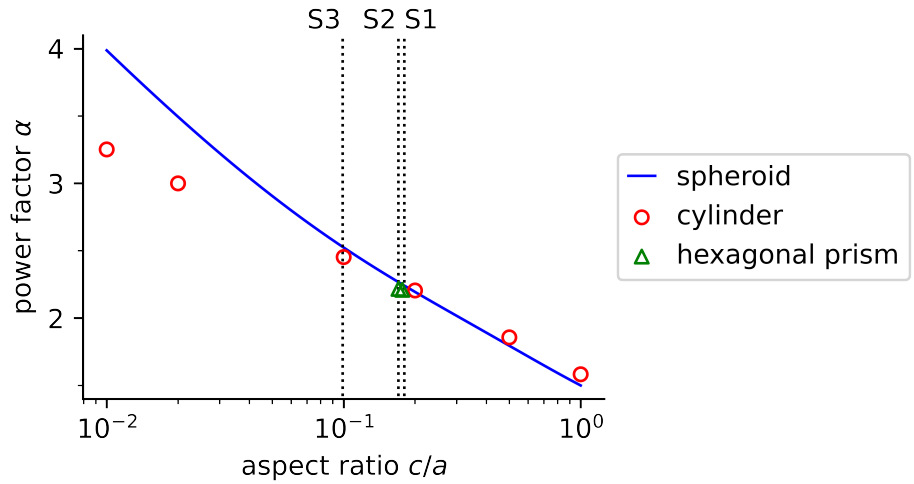

Figure 4.10: Effect of sample geometry on overall power absorption. Power factor α versus aspect ratio c/a for several sample geometries. Vertical lines represent the aspect ratios of the measured samples. From [6].

of a perfect conductor of the same shape:

$$w_{\perp} = \int_{A_{\perp}} H_t^2 dA \Big/ \int_{A_{\perp}+A_{\parallel}} H_t^2 dA \tag{4.52}$$

where $A_{\perp}$ ($A_{\parallel}$) is the area of the perpendicular (parallel) faces. The weights determined by our finite-element simulations are shown in fig. 4.11.

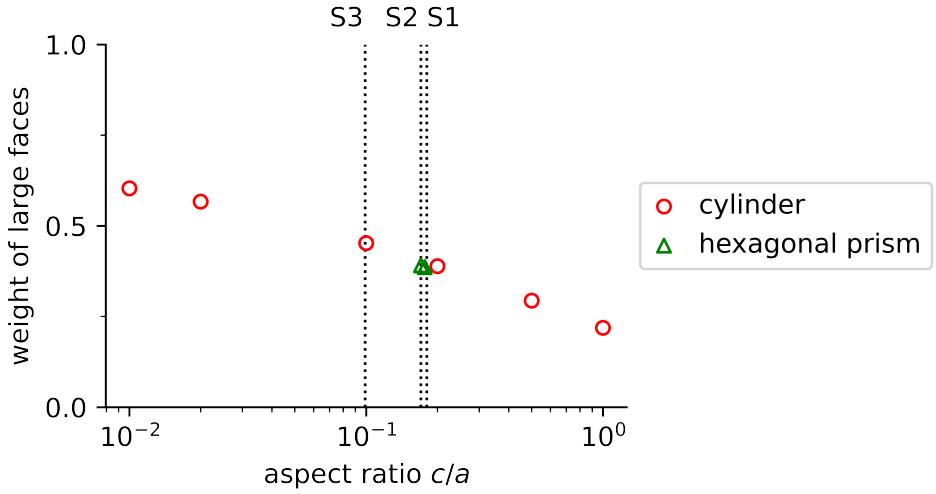

Figure 4.11: Effect of sample geometry on relative contribution of faces. Weight $w_{\perp}$ of large faces (perpendicular to applied magnetic field) as a function of aspect ratio c/a. From [6].

Applying eq. (4.51) to the three samples that we measured, we get

$$R_1 = w_1 R_{a,c} + (1 - w_1) R_{30,0} \tag{4.53}$$

$$R_2 = w_2 R_{a,c} + (1 - w_2) R_{0,30} \tag{4.54}$$

$$R_3 = w_3 R_{a,c} + (1 - w_3) R_{0,30} \tag{4.55}$$

where on the left side of the equations, R_i refers to R^{eff} for Sample i, and on the right side of the equations, the two subscripts refer to the directions $\hat{\boldsymbol{J}}, \hat{\boldsymbol{q}}$. Using eqs. (4.54) and (4.55), $R_{a,c}$ was found from the measurements of Samples 2 and 3:

$$R_{a,c} = \frac{w_3 R_2 - w_2 R_3}{w_3 - w_2}. \tag{4.56}$$

$R_{a,c}$ was then used to determine $R_{30,0}$ and $R_{0,30}$ from eqs. (4.53) and (4.54):

$$R_{30,0} = \frac{R_1 - w_1}{1 - w_1} \tag{4.57}$$

$$R_{0,30} = \frac{R_2 - w_2 R_{a,c}}{1 - w_2}. \tag{4.58}$$

The values of α and $w_\perp$ that were used in eqs. (4.44) and (4.56) to (4.58) to arrive at the presented data are summarized in table 4.2. For Samples 1 and 2, we used the values of α and $w_\perp$ from our simulations. For Sample 3, some adjustment relative to the simulation values was necessary in order to obtain physically plausible results for $R_{a,c}$, $R_{30,0}$, and $R_{0,30}$. We found that the magnitude of R_3 determined using the simulation value α_3^{sim} was larger than expected. Specifically, unless R_3 is of a comparable magnitude to R_2, then the decomposition into components via eqs. (4.56) to (4.58) yields negative values, which is unphysical. A comparable magnitude of R_3 to R_2 can be accomplished by using a value of α_3 of ≈ 4, whereas the simulation value α_3^{sim} is ≈ 2.5. There are a couple potential explanations for this discrepancy. The first is that Sample 3, being cut from a different original sample, has a higher residual scattering rate than Sample 2. In the classical case, $R \propto \sqrt{1/\tau}$, so a factor of $4/2.5 = 1.6$ difference in magnitude corresponds to a factor of $1.6^2 \approx 2.6$ difference in residual scattering rates. This is consistent with the variation in residual resistivity reported by Nandi et al. [44]. The second potential explanation is that we failed to accurately account for geometric effects in our simulations, with α_3^{sim} being smaller than the true value of α_3. This difference in magnitude would result if the power factor α increases more rapidly with decreasing aspect ratio c/a than captured by our simulations. With α_3 set to 4, next we turned to w_3. The simulation value of ≈ 0.45 also lead to negative decomposed values, whereas there is a wide range of w_3 values near ≈ 0.6 for which the decomposed values are positive and only weakly dependent on the specific choice of w_3. As with α, the difference between empirical and simulated results may indicate that simulations are underestimating the magnitude of extrinsic geometric effects

for small aspect ratios. Despite that it was necessary to adjust α_3 and w_3 relative to the simulation values to get physically reasonable results, in both cases there is a range of values which lead to qualitatively similar results.

Sample	α	$w_\perp$
1	2	0.4
2	2	0.4
3	4	0.6

Table 4.2: Data calibration parameters.

The measurements of the three samples, after having applied the power factors from table 4.2, are shown in fig. 4.8d. The fact that the three measurements differ in frequency dependence provides immediate evidence of non-local electrodynamics. In all cases, current flows in the plane perpendicular to the c axis; for local electrodynamics, the triangular in-plane lattice dictates that the conductivity tensor has non in-plane anisotropy and so all three measurements would be identical. Next we will examine the individual surface resistances obtained via the effective surface resistances via eqs. (4.56) to (4.58).

The measured surface resistance for the two in-plane wavevectors is shown in fig. 4.12a. Surprisingly, the two orientations exhibit distinct power-law behaviours. A useful property of the viscosity tensor in a plane with six-fold rotational symmetry provides an elegant avenue for differentiating ballistic and viscous effects: in this setting, as is the case in $PdCoO_2$, the in-plane viscosity tensor is isotropic [23]. This implies the qualitative insight that the anisotropy in the surface resistance at 2 K for the two orientations cannot be due to purely viscous effects.

With this in mind, we turn to the possible ballistic origin of this effect. The standard theory of the anomalous skin effect (i.e., ballistic propagation within the skin layer)—Pippard theory [48]—predicts that any orientation should exhibit $R \sim \omega^{2/3}$, with only the pre-factor being orientation-dependent. Our data is at odds with Pippard theory: while one orientation exhibits behavior close to $\omega^{2/3}$, the other exhibits only a weak deviation from classical behavior. This breakdown of Pippard theory is all the more surprising because—aside from its ubiquity—Pippard theory has previously demonstrated success in describing the behavior of anisotropic FSs. Famously, Pippard performed the first ever experimental determination of a FS by applying his eponymous theory to measurements of the ASE in Cu, revealing deviation from a spherical FS [49]. Nonetheless, Pippard theory treats FS geometry phenomenologically, and was originally justified by agreement with more rigorous treatments based on solving the Boltzmann equation for spherical [51] and spheroidal [57] FSs.

To model our results, we solved the Boltzmann equation using a realistic parameterization of the FS of $PdCoO_2$ based on ARPES and quantum oscillation measurements [28]. As seen, our calculations reproduce the difference in power-law behaviour between the two orientations. An intuitive explanation for the difference in power laws comes from applying Pippard's "ineffectiveness concept" [47, 48] to the FS of $PdCoO_2$: only those electrons that spend an entirety of a MFP within the skin layer are effective at screening electromagnetic fields. As the ratio of MFP to skin depth increases, electrons spend an increasingly small fraction of a MFP within the skin layer, so the surface resistance becomes

increasingly larger than the classical value. Mathematically, this can be described as an effective MFP for each state $\boldsymbol{k}$, which represents that state's contribution to the overall conductivity:

$$\lambda_{\boldsymbol{k}}^{\text{eff}} = \frac{(\hat{\boldsymbol{v}}_{\boldsymbol{k}} \cdot \hat{\boldsymbol{E}})\lambda_0}{1 + i(\hat{\boldsymbol{v}} \cdot \hat{\boldsymbol{q}})q\lambda_0} \tag{4.59}$$

where λ_0 is the bare MFP and $\hat{\boldsymbol{v}}_{\boldsymbol{k}}$ is the unit velocity vector. (Because the present discussion is focused on purely ballistic effects, here we have taken $\lambda_{mr} = \lambda_{mc} = \lambda_0$). In $PdCoO_2$, a third of electrons propagate nearly parallel to the sample's surface, such that $\hat{\boldsymbol{v}} \cdot \hat{\boldsymbol{q}} = 0$. These electrons remain effective at screening regardless of the ratio of MFP to skin depth, largely suppressing the increase in surface resistance. Indeed, there have been several theoretical works predicting extreme FS geometries for which Pippard theory would break down [25, 31, 73]. To our knowledge, the present results represent the first experimental confirmation of these ideas.

We used the Fermi surface parameterization from Hicks et al. [28]:

$$\boldsymbol{k}_F(\phi, \phi_0, k_z) = \rho(\phi - \phi_0, k_z)[\cos\phi\,\hat{\boldsymbol{i}} + \sin\phi\,\hat{\boldsymbol{j}}] + k_z\hat{\boldsymbol{k}} \tag{4.60}$$

where

$$\rho(\phi - \phi_0, k_z) = \sum_{\mu,\nu} k_{\mu\nu}\cos[\mu(\phi - \phi_0)] \begin{cases} \sin[\nu d k_z] & k_{31} \\ \cos[\nu d k_z] & \text{otherwise} \end{cases} \tag{4.61}$$

with $d = c/3$ where $c = 17.743\,\text{Å}$ and with the Fermi surface harmonics listed in table 4.3. The angle ϕ_0 sets the in-plane rotation of the Fermi surface relative to the coordinate system. To take advantage of the simplifications arising from three mirror planes, we set $k_{31} = 0$. We assumed diffuse surface scattering when calculating the surface resistance. We used the reported experimental parameters as given in table 4.4. We took $\gamma_{\boldsymbol{k}x}^{\text{mr}} = \gamma_{\boldsymbol{k}x}^{\text{mr}} = \gamma^{\text{mr}}$ using the value from table 4.4, and took $\gamma_{\boldsymbol{k}}^{\text{mc}} = \gamma^{\text{mc}}$ with γ^{mc} as a free parameter.

μ	ν	$k_{\mu,\nu}$
0	0	0.9538
6	0	0.040
12	0	0.007
0	1	0.0107
0	2	-0.009
3	1	0.0010

Table 4.3: Harmonics for parameterization of Fermi surface of $PdCoO_2$ from Hicks et al. [28].

The measured surface resistance for wavevector along the c axis, shown in fig. 4.13a, exhibits a clear deviation from classical $R \sim \sqrt{\omega}$ behavior. The observation of non-local electrodynamics in this orientation is surprising: as per the ineffectiveness concept, this means that electrons must be able to propagate in and out of the skin layer within a single mean free path. However, the nearly cylindrical geometry of the Fermi surface means that in this orientation, electrons propagate at a shallow angle

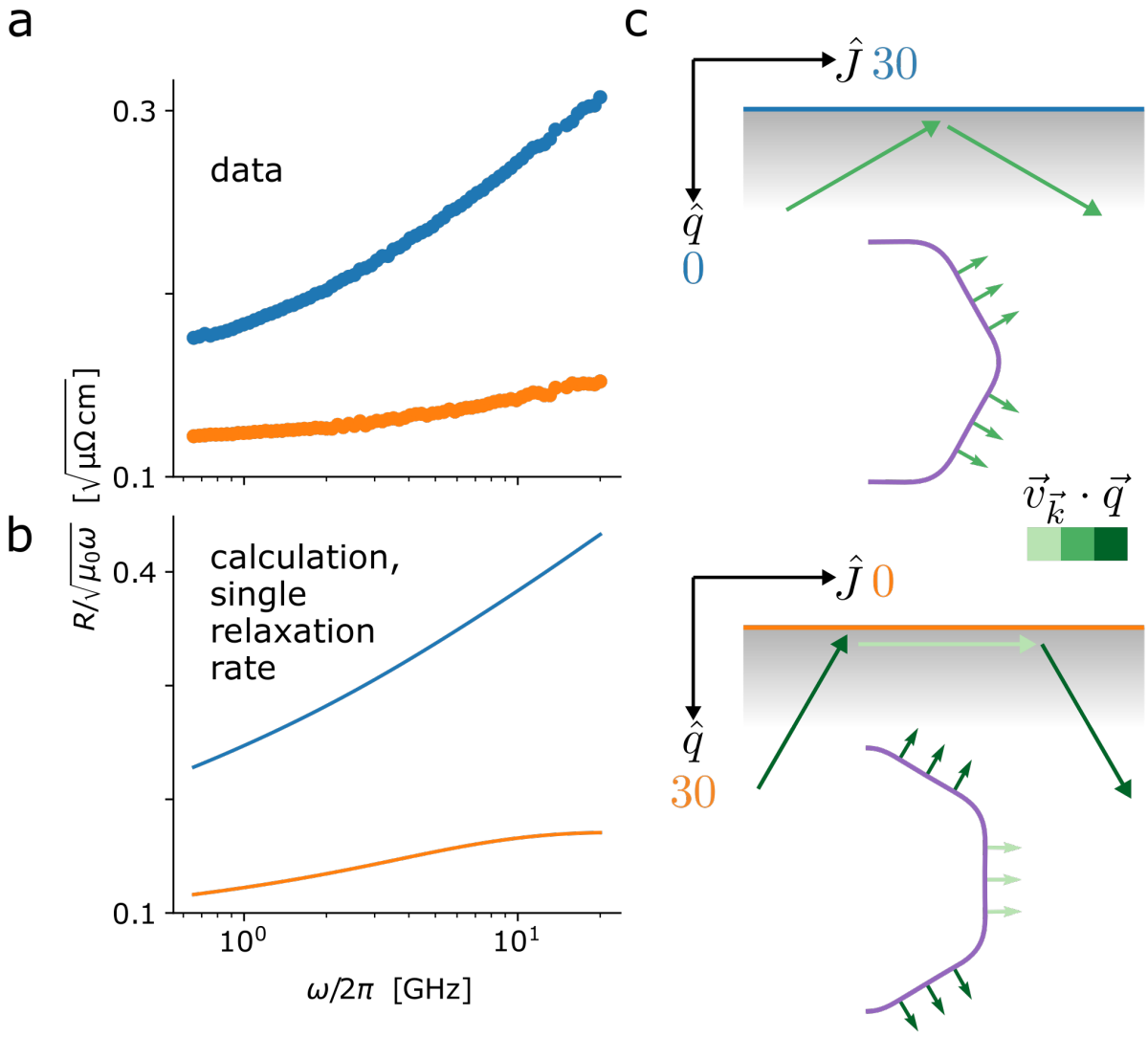

Figure 4.12: Surface resistance measurements for in-plane wavevector. (a) Data obtained by subtracting the $\boldsymbol{q} \parallel c$ component from the raw data. The different power-law behavior originates from predominantly ballistic propagation within the skin layer coupled with a strongly-facetted Fermi surface, as illustrated in (b) and (c). (b) Calculated surface resistance based on the experimentally-determined Fermi surface, capturing the different power-law behavior of the two orientations. The calculation is for a single relaxation rate, i.e. $\gamma_{\mathrm{mc}} = \gamma_{\mathrm{mr}}$, and uses published values with no free parameters. (c) Illustration of ballistic propagation within the skin layer. Top: There are two main directions of electron propagation, both at an angle to the surface. As frequency increases, the skin depth becomes shallower. The electrons spend an increasingly smaller fraction of a mean free path inside the skin layer, leading to an increasing surface resistance—the anomalous skin effect. Bottom: There are three main directions of electron propagation. Electrons propagating parallel to the sample's surface spend the entirety of a mean free path within the skin layer, regardless of how shallow the skin depth becomes. Often, this is a negligible fraction of the Fermi surface; in $PdCoO_2$, approximately a third of the Fermi surface propagates parallel to the sample's surface. The anomalous skin effect is largely suppressed even when the mean free path is much larger than the skin depth. From [6].

Parameter	Value
v_F	7.5×10^5 m/s
$\omega_{p,ab}$	7.2×10^{15} Hz
$\rho_{ab}(T = 2\,\mathrm{K})$	7.5 nΩ cm
$\gamma^{\mathrm{mr}}(T = 2\,\mathrm{K})$	34 GHz

Table 4.4: Parameters for $PdCoO_2$. All parameters are directly from Hicks et al. [28], except for γ^{mr} which was found as $\gamma^{\mathrm{mr}} = \varepsilon_0 \omega_{p,ab}^2 \rho_{ab}$.

relative to the skin layer (fig. 4.13c). $PdCoO_2$ is often described as electronically two-dimensional or quasi-two-dimensional, as supported by its low-temperature resistivity anisotropy of $\rho_c/\rho_a \approx 1000$ [28]. However, in a perfectly two-dimensional material, the ASE would be completely suppressed. Its presence here is a result of the subtle warping of the Fermi surface along k_z, as was resolved by quantum oscillations, and highlights the limitations of a purely two-dimensional description of transport properties in $PdCoO_2$. This observation has implications for DC transport measurements. To date, studies have focused on how resistivity varies when restricting in-plane dimensions; these results imply that size effects will also be present while varying thickness along the c axis. The estimated maximum skin depth over the measured frequency range is on the order of 100 nm. This implies that size effects are likely to be especially important to thin films, which have been the subject of recent growth efforts [13, 27, 59].

Having identified a ballistic origin for the main features of the three measured surface resistances, we now turn to placing a quantitative bound on the rate of MC scattering by comparing to calculations. In fig. 4.14, we show the calculated power-law behaviour of the surface resistance as a function of the relative size of the MC and MR scattering rates γ_{mc}/γ_{mr}. The colour scale displays the evolution of the frequency dependence in this cross-over regime, with the frequency range of our measurement indicated by vertical green lines. Too high a rate of MC scattering ($\gamma_{mc}/\gamma_{mr} > 10$) leads to too little anisotropy between $R_{a,\hat{\boldsymbol{q}}\|0}$ and $R_{a,\hat{\boldsymbol{q}}\|30}$. Below this, the model captures the higher power law seen for $R_{a,\hat{\boldsymbol{q}}\|0}$. However, for $\gamma_{mc}/\gamma_{mr} < 3$, the calculated anisotropy overestimates that seen in the data. We thus indicate lower and upper bounds, corresponding to $3 < \gamma_{mc}/\gamma_{mr} < 10$ for measurements at 2 K. This raises the question of the source of MC scattering at this temperature. Given that $T \ll T_F$, it is expected that direct electron-electron scattering is negligible [18]. Recent theoretical work has explored electron-phonon scattering as a source of MC scattering [29, 36], though we estimate that it is insufficient to give rise to our experimentally-determined value of γ_{mc}. Another recent work has proposed a phonon-mediated electron-electron interaction as a potential source of sufficient MC scattering [71], but such a mechanism in $PdCoO_2$ would be predominantly momentum-relaxing due to electron-electron Umklapp processes. The low temperature of our measurements is suggestive of impurity scattering as the source of the observed γ_{mc} [1, 30]. It was noted by Ref. [18] that the evidence for viscous effects in the width-dependent resistivity measurements from Ref. [43] only sets in at low temperature, further corroborating the impurity scattering scenario. A comparison between the data and calculations for a few selected values of γ^{mc} is shown in fig. 4.15.

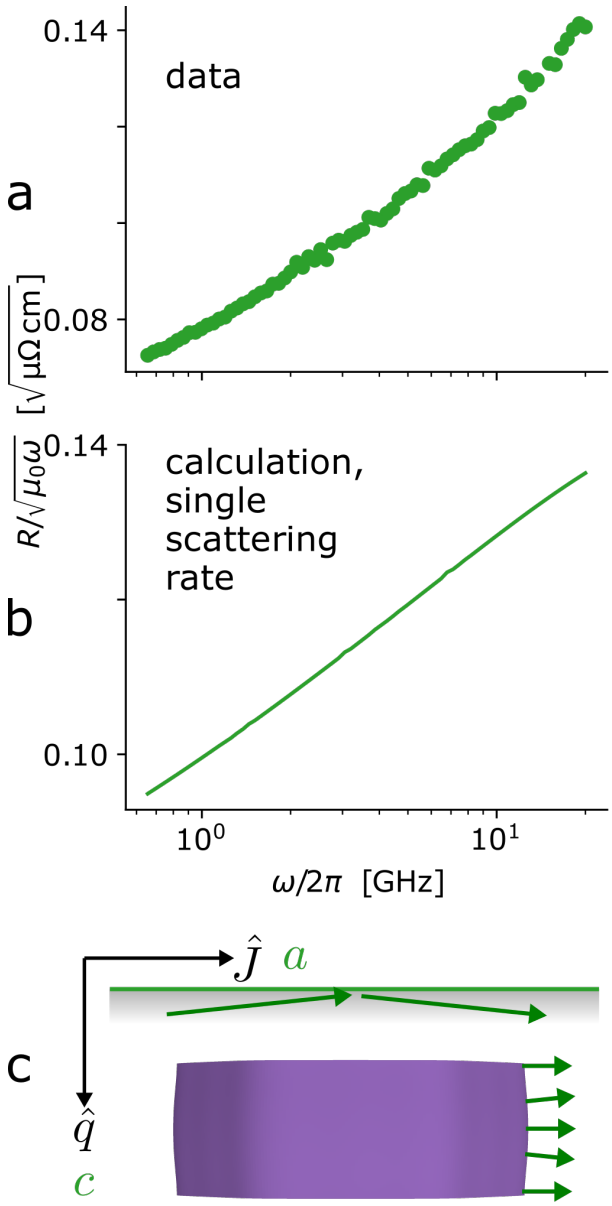

Figure 4.13: Surface resistance measurements for out-of-plane wavevector. (a) Data showing upward deviation from classical $R \sim \sqrt{\omega}$ behavior. Because of the high ratio of mean free path to skin depth reached in the present frequency range, even the small amount of Fermi surface warping along k_z is sufficient to produce non-local effects. (b) Calculated surface resistance based on the experimentally-determined Fermi surface. The calculation is for a single relxation rate, i.e. $\gamma_{\mathrm{mc}} = \gamma_{\mathrm{mr}}$, and uses published values with no free parameters. (c) Illustration of ballistic propagation within the skin layer. From [6].

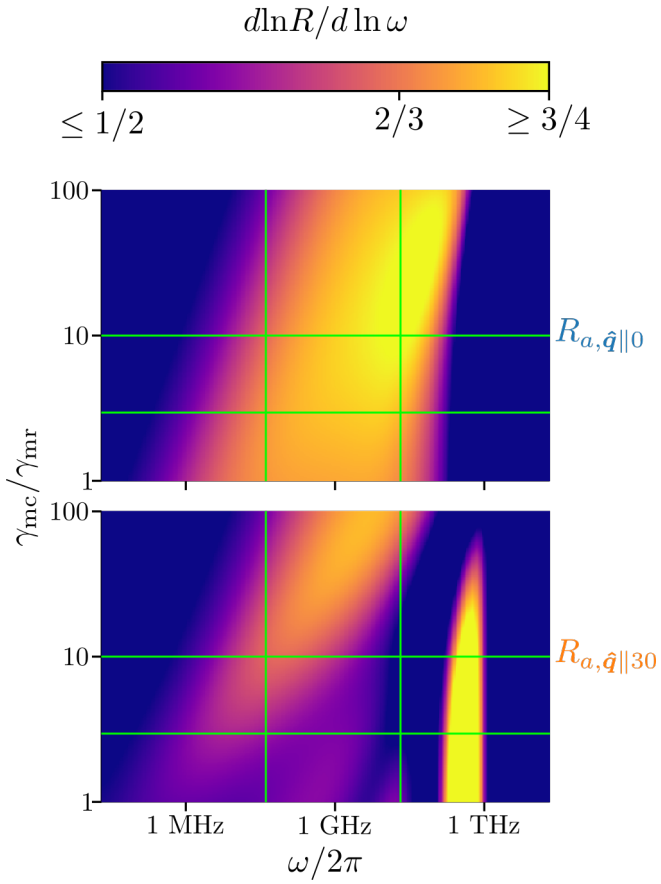

Figure 4.14: Bounds on rate of momentum-conserving scattering. Plots show the dependence of the surface resistance on the rate of momentum-conserving scattering, as calculated using our kinetic theory. Vertical green lines indicate the range of measurement frequency. Horizontal green lines represent bounds on the rate of momentum-conserving scattering deduced for $PdCoO_2$ based on comparison of our theory and experiment. From [6].

4.5 Outlook

Our experiments demonstrate the utility of broadband microwave spectroscopy in the investigation of non-local electrodynamics. While the foundational measurements of the ASE having been performed at fixed frequencies [16, 17, 47, 49], in the present work, continuous-frequency measurements were critical to the interpretation of our results: in particular, in identifying a ballistic- rather than viscous-dominated regime, and in revealing the predicted breakdown of Pippard theory as a result of a strongly-faceted Fermi surface. These effects are also technologically relevant, as future applications of ultra-high-conductivity materials are likely to operate at GHz frequencies. The ASE is known to limit the conductance of interconnects in integrated circuits when operated at these high frequencies [53]. The present results demonstrate that conductance can be improved by aligning interconnects along a direction for which the ASE is suppressed. Finally, to our knowledge, our findings represent the first experimental observation of the ASE outside of elemental metals, suggesting experimental opportunities among new-generation ultra-high-conductivity materials. The interplay of frequency, scattering rates, carrier

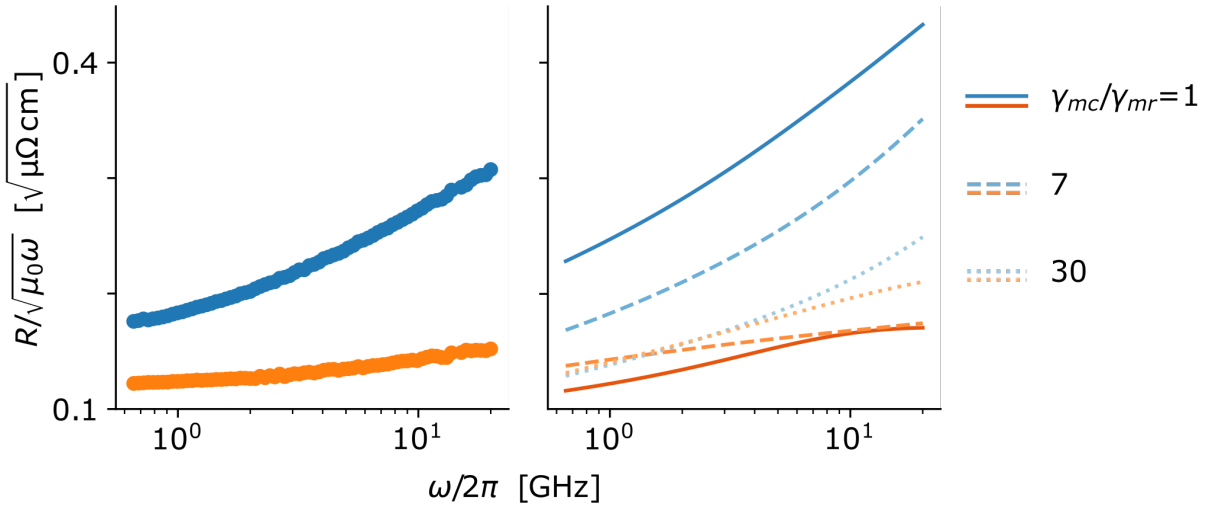

Figure 4.15: Comparison of data with calculations for varying γ^{mc}. From [6].

density, and Fermi surface geometry gives rise to a rich phenomenological landscape for non-local electrodynamics, particularly in the microwave and THz range—which, to date, remains largely unexplored [15, 22, 40, 66–68].

Chapter 5

Conclusion

This thesis has focused on non-local electrical conductivity in $PdCoO_2$, as manifested in measurements of the size effect and the skin effect, and the influence of Fermi surface anisotropy and momentum-conserving scattering.

5.1 Summary

In chapter 1, we introduced the idea of non-local electrical conduction. We reviewed the historical development of its manifestation in the size and skin effects. We also introduced $PdCoO_2$, a material whose long electronic mean free path and simple yet anisotropic Fermi surface presented opportunities to observe novel non-local electrical conduction effects.

We saw in chapter 1 that while theory of the size effect combining both ballistic and viscous effects had been developed, the assumption of an isotropic Fermi surface had always been made. In chapter 2, we addressed this shortcoming, deriving a formula for the size effect within the relaxation time approximation for arbitrary Fermi surface. We applied this result to explain two novel experimental results in the resistivity of narrow channels of $PdCoO_2$ that would be symmetry-forbidden for a local conductivity tensor: in-plane longitudinal resistivity anisotropy, and non-zero transverse resistivity in zero magnetic field.

We saw in chapter 1 that existing theories of the skin effect had captured either ballistic or viscous effects, but not both, and had always assumed an isotropic Fermi surface. In chapter 3, we developed a theory of the electromagnetic response for arbitrary Fermi surface and arbitrary combination of momentum-relaxing and momentum-conserving scattering rates. For a circular Fermi surface geometry, we saw that our theory encompassed previous results based in the two limits of either equal MR and MC scattering rates or of very frequent MC scattering. For polygonal surface geometries, we showed that the qualitative behaviour of the surface impedance differs not just relative to the circular geometry but also based on the relative orientation of the Fermi surface.

In chapter 4, we described our measurements of non-local microwave electrodynamics in $PdCoO_2$. We reviewed the key operating principles of bolometric microwave spectroscopy and discussed its appropriateness to the present goal relative to other experimental techniques. We discussed general fea-

tures of the electrodynamics of finite conductors, revealing the principles that allowed us to connect our power absorption measurements to surface resistances for specific current and wavevector directions. We were able to measure the surface resistance of $PdCoO_2$ for three distinct wavevectors, all for in-plane current. The fact that all three measurements differed implied non-local electrodynamics because they would be symmetry-equivalent within a local picture. The difference in frequency dependence between the two measurements with in-plane wavevectors went beyond Pippard's theory of the anomalous skin effect for anisotropic Fermi surfaces. However, we were able to show that the origin of this difference arises from ballistic propagation in the skin layer; the faceted Fermi surface of $PdCoO_2$ means that for one orientation, a large fraction of electrons are confined to always travel within the skin layer, largely suppressing the anomalous skin effect. We showed that our results were best described by $3 < \gamma_{mc}/\gamma_{mr} < 10$. The measurement for out-of-plane wavevector demonstrated that the finite warping of the Fermi surface along k_z is sufficient to give rise to non-local electrodynamics along this direction as well, showing that a purely two-dimensional description of $PdCoO_2$ is insufficient.

5.2 Future directions

Our view is that this line of research fits in the context of a field for which there are many interesting questions and many opportunities to address these questions. Here we discuss a number of potential future directions related to the present work.

5.2.1 Improved interpretation of electromagnetic measurements

While the power factor approximation developed in section 4.3.3 is well justified in the limit of skin depth much smaller than the sample dimensions, one would ideally like to be able to make a more direct comparison between measurements and calculations. The ultimate capability would be to calculate the power absorption for a given sample geometry and orientation directly from a non-local conductivity tensor $\sigma_{ij}(\boldsymbol{q}, \omega)$. This is in principle possible via the finite element method, though it remains to be seen if it is computationally feasible.

5.2.2 Improved capabilities for electromagnetic measurements

Expanded experimental capabilities for electromagnetic measurements in the microwave and adjacent frequency regimes are likely to be fruitful for investigations of non-local electrodynamics.

One potential direction is to pursue measurements over a broader range of temperature. In many materials, the temperature range most favourable to the observation of the viscous regime is expected to be at a temperature higher than those currently accessible via the bolometric technique. A broader temperature range would enable the possibility of observing a temperature-dependent crossover from local to non-local electrodynamics. The current implementation of the bolometric method is limited to temperatures $<30\,\mathrm{K}$. It may be possible to extend this range to higher temperature by selecting a thermometer whose sensitivity is optimized for a higher temperature range, though thermal noise may place inherent limitations on the upper temperature limit of the technique. Another possibility is to use

microwave cavity perturbation to obtain broad temperature dependence at a fixed frequency.

Another potential direction is to pursue measurements over a broader range of frequency. In many materials, being able to extend measurements to lower frequencies than currently accessible by BMS would aid our chances of being able to observe the viscous regime. On the other hand, the anomalous reflection regime, which may be useful for diagnosing the nature of boundary scattering, is likely to exist at frequencies higher than those currently accessible by BMS. The upper frequency limit can be extended by miniaturizing the transmission line; the lower frequency limit, potentially, by increasing the sensitivity of the bolometric detection. Another avenue would be to apply techniques from the radio-frequency and THz regimes.

Finally, it is desirable to be able to measure the surface reactance in addition to the surface resistance. It is possible to do so in principle via microwave cavity perturbation, though it may be difficult to achieve in practice depending on sample geometry [14].

5.2.3 Improved treatment of anisotropic properties within the RTA

In this thesis, we derived expressions for the size and skin effect for arbitrary Fermi surface geometries and properties. However, we then went on to assume that the scattering time and Fermi velocity magnitude were constant over the Fermi surface, and only analyzed Fermi surface geometries for which a simple, closed-form parameterization was available. It would be desirable to be able to numerically calculate the non-local conductivity using a band structure model as input to determine the Fermi surface geometry and variation of the Fermi velocity magnitude.

5.2.4 Improved treatment of the scattering integral: beyond the viscous versus ballistic dichotomy

The idea of observing hydrodynamic effects in solids has attracted significant recent attention. Contributing to this interest is the universality of a hydrodynamic description of transport processes.

However, the experimental effects being observed in new-generation ultra-high-conductivity materials may be interpreted through a different lens, which was briefly alluded to in chapter 1: these experiments are observing scattering processes that cannot be described with the relaxation time approximation.

The non-equilibrium distribution function can be expanded in terms of the eigenfunctions of the collision operator, each with an associated scattering rate (eigenvalue). For transport processes involving a spatially homogeneous electronic distribution, only a single scattering rate enters the observable properties. For an inhomogeneous electronic distribution, the various eigenfunctions become coupled, and the observable properties depend on the entire spectrum of scattering rates.

Recently, Nazaryan and Levitov [45] showed that the eigenfunctions of the collision operator in an isotropic, two-dimensional metal are the functions $e^{im\phi}$ with m a non-negative integer. They then derived the non-local conductivity for arbitrary eigenvalue scattering rates γ_m in terms of a continued fraction over all γ_m.

Ultimately, it would be desirable to derive the non-local conductivity in terms of the eigenvalues γ_m

of the collision operator for both two- and three-dimensional metals and allowing for arbitrary crystal symmetry

At the same time, it would be desirable to understand what the γ_m spectrum is for different scattering mechanisms (electron-impurity, electron-phonon, electron-electron) in either 2D or 3D and for arbitrary crystal symmetry. To date, we are aware of work deriving the γ_m spectrum for electron-phonon scattering in three-dimensional free-electron metals [36], for electron-electron scattering in two-dimensional metals [35], and for electron-electron scattering in graphene (with a Dirac dispersion) [32]. We note also that the RTA is exact for electron-impurity scattering from point-like impurities.

5.2.5 $PdCoO_2$

For $PdCoO_2$, the source of the MC scattering observed in chapter 4 and by Moll et al. [43] remains an important open question. As mentioned in chapter 4, the temperature at which the MC scattering is observed is strongly suggestive of a basis in electron-impurity scattering. Electron-impurity scattering is not typically associated with MC scattering; as noted in the previous section, for point-like impurities it gives rise to the RTA in which there is no MC scattering in excess of the MR scattering. However, two factors may modify the situation in $PdCoO_2$. With conduction taking place primarily in the Pd planes, defects in the CoO_2 layers will act as out-of-plane scatterers, which are known to enhance forward scattering [19]. Additionally, the γ_m spectrum for electron-impurity scattering may be altered in the presence of Fermi surface anisotropy.

5.2.6 Other materials

Conductors

The number of high-conductivity metals for which effects related to non-local electrical conduction may be observable has grown steadily in recent years. These, and likely other materials yet to be synthesized, will offer the possibility to explore many of the ideas explored in this thesis. Other materials will offer different FS geometries. Just by virtue of having different Fermi velocity and plasma frequency, e.g. in semimetals, different regimes may be accessible even in the same range of measurement frequencies. Finally, it remains to be seen whether a material can be found for which the viscous skin effect is observable.

Superconductors

Closely tied in with the discovery and early development of the anomalous skin effect in metals was the development of non-local electrodynamics (NLE) in superconductors. In chapter 4, studying NLE in metals bore fruit to new discoveries both because of the development of new materials and because of the development of new experimental techniques—namely, bolometric microwave spectroscopy. Since the early work on NLE in superconductors, a plethora of new superconducting materials have been discovered. Therefore, there is good reason to expect the possibility of new discoveries by applying BMS to the study of NLE in superconductors.

Bibliography

[1] P. S. Alekseev. Negative Magnetoresistance in Viscous Flow of Two-Dimensional Electrons. *Physical Review Letters*, 117:166601, 2016. doi:10.1103/PhysRevLett.117.166601. → page 78

[2] E. T. S. Appleyard and A. C. B. Lovell. The Electrical Conductivity of Thin Metallic Films II—Caesium and Potassium on Pyrex Glass Surfaces. *Proceedings of the Royal Society of London. Series A*, 158:718, 1937. doi:10.1098/rspa.1937.0050. → page 5

[3] N. Ashcroft and N. Mermin. *Solid State Physics*. Holt-Saunders, 1976. → page 2

[4] M. D. Bachmann, A. L. Sharpe, A. W. Barnard, C. Putzke, M. König, S. Khim, D. Goldhaber-Gordon, A. P. Mackenzie, and P. J. W. Moll. Super-geometric electron focusing on the hexagonal Fermi surface of $PdCoO_2$. *Nature Communications*, 10:5081, 2019. doi:10.1038/s41467-019-13020-9. → pages 14, 16

[5] M. D. Bachmann, A. L. Sharpe, G. Baker, A. W. Barnard, C. Putzke, T. Scaffidi, N. Nandi, P. H. Mcguinness, E. Zhakina, M. Moravec, S. Khim, M. König, D. Goldhaber-Gordon, A. P. Mackenzie, and P. J. W. Moll. Directional ballistic transport in the two-dimensional metal $PdCoO_2$. *Nature Physics*, 2022. doi:10.1038/s41567-022-01570-7. → pages v, 34, 35, 36, 37, 39

[6] G. Baker, T. W. Branch, J. Day, D. Valentinis, M. Oudah, P. McGuinness, S. Khim, P. Surówka, R. Moessner, J. Schmalian, A. P. Mackenzie, and D. A. Bonn. Non-local microwave electrodynamics in ultra-pure $PdCoO_2$. *arXiv*, 2022. doi:10.48550/arXiv.2204.14239. → pages vi, 71, 72, 73, 77, 79, 80, 81, 93

[7] D. A. Bandurin, I. Torre, R. Krishna Kumar, M. Ben Shalom, A. Tomadin, A. Principi, G. H. Auton, E. Khestanova, K. S. Novoselov, I. V. Grigorieva, L. A. Ponomarenko, A. K. Geim, and M. Polini. Negative local resistance caused by viscous electron backflow in graphene. *Science*, 351(6277):1055–8, 2016. ISSN 1095-9203. doi:10.1126/science.aad0201. URL http://www.ncbi.nlm.nih.gov/pubmed/26912363. → page 8

[8] C. W. Beenakker and H. van Houten. Boundary scattering and weak localization of electrons in a magnetic field. *Physical Review B*, 38:3232, 1988. ISSN 0021-4884. doi:10.15036/arerugi.37.589. → pages 5, 7, 26, 31, 33

[9] C. W. Beenakker and H. van Houten. Quantum Transport in Semiconductor Nanostructures. *Solid State Physics*, 44:1, 1991. ISSN 00811947. doi:10.1016/S0081-1947(08)60091-0. → page 5

[10] C. Bidinosti, E. Chapple, and M. Hayden. The Sphere in a Uniform RF Field—Revisitied. *Concepts in Magnetic Resonance Part B: Magnetic Resonance Engineering*, 31B:191, 2007. ISSN 15525031. doi:10.1002/cmr.b.20090. → page 65

[11] C. P. Bidinosti, W. N. Hardy, D. A. Bonn, and R. Liang. Magnetic field dependence of λ in YBa2Cu3O6.95: Results as a function of temperature and field orientation. *Physical Review Letters*, 83:3277, 1999. ISSN 10797114. doi:10.1103/PhysRevLett.83.3277. → page 68

[12] J. S. Bobowski. *Precision Electrodynamics of Unconventional Superconductors*. PhD thesis, 2010. → pages 56, 57

[13] M. Brahlek, G. Rimal, J. M. Ok, D. Mukherjee, A. R. Mazza, Q. Lu, H. N. Lee, T. Zac Ward, R. R. Unocic, G. Eres, and S. Oh. Growth of metallic delafossite $PdCoO_2$ by molecular beam epitaxy. *Physical Review Materials*, 3:093401, 2019. doi:10.1103/PhysRevMaterials.3.093401. → page 78

[14] T. W. Branch. Microwave Responses of Strongly Demagnetized Metallic Samples. Master's thesis, University of British Columbia, 2021. → pages 72, 84

[15] H. B. G. Casimir and J. Ubbink. The skin effect II. The skin effect at high frequencies. *Philips Technical Review*, 28:300, 1967. ISSN 01490370. URL https://www.pearl-hifi.com/06_Lit_Archive/02_PEARL_Arch/Vol_16/Sec_53/Philips_Tech_Review/PTechReview-28-1967-300.pdf. → pages 21, 22, 23, 49, 52, 81

[16] R. G. Chambers. Anomalous Skin Effect in Metals. *Nature*, 165:289, 1950. doi:https://doi.org/10.1038/165239b0. → page 80

[17] R. G. Chambers. The anomalous skin effect. *Proceedings of the Royal Society A*, 215:481, 1952. doi:https://doi.org/10.1098/rspa.1952.0226. → page 80

[18] C. Q. Cook and A. Lucas. Electron hydrodynamics with a polygonal Fermi surface. *Physical Review B*, 99:235148, 2019. doi:10.1103/PhysRevB.99.235148. → pages 14, 78

[19] S. Das Sarma and F. Stern. Single-particle relaxation time versus scattering time in an impure electron gas. *Physical Review B*, 32:8442(R), 1985. doi:10.1103/PhysRevB.32.8442. → page 85

[20] M. J. M. De Jong and L. W. Molenkamp. Hydrodynamic electron flow in high-mobility wires. *Physical Review B*, 51:13389, 1995. doi:10.1103/PhysRevB.51.13389. → page 8

[21] R. Dingle. The anomalous skin effect and the reflectivity of metals I. *Physica*, 19:311–347, 1953. ISSN 00318914. doi:10.1016/S0031-8914(54)80042-5. → page 42

[22] D. Forcella, J. Zaanen, D. Valentinis, and D. van der Marel. Electromagnetic properties of viscous charged fluids. *Physical Review B*, 90:035143, 2014. ISSN 1550235X. doi:10.1103/PhysRevB.90.035143. URL https://journals.aps.org/prb/pdf/10.1103/PhysRevB.90.035143. → pages 25, 40, 53, 81

[23] U. Frisch, B. Hasslacher, and Y. Pomeau. Lattice-gas Automata for the Navier-Stokes Equation. *Physical Review Letters*, 56:1505, 1986. ISSN 00319007. doi:10.1103/PhysRevLett.56.1505. → pages 53, 75

[24] K. Fuchs. The conductivity of thin metallic films according to the electron theory of metals. *Mathematical Proceedings of the Cambridge Philosophical Society*, 34:100, 1938. doi:10.1017/S0305004100019952. → pages 5, 25, 26, 31, 33

[25] M. L. Glasser. Influence of Band Structure on the Nonlocal Conductivity of Metals and the Anomalous Skin Effect. *Physical Review*, 176:1110, 1968. doi:https://doi.org/10.1103/PhysRev.176.1110. → page 76

[26] R. N. Gurzhi. Hydrodynamic effects in solids at low temperature. *Soviet Physics Uspekhi*, 11(2): 255–270, 1968. ISSN 0038-5670. doi:10.1070/PU1968v011n02ABEH003815. URL http://stacks.iop.org/0038-5670/11/i=2/a=R07?key=crossref.ab092203da31656011fa26b469078a57. → pages 7, 24, 25, 40, 53

[27] T. Harada, K. Fujiwara, and A. Tsukazaki. Highly conductive $PdCoO_2$ ultrathin films for transparent electrodes. *APL Materials*, 6:046107, 2018. doi:10.1063/1.5027579. → page 78

[28] C. W. Hicks, A. S. Gibbs, A. P. Mackenzie, H. Takatsu, Y. Maeno, and E. A. Yelland. Quantum Oscillations and High Carrier Mobility in the Delafossite $PdCoO_2$. *Physical Review Letters*, 109: 116401, 2012. doi:10.1103/PhysRevLett.109.116401. → pages x, 7, 9, 10, 12, 75, 76, 78, 92

[29] X. Huang and A. Lucas. Electron-phonon hydrodynamics. *Physical Review B*, 103:155128, 2021. doi:10.1103/PhysRevB.103.155128. → pages 14, 78

[30] A. Hui, S. Lederer, V. Oganesyan, and E.-A. Kim. Quantum aspects of hydrodynamic transport from weak electron-impurity scattering. *Physical Review B*, 101:121107, 2020. doi:10.1103/PhysRevB.101.121107. → page 78

[31] M. I. Kaganov and P. Contreras. Theory of the anomalous skin effect in metals with complicated Fermi surfaces. *Journal of Experimental and Theoretical Physics*, 79:985, 1994. ISSN 0080-4630. URL http://www.jetp.ac.ru/cgi-bin/e/index/e/79/6/p985?a=list. → page 76

[32] E. I. Kiselev and J. Schmalian. Lévy Flights and Hydrodynamic Superdiffusion on the Dirac Cone of Graphene. *Physical Review Letters*, 123(19):195302, 2019. ISSN 10797114. doi:10.1103/PhysRevLett.123.195302. URL https://doi.org/10.1103/PhysRevLett.123.195302. → page 85

[33] M. J. Ku, T. X. Zhou, Q. Li, Y. J. Shin, J. K. Shi, C. Burch, L. E. Anderson, A. T. Pierce, Y. Xie, A. Hamo, U. Vool, H. Zhang, F. Casola, T. Taniguchi, K. Watanabe, M. M. Fogler, P. Kim, A. Yacoby, and R. L. Walsworth. Imaging viscous flow of the Dirac fluid in graphene. *Nature*, 583(7817):537–541, 2020. ISSN 14764687. doi:10.1038/s41586-020-2507-2. URL http://dx.doi.org/10.1038/s41586-020-2507-2. → page 8

[34] L. D. Landau and E. M. Lifshitz. Chapter VII. In *Electrodynamics of Continuous Media*, chapter VII, pages 199–224. Pergamon, second edition, 1984. doi:10.1016/B978-0-08-030275-1.50013-8. → page 69

[35] P. J. Ledwith, H. Guo, and L. Levitov. The hierarchy of excitation lifetimes in two-dimensional Fermi gases. *Annals of Physics*, 411:167913, 2019. ISSN 1096035X. doi:10.1016/j.aop.2019.167913. URL https://doi.org/10.1016/j.aop.2019.167913. → pages 7, 85

[36] A. Levchenko and J. Schmalian. Transport properties of strongly coupled electron–phonon liquids. *Annals of Physics*, 419:168218, 2020. doi:10.1016/j.aop.2020.168218. → pages 7, 14, 78, 85, 92

[37] A. C. Lovell. The Eectrical Conductivity of Thin Metallic Films I—Rubidium on Pyrex Glass Surfaces. *Proceedings of the Royal Society A*, 157:311, 1936. doi:10.1098/rspa.1936.0197. → page 5

[38] A. Lucas and K. C. Fong. Hydrodynamics of electrons in graphene. *Journal of Physics Condensed Matter*, 30(5), 2018. ISSN 1361648X. doi:10.1088/1361-648X/aaa274. → page 8

[39] A. P. Mackenzie. The properties of ultrapure delafossite metals. *Reports on Progress in Physics*, 80:32501, 2017. doi:10.1088/1361-6633/aa50e5. URL https://iopscience.iop.org/article/10.1088/1361-6633/aa50e5/pdf. → pages 9, 11

[40] P. Matus, R. M. A. Dantas, R. Moessner, and P. Surówka. Skin effect as a probe of transport regimes in Weyl semimetals. *Proceedings of the National Academy of Sciences*, 119: e2200367119, 2022. doi:10.1073/pnas.2200367119. → page 81

[41] P. H. McGuinness, E. Zhakina, M. König, M. D. Bachmann, C. Putzke, P. J. W. Moll, S. Khim, and A. P. Mackenzie. Low-symmetry nonlocal transport in microstructured squares of delafossite metals. *Proceedings of the National Academy of Sciences*, 118:2113185118, 2021. doi:10.1073/PNAS.2113185118. → pages 15, 17

[42] L. W. Molenkamp and M. J. M. de Jong. Electron-electron-scattering-induced size effects in a two-dimensional wire. *Physical Review B*, 49:5038, 1994. doi:10.1103/PhysRevB.49.5038. → pages 8, 13, 25

[43] P. J. W. Moll, P. Kushwaha, N. Nandi, B. Schmidt, and A. P. Mackenzie. Evidence for hydrodynamic electron flow in $PdCoO_2$. *Science*, 351(6277):1061–4, 2016. ISSN 1095-9203. doi:10.1126/science.aac8385. URL http://www.ncbi.nlm.nih.gov/pubmed/26912359. → pages 13, 14, 15, 78, 85

[44] N. Nandi, T. Scaffidi, P. Kushwaha, S. Khim, M. E. Barber, V. Sunko, F. Mazzola, P. D. C. King, H. Rosner, P. J. W. Moll, M. König, J. E. Moore, S. Hartnoll, and A. P. Mackenzie. Unconventional magneto-transport in ultrapure $PdCoO_2$ and $PtCoO_2$. *npj Quantum Materials*, 3: 66, 2018. doi:10.1038/s41535-018-0138-8. URL https://doi.org/10.1038/s41535-018-0138-8. → pages 33, 34, 74, 92

[45] K. G. Nazaryan and L. Levitov. Robustness of vorticity in electron fluids. (1):1–11, 2021. URL http://arxiv.org/abs/2111.09878. → pages 8, 84

[46] H.-J. Noh, J. Jeong, J. Jeong, E.-J. Cho, S. B. Kim, K. Kim, B. I. Min, and H.-D. Kim. Anisotropic Electric Conductivity of Delafossite PdCoO2 Studied by Angle-Resolved Photoemission Spectroscopy. *Physical Review Letters*, 102:256404, 2009. doi:10.1103/PhysRevLett.102.256404. → page 9

[47] A. Pippard. The surface impedance of superconductors and normal metals at high frequencies II. The anomalous skin effect in normal metals. *Proceedings of the Royal Society A*, 191:385–399, 1947. doi:10.1098/rspa.1947.0122. → pages 18, 20, 25, 75, 80

[48] A. Pippard. The anomalous skin effect in anisotropic metals. *Proceedings of the Royal Society A*, 224:273–282, 1954. URL https://doi.org/10.1098/rspa.1954.0157. → pages 22, 40, 75

[49] A. Pippard. An Experimental Determination of the Fermi Surface in Copper. *Philosophical Transactions of the Royal Society A*, 250:325, 1957. doi:10.1098/rsta.1957.0023. → pages 22, 23, 24, 75, 80

[50] R. Prozorov and V. G. Kogan. Effective Demagnetizing Factors of Diamagnetic Samples of Various Shapes. *Physical Review Applied*, 10:14030, 2018. doi:10.1103/PhysRevApplied.10.014030. → pages 66, 68

[51] G. E. H. Reuter and E. H. Sondheimer. The theory of the anomalous skin effect in metals. *Proceedings of the Royal Society A*, 195:336–364, 1948. doi:10.1098/rspa.1948.0123. → pages 19, 22, 25, 40, 42, 51, 53, 75

[52] P. L. Richards. Bolometers for infrared and millimeter waves. *Journal of Applied Physics*, 76:1, 1994. doi:10.1063/1.357128. → page 56

[53] R. Sarvari. *Impact of Size Effects and Anomalous Skin Effect on Metallic Wires as GSI Interconnects*. PhD thesis, Georgia Institute of Technology, 2008. → page 80

[54] G. S. Smith. On the skin effect approximation. *American Journal of Physics*, 58:996, 1990. doi:10.1119/1.16266. → page 68

[55] H. Smith and H. H. Jensen. *Transport phenomena*. Oxford University Press, 1989. → page 41

[56] E. Sondheimer. The mean free path of electrons in metals. *Advances in Physics*, 1:1–42, 1952. doi:10.1080/00018735200101151. → page 5

[57] E. H. Sondheimer. The Theory of the Anomalous Skin Effect in Anisotropic Metals. *Proceedings of the Royal Society A*, 224:260, 1954. doi:https://doi.org/10.1098/rspa.1954.0156. → pages 22, 25, 40, 53, 75

[58] J. A. Sulpizio, L. Ella, A. Rozen, J. Birkbeck, D. J. Perello, D. Dutta, M. Ben-Shalom, T. Taniguchi, K. Watanabe, T. Holder, R. Queiroz, A. Principi, A. Stern, T. Scaffidi, A. K. Geim, and S. Ilani. Visualizing Poiseuille flow of hydrodynamic electrons. *Nature*, 576(7785):75–79, 2019. ISSN 14764687. doi:10.1038/s41586-019-1788-9. → page 8

[59] J. Sun, M. R. Barone, C. S. Chang, M. E. Holtz, H. Paik, J. Schubert, D. A. Muller, and D. G. Schlom. Growth of PdCoO2 by ozone-assisted molecular-beam epitaxy. *APL Materials*, 7: 121112, 2019. doi:10.1063/1.5130627. → page 78

[60] V. Sunko. *Bulk States in $PtCoO_2$ and $PdCoO_2$*. PhD thesis, 2019. → pages x, 9, 10, 33

[61] V. Sunko, P. H. Mcguinness, C. S. Chang, E. Zhakina, S. Khim, C. E. Dreyer, M. Konczykowski, H. Borrmann, P. J. W. Moll, M. König, D. A. Muller, and A. P. Mackenzie. Controlled Introduction of Defects to Delafossite Metals by Electron Irradiation. *Physical Review X*, 10: 021018, 2020. doi:10.1103/PhysRevX.10.021018. → pages 11, 12, 14

[62] H. Takatsu, S. Yonezawa, S. Mouri, S. Nakatsuji, K. Tanaka, and Y. Maeno. Roles of high-frequency optical phonons in the physical properties of the conductive delafossite $PdCoO_2$. *Journal of the Physical Society of Japan*, 76:104701, 2007. ISSN 00319015. doi:10.1143/JPSJ.76.104701. → page 92

[63] P. J. Turner. *Broadband Microwave Spectroscopy of $YBa_2Cu_3O_{6+y}$*. PhD thesis, 2004. → page 56

[64] P. J. Turner, D. M. Broun, S. Kamal, M. E. Hayden, J. S. Bobowski, R. Harris, D. C. Morgan, J. S. Preston, D. A. Bonn, and W. N. Hardy. Bolometric technique for high-resolution broadband microwave spectroscopy of ultra-low-loss samples. *Review of Scientific Instruments*, 75(1): 124–135, 2004. doi:10.1063/1.1633001. → pages 56, 58, 61

[65] H. Usui, M. Ochi, S. Kitamura, T. Oka, D. Ogura, H. Rosner, M. W. Haverkort, V. Sunko, P. D. King, A. P. Mackenzie, and K. Kuroki. Hidden kagome-lattice picture and origin of high conductivity in delafossite $PtCoO_2$. *Physical Review Materials*, 3(4):1–8, 2019. ISSN 24759953. doi:10.1103/PhysRevMaterials.3.045002. → pages 11, 13

[66] D. Valentinis. Optical signatures of shear collective modes in strongly interacting Fermi liquids. *Physical Review Research*, 3:023076, 2021. doi:10.1103/PhysRevResearch.3.023076. → pages 25, 81

[67] D. Valentinis, J. Zaanen, and D. Van Der Marel. Propagation of shear stress in strongly interacting metallic Fermi liquids enhances transmission of terahertz radiation. *Scientific Reports*, 11:7105, 2021. doi:10.1038/s41598-021-86356-2. → page 25

[68] D. Valentinis, G. Baker, D. A. Bonn, and J. Schmalian. Kinetic theory of the non-local electrodynamic response in anisotropic metals: skin effect in 2D systems. 2022. URL http://arxiv.org/abs/2204.13344. → page 81

[69] D. Valentinis, G. Baker, D. A. Bonn, and J. Schmalian. Kinetic theory of the non-nocal electrodynamic response in anisotropic metals: skin effect in 2D systems. *arXiv*, 2022. doi:10.48550/ARXIV.2204.13344. → pages v, 52, 54, 55

[70] U. Vool, A. Hamo, G. Varnavides, Y. Wang, T. X. Zhou, N. Kumar, Y. Dovzhenko, Z. Qiu, C. A. Garcia, A. T. Pierce, J. Gooth, P. Anikeeva, C. Felser, P. Narang, and A. Yacoby. Imaging phonon-mediated hydrodynamic flow in WTe2. *Nature Physics*, 17(11):1216–1220, 2021. ISSN 17452481. doi:10.1038/s41567-021-01341-w. → page 8

[71] Y. Wang, G. Varnavides, P. Anikeeva, J. Gooth, C. Felser, and P. Narang. Generalized Design Principles for Hydrodynamic Electron Transport in Anisotropic Metals. 2021. URL http://arxiv.org/abs/2109.00550. → page 78

[72] A. Zangwill. *Modern Electrodynamics*. Cambridge University Press, Cambridge, 2012. doi:10.1017/CBO9781139034777. → page 63

[73] N. A. Zimbovskaya. Local features of the Fermi surface curvature and the anomalous skin effect in metals. *Journal of Physics: Condensed Matter*, 18:8149, 2006. doi:10.1088/0953-8984/18/35/003. → page 76

Appendix A

Estimate of momentum-conserving electron-phonon scattering in $PdCoO_2$

Here we estimate the rate of momentum-conserving electron-phonon scattering in $PdCoO_2$. First, we obtained an experimental MR scattering rate as $\gamma_1^{\text{exp}} = \rho_{xx}/\varepsilon_0\omega_{p,xx}^2$ using ρ_{xx} for a 155 µm channel from Nandi et al. [44] and using $\omega_{p,xx}$ = 7.2×10^{15} Hz from Hicks et al. [28]. Next, we performed fits to γ_1^{exp}. The results are shown in fig. A.1 and the fit parameters given in table A.1. To find the MR electron-impurity scattering rate γ_1^{imp}, we fit γ_1^{exp} to a constant over the range $2\,\text{K} < T < 10\,\text{K}$. Next we considered electron-phonon scattering. It has previously been noted that at high temperature $\gamma_1^{\text{exp}} \propto T^{\alpha}$ with $\alpha > 1$, in contrast with expectation that $\alpha = 1$ within the Bloch-Grüneisen treatment of electron-acoustic phonon scattering. This discrepancy has been attributed to electron-optical phonon scattering [28, 62]. Therefore, we fit $\gamma_1^{\text{exp}} - \gamma_1^{\text{imp}}$ to a sum of Einstein and Debye contributions using

$$\hbar\gamma_1^{\text{Ein}} = \frac{\pi}{2}\lambda_E k_B T_E \frac{T_E/T}{\sinh^2(T_E/2T)} \tag{A.1}$$

and

$$\hbar\gamma_l^{\text{Deb}} = 4\pi\lambda_D k_B T \left(\frac{T}{T_D}\right)^2 \int_0^{T_D/T} dx \frac{x^3}{\cosh(x)-1}\left[1 - P_l\left(1 - (T/T_D)^2 x^2\right)\right] \tag{A.2}$$

with $l = 1$ (cf. eq. A.45 from Levchenko and Schmalian [36]). The fit returned Debye and Einstein temperatures T_D and T_E and transport electron-phonon couplings λ_D and λ_E. Following Hicks et al. [28], the fit was performed over the range $60\,\text{K} < T < 300\,\text{K}$. Having determined T_D and λ_D, we then used eq. (A.2) to determine γ_l^{Debye} for all l, as shown in fig. A.2. We see that at 2 K, all γ_l for electron-Debye phonon scattering are less than the experimentally determined MR scattering rate. Therefore, electron-phonon scattering is unlikely to be responsible for the MC scattering inferred from our measurements.

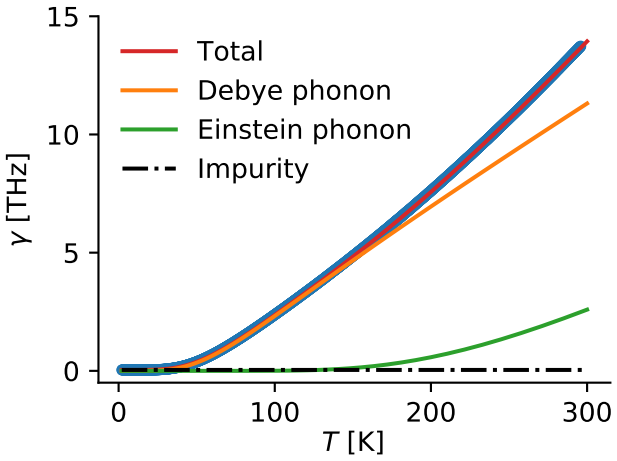

Figure A.1: Momentum-relaxing temperature-dependent scattering rates determined by fitting to bulk resistivity measurements. From [6].

γ_1^{imp}	39 GHz
λ_D	0.049
T_D	331 K
λ_E	0.030
T_E	1120 K

Table A.1: Fit parameters.

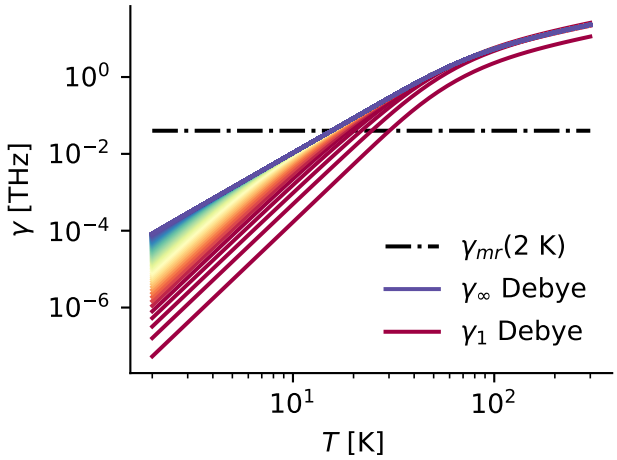

Figure A.2: Spectrum of scattering rates for electron-Debye phonon scattering compared with 2 K momentum-relaxing scattering rate. From [6].